STATE OF CALIFORNIA • DEPARTMENT OF TRANSPORTATION

TECHNICAL REPORT DOCUMENTATION PAGE

TR0003 (REV 10/98)

ADA Notice

For individuals with sensory disabilities, this document is available in alternate formats. For information call (916) 654-6410 or TDD (916) 654-3880 or write Records and Forms Management, 1120 N Street, MS-89, Sacramento, CA 95814.

1. REPORT NUMBER	2. GOVERNMENT ASSOCIATION NUMBER	3. RECIPIENT'S CATALOG NUMBER
RTA-65A0102		

4. TITLE AND SUBTITLE

MOBILE PLATFORM FOR OVERHEAD DETECTORS OF ROAD VEHICLES

5. REPORT DATE

June 2002

6. PERFORMING ORGANIZATION CODE

7. AUTHOR

Fidelis O. Eke

8. PERFORMING ORGANIZATION REPORT NO.

9. PERFORMING ORGANIZATION NAME AND ADDRESS

DEPARTMENT OF MECHANICAL AND AERONAUTICAL ENGINEERING
UNIVERSITY OF CALIFORNIA
ONE SHIELDS AVENUE
DAVIS, CA 95616

10. WORK UNIT NUMBER

11. CONTRACT OR GRANT NUMBER

65A0102

12. SPONSORING AGENCY AND ADDRESS

California Department of Transportation
Sacramento, CA 95819

13. TYPE OF REPORT AND PERIOD COVERED

Final March 2001 - March 2002

14. SPONSORING AGENCY CODE

15. SUPPLEMENTARY NOTES

16. ABSTRACT

The California Department of Transportation (CALTRANS) has a need to monitor traffic flow over freeways. Currently, this is done mainly through the use of “loop detectors.” These are measuring devices that are buried under the road pavement, and that can indicate whether or not a vehicle is present, and give qualitative speed relationships. Because this class of detectors are known to have low reliability, CALTRANS is working on developing a new family of sophisticated electronic sensing devices for the purpose of monitoring certain characteristics of road vehicles as they move along the highway. The devices currently under development are to be located overhead individual highway traffic lanes, from where they can have a clear “view” of ground vehicles. In order to deploy these devices, there is a need to develop the capability to safely and efficiently mount them above highway traffic lanes, using existing overhead bridges and sign structures as support structures.

In fulfillment of a CALTRANS contract for the development of a viable mounting system for these new electronic measuring instruments, this report presents a complete engineering study of a mobile support platform that will use existing walkway structure as support. The study discusses such issues as mobility, effects of wind loading from moving vehicles, vibration isolation, safety, reliability, and resistance to environmental and other hazards. The report includes information on the complete design, construction, and testing of a prototype of the platform system.

17. KEY WORDS	18. DISTRIBUTION STATEMENT	
Caltrans, Safety, Platform, Electronic, Overhead, Mobile, Detector		
19. SECURITY CLASSIFICATION *(of this report)*	**20. NUMBER OF PAGES**	**21. COST OF REPORT CHARGED**
unclassified	119	

MOBILE PLATFORM FOR OVERHEAD DETECTORS OF ROAD VEHICLES

FINAL TECHNICAL REPORT

Submitted to

CALIFORNIA DEPARTMENT OF TRANSPORTATION (CALTRANS)

In fulfillment of

RESEARCH TECHNICAL AGREEMENT NO. 65A0102

by

DEPARTMENT OF MECHANICAL AND AERONAUTICAL ENGINEERING
UNIVERSITY OF CALIFORNIA
ONE SHIELDS AVENUE
DAVIS, CA 95616

Principal Investigator: **Fidelis O. Eke**
Co-Investigator: **Harry H. Cheng**
Research Assistant: **Jacob Duane**

Period: **March 23, 2001 to March 23, 2002**

MOBILE PLATFORM FOR OVERHEAD DETECTORS OF ROAD VEHICLES

ABSTRACT

The California Department of Transportation (CALTRANS) has a need to monitor traffic flow over freeways. Currently, this is done mainly through the use of "loop detectors." These are measuring devices that are buried under the road pavement, and that can indicate whether or not a vehicle is present, and give qualitative speed relationships. Because this class of detectors are known to have low reliability, CALTRANS is working on developing a new family of sophisticated electronic sensing devices for the purpose of monitoring certain characteristics of road vehicles as they move along the highway. The devices currently under development are to be located overhead individual highway traffic lanes, from where they can have a clear "view" of ground vehicles. In order to deploy these devices, there is a need to develop the capability to safely and efficiently mount them above highway traffic lanes, using existing overhead bridges and sign structures as support structures.

In fulfillment of a CALTRANS contract for the development of a viable mounting system for these new electronic measuring instruments, this report presents a complete engineering study of a mobile support platform that will use existing walkway structure as support. The study discusses such issues as mobility, effects of wind loading from moving vehicles, vibration isolation, safety, reliability, and resistance to environmental and other hazards. The report includes information on the complete design, construction, and testing of a prototype of the platform system.

ACKNOWLEDGMENT

The material presented in this report is based on the research effort of several individuals. By far the greatest contributor to this work is Mr. Jacob Duane, whose M.S. thesis work was based on this topic and was completely supported by the contract. We also wish to acknowledge the assistance of post doctoral researcher Zhaoqing Wang, post-graduate researcher Qingcang Yu, and undergraduate students Chanh Truong, Chris Schleich, and Johann Tiamzon. Each of these individuals made important contributions to the final outcome of this research project.

We take this opportunity to express our immense gratitude to Mr. Joe Palen, Senior Research Engineer with ATMIS Development at CALTRANS, who served as Contract Manager for this project. His frequent advice and suggestions, based on experience and deep engineering insight were invaluable throughout the duration of the project.

Finally, we are most grateful to CALTRANS for its generous support of our research efforts through this technical research agreement No. 65A0102.

Fidelis O. Eke and Harry H. Chang
June 2002

TABLE OF CONTENTS

CHAPTER 1

INTRODUCTION

1.1 Background

The California Department of Transportation (Caltrans) has always been interested in monitoring traffic flow on roadways as part of its effort to improve the efficiency of road transportation systems in California. Currently, Caltrans has the ability to monitor traffic flow by means of "loop detectors." These detectors are in-pavement devices that can indicate whether or not a vehicle is present. They are also capable of yielding qualitative speed relationships (fast, medium, or slow). It is now a well-known fact that these loop detectors have significant maintenance, accuracy and reliability problems. For example, Caltrans' District 4 (San Francisco Bay Area) has over four hundred freeway loop surveillance stations. A recent study conducted over a two-year period showed that only between twenty and forty of the more than four hundred installed loop detectors produced data that were good enough to be of much use most of the time.

Travel time is one of the most important measures of effectiveness and efficiency of a transportation system. Travel time is simply the time taken by a vehicle to travel between two points. To determine this, one monitors a vehicle as it passes two locations separated by a known distance. This requires the capability to identify a vehicle as it passes a point *A* and then to re-identify the same vehicle as it passes another point *B*. Loop detectors cannot do this. In fact, Caltrans Operations currently has no system anywhere in the state capable of continuously measuring and reporting travel time.

Even more useful than knowing the current travel time is having an accurate prediction of what the travel time will be when a traveler actually gets to a highway segment. This

requires a “look-ahead” predictive model and a study of how the origin/destination (O/D) patterns of road vehicles intersect to produce congestion. Real data on O/D patterns are necessary to validate any theoretical traffic models that may be developed. In fact, the main reason traffic models currently have very limited use in real world settings is the difficulty in validating these models, due to the unavailability of valid O/D data. Such data cannot be collected via loop detectors. Here again, Caltrans currently has no means of collecting significant samples of O/D data needed for valid congestion predictions.

For many years now, Caltrans has encouraged and sponsored efforts to develop alternatives to the in-pavement loop detectors. A major objective is to find a means of detection that can be deployed out-of-pavement and that has at least some of the capabilities above. An out-of-pavement device will be more accessible, and therefore easier, safer, and cheaper to install and maintain. Many out-of-pavement detectors are based on video image processing systems (VIPS) where a video camera image is read and interpreted by a computer. Another, and more promising example of the new generation of detectors is a laser based overhead detector such as the one recently developed at UC Davis and jointly patented by Caltrans and UC Davis.

Naturally, a device such as this still needs to be placed somewhere in the vicinity of a given highway in order to effectively monitor vehicle activity on the highway. The design of the family of detection devices currently under development assumes that these devices will be located over individual highway traffic lanes. This mounting position allows the detectors to have an unobstructed view of the vehicles. Possible support structures for these devices include existing overhead bridges and sign structures.

1.2 Problem Statement

Field testing and further refinement of both the laser detector system and the VIPS have been impeded by the lack of an effective and efficient overhead mounting mechanism. Figure 1 below shows a mount arrangement used for one of the tests conducted on the

laser detector. The detection system was basically custom mounted on a bridge railing for each test. This is time consuming, inefficient, and is not theft or vandal resistant; it is thus unsuitable for long-term use.

Figure.0.1.1 Custom Mount for Laser Detector

With the desire to exploit the advanced monitoring capabilities of the new family of out-of-pavement detectors, comes the need for mounting them properly, safely, and effectively over the roadway. Because it may become necessary to use different devices at the same location (above the freeway) at different periods of time, there is also a need for the capability to mount, dismount, and replace the monitoring devices without disrupting traffic. The current plan is to develop a generic support platform for holding and positioning these sensing devices, possibly with an adapter for each type of device. One such platform will carry a single electronic sensing device, and several such

sensor/platform systems can be placed on an existing standard overhead truss to individually monitor multiple lanes of traffic.

The purpose of this work is to carry out a comprehensive engineering study of such a support platform that will carry the detection and monitoring devices that are under development or currently available. The study will culminate in the actual design, construction, and testing of a prototype of the system.

1.3 Requirements

The support system described above is to be placed above individual freeway lanes and will hold sensitive instruments over live traffic. It is expected, therefore, that the platform will meet a number of requirements, primarily in the following areas:

- ease of mounting/dismounting
- safety and structural integrity
- reliability and resistance to environmental and other hazards

Mounting

It is expected that different monitoring devices will be needed at any given location to perform various tasks at different times of the year. Hence, there will be need to replace the particular device on a platform from time to time. It would be preferable if such replacement/installation of devices could be done without shutting down traffic lanes, and in fact, without interfering in any way with the flow of traffic. Because of this, the platform and its monitoring device should be relatively inconspicuous so as not to distract the driving public. It is clearly undesirable to have a human worker climb over the highway to install or remove a detector on one or more of the platforms every time that such a change is warranted. This is not only hazardous to both the worker and the traveling public; it is also a source of interference to normal traffic flow. One way to resolve the device-replacement problem is to make the platform mobile relative to the truss structure on which it rests. This way, when there is a need to replace the device on

a given platform, that platform can be moved to one end of the overhead truss, from where it can be accessed, without traffic disruption, by a human worker for the purposes of mounting or dismounting the measuring device. The design of the platform should give it the mobility needed to allow for the location of the sensing device anywhere on the truss span.

Safety

Safety is of the utmost importance for any system that needs to be placed above the roadway. In addition to avoiding hazards when mounting and dismounting the platform, the system must be properly secured to its supporting truss once above traffic so that the device or platform parts will not fall onto the traffic below. The system must also be easily and smoothly integrated with the existing sign truss systems. Any needed modification to the truss system should be minimal, and have no appreciable negative impact on the truss' structural integrity. Trucks and other large vehicles moving at highway speeds below can impose significant wind loads on the platform and mounted device. The platform system and the manner in which the system is secured to the supporting truss structure must therefore be such as to withstand these potentially large forces from frequent wind gusts. The platform must be able to isolate the monitoring device from excessive vibration to ensure accurate data collection and retrieval.

Reliability

The device and mounting platform could remain in place over traffic for years, and thus be subject to such environmental conditions as rain, sunshine, dust, etc. Therefore, the platform support system should be designed to withstand or be protected from environmental hazards. In addition, the platform needs to be constructed with reliable components that will remain operational after long periods of immobility. In the event that the platform becomes stuck in place over traffic, the design should provide for an easy way to return mobility to the platform.

Other Requirements

The system's design and configuration should be such as to maximize its vandal resistance – making it difficult to be moved/removed by anyone but Caltrans personnel. The system will need power for operation. Thus, power should be supplied to the platform in some manner that allows the operation of the platform as well as the mounted device. It should be possible to mount multiple platforms on a given truss, all using the same power source. Finally, the system should be as simple as possible, and capable of being fabricated using low maintenance, low cost, and low complexity mechanical components.

CHAPTER 2

DESIGN ISSUES

In this chapter, a number of issues that are essential to the basic design of the support platform under study are discussed. The purpose is to explain the motivation behind certain initial choices that were made for the system's overall configuration, and set the stage for the next chapter where the system's basic design is discussed.

2.1 Platform Mobility

As mentioned earlier, there is great merit in making the platform movable relative to the support truss. The main benefit is that this reduces, and can even eliminate the need for a human worker to be suspended over traffic each time that the platform and mounted device need to be repositioned over the freeway; or when it is necessary to replace or change the device, or to retrieve the system for routine maintenance. Mobility raises other issues, however. One important issue to be resolved in the early phase of the platform design is the choice of the "best" method for platform mobility. Clearly, the platform must be equipped with rollers or wheels to permit motion. Platform mobility can be accomplished manually, through mechanical means such as cables, pulleys, and gears. It is also possible to motorize the platform, and even to control its motion through the use of automatic control circuitry.

Some type of restraint mechanism for the platform will also be needed. Restraining the platform can be accomplished by purely mechanical means, or as part of the platform's electromechanical motion control system. An appropriate restraint system for the

platform will prevent gross vertical and horizontal motion due to disturbances such as wind gusts generated by passing vehicles and the environment.

The strategy for placing or mounting the platform on the supporting truss or for dismounting it when necessary can have a great deal of influence on the platform's overall design. In order to avoid the need for a human worker to climb onto the truss to install or remove a monitoring device, the mobile platform can be moved to one end of the truss, where it can then be accessed safely and with minimal traffic disruption. Once the platform is at the end of the truss, there are at least two options for retrieval or placement of the platform and device. One direct way of doing this is to have a worker get up to the platform by means of a bucket truck specially equipped for that purpose, or through the use of a ladder that is permanently fixed to the structure. Another option is to configure the system in such a way that the platform with mounted device can be raised and lowered between the truss and the ground level from one end of the truss. This option would include a winch or similar system for raising and lowering the platform, and a method of connecting and disconnecting the platform from the winch.

The first option above has the advantage of simplicity. The main drawback comes from the fact that, in general, personnel that operate the platform and its monitoring device would normally come from a different department or office than the personnel that manage the bucket truck needed to access the platform. Hence, when a change is to be made to the device on the platform, delays can occur from the need to coordinate and schedule the necessary activities with personnel from more than one department. It would be most desirable to design the platform system in such a way that it becomes possible for the operators of the monitoring device to access the entire system without the need for a bucket truck or similar equipment. It would be most advantageous if this can be done without a prohibitive rise in system complexity and cost, and without compromising system safety and reliability. The need to make the system resistant to tampering by vandals will also play a role in the overall system design.

2.2 Power Considerations

Unless a manual approach to moving and restraining the platform system is adopted, and the electronic instrument is battery operated, the system will need power to operate. At least one electric motor will be necessary for driving the trolley; and linear actuators or similar devices will be needed for holding the trolley in place. These components and any control circuitry that may be utilized, as well as the electronic device supported by the trolley, will all need electric power. The issue of supplying power to the trolley system while above traffic thus becomes important. One idea is to hardwire power to the trolley using small gauge wiring. This immediately leads to myriads of problems that must be addressed: the wires would need to be held above traffic somehow; cables would need to be dragged by the trolley, possibly creating a torque and large resistance forces on the trolley; it would be difficult to mount multiple trolleys on a single truss, and it would be equally difficult to remove them. All of these make the use of wiring to supply power directly to the trolley problematic. A proposed solution is presented in chapter 3.

2.3 Vibration Suppression

Any detection device mounted on one of the platforms will inevitably be subject to vibrations. Part of the vibratory motion will come from ground motion transmitted to the system via the flexible truss to which the platform is mounted. Another important source of vibration excitation to the trolley system is the frequent wind loading from passing vehicles. Various methods of vibration suppression have been documented in the literature. There are two main techniques: active and passive. As the name indicates, active techniques usually involve the use of active open-loop or feedback control loops, and may thus require actuators and sensors. Passive methods, on the other hand, generally exploit the inherent dynamics of the system and use some type of oscillator to damp out vibration. Both techniques have been used extensively in industry, especially in the aerospace industry where it is often necessary to control the vibratory motion of spacecraft that carry flexible appendages [see for example Banerjee (1993), Singhose, et al. (1997), Singer, et al. (1990). Naturally, passive methods are preferred whenever they

can be used effectively to control vibration, since they are generally less complex and less expensive than their active counterpart. The passive approach was chosen for this project, and details of the vibration suppression scheme are given in chapter 5.

CHAPTER 3

BASIC DESIGN OF THE MOUNTING SYSTEM

3.1 Basic Configuration

The basic configuration that is proposed for the mobile platform and its supporting structure is shown in figures 3.1, 3.2, and 3.3. The trolley system is designed to be retrofit to existing trusses; this eliminates the need for a special truss to be built solely for the system. Figures 3.1 and 3.2 show how the platform will be integrated with existing highway truss structures, and figure 3.3 is a close-up of the platform itself. The main components of the system are a trolley and a pair of tracks. The plan for the tracks is to use two aluminum C-channels running parallel to each other and spaced 12.5" apart. These tracks are connected to the bottom of the truss walkway using I-beams that double as track separators. The trolley is equipped with four wheels and rides along the tracks carrying an electronic monitoring device. The trolley is motorized via a front wheel drive system, and can be positioned at any desired location over traffic. The overall dimensions of the trolley and the mounted device are small; hence they will be relatively inconspicuous and will therefore be non-distracting to the driving public.

The mobile platform is able to accommodate many different monitoring devices. This is possible because of the use of a mounting plate (U-plate) that allows various shapes and sizes of monitoring devices to be mounted to the trolley. The U-plate has a set of holes for the device as well as a set of holes matching the trolley body holes. One shortcoming of this system is that each device may need a separate mounting plate. However, this is not a major problem since these plates are inexpensive and can be easily fabricated. The main advantage of the mounting plate idea is that the trolley itself will not have to be modified to accommodate a device.

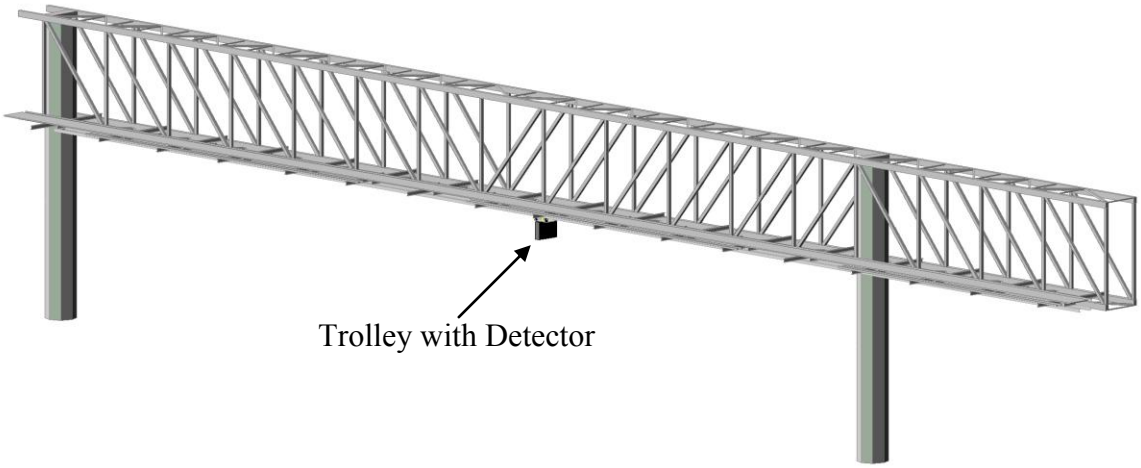

Figure 3.1a: Isometric View of Truss with Mounted Trolley and Detector

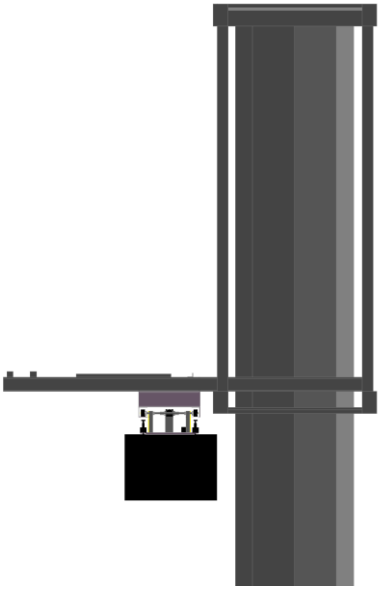

Figure 3.1b: Side View of Truss with Mounted Trolley and Detector

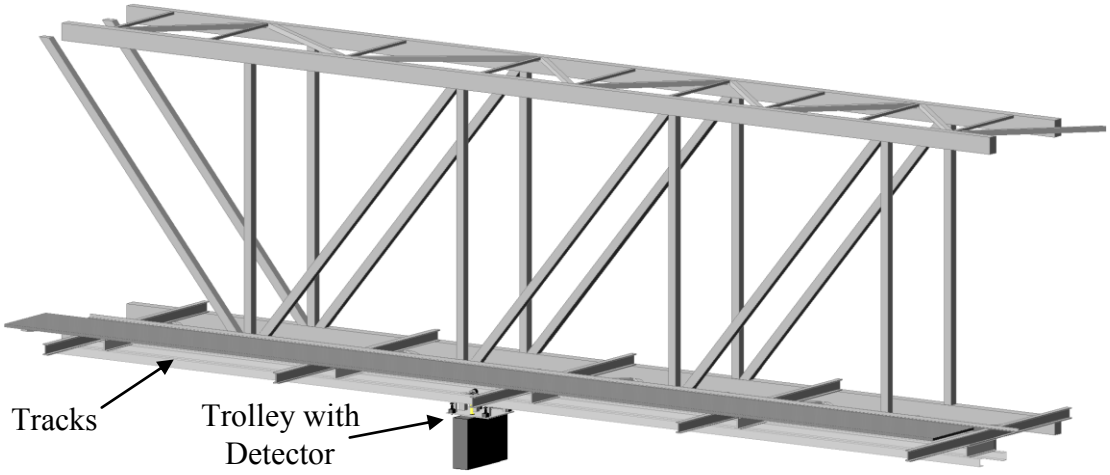

Figure 3.2: Close-Up of Trolley and Detector on Truss

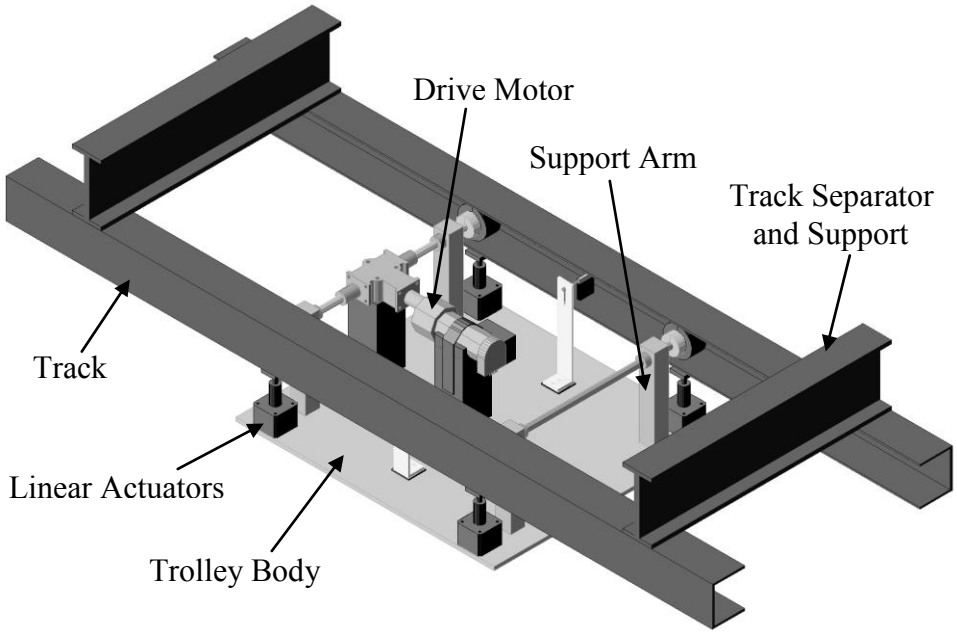

Figure 3.3: Trolley System (Mobile Platform)

3.2 The Trolley Components

The main components of the trolley (see figure 3.3) include a body, support arms, wheels, a drive system, and a static constraint system. The trolley body is an aluminum plate that is 18”x16”x1/4” in size. Four 1.25” square by 5.5” long aluminum support arms are connected to the trolley body using three #8-32 screws on each arm. Each support arm has two stainless steel bearings that are press fit into slots on opposite sides near the top of the arms. On the rear support arms, a single 16” long by 3/8” diameter stainless steel axle is fit through the bearings on both arms. Neoprene wheels with an aluminum hub are attached to the ends of the axle using integrated setscrews. For the front, two 6” axles are used. Each front axle is fit through the bearings of the corresponding support arm and connected to the gearbox using an aluminum shaft coupling. A wheel is connected to the outer end of each front axle. The axles overhang the wheels by about 1/4” to allow 3/8” diameter Delrin hemispheres to be glued to the ends of the axles. Shaft collars are used on the axles on both sides of the support arms at the rear and only on the inside of the support arms at the front.

To drive the system, a gear-motor and dual right angle gearbox are used. The gearbox and motor are both elevated to the proper height using a 2” square by 4.25” tall block of Delrin. These mounts are connected to the trolley body using 3 #10-24 screws for each mount. The motor is held to its mount using a Velcro strap and the gearbox to its mount using 3 #10-24 screws. With the gearbox output shafts attached to the two front axles, the input shaft is connected to the output shaft of the motor using a shaft coupling.

As in most design work, the configuration described above did not come in one easy iteration. Many changes and decisions were made before this final configuration was decided upon. Areas that required extensive design changes and decisions included the tracks, lateral constraint system, static constraint system, drive system, and power connection. The initial track design called for a round track and eight wheels (see figure 3.4). Because of the difficulty in mounting the trolley on the tracks, the number of wheels was reduced to four. A problem was then found in securing the trolley to the

round tracks. If the linear actuators were used, they would need to be rather complex to apply a firm hold on the tracks. This is why square tracks were adopted. Laterally constraining the trolley while moving was found to be rather difficult with the square track design. This led to the final channel track configuration. The channel tracks protect the wheel riding surface and the wheels themselves from rain, sun, and debris, and make laterally constraining the trolley very simple.

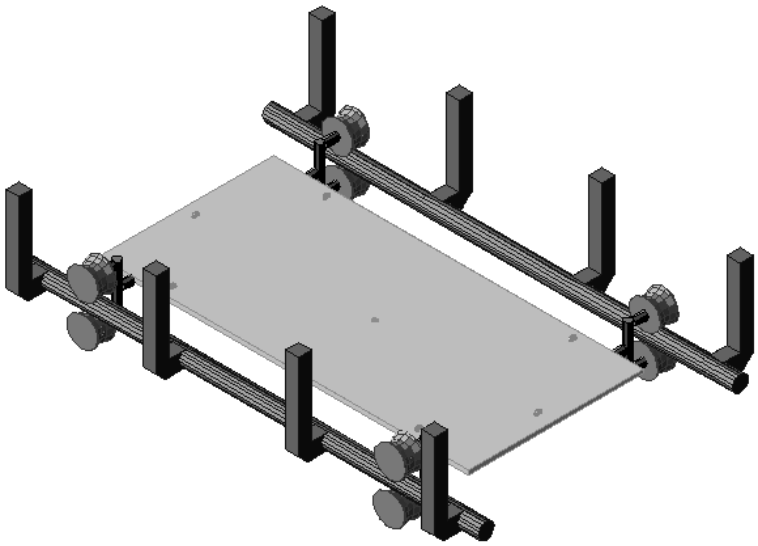

Figure 3.4: Round Track Trolley System

The trolley system weight will keep the trolley on the tracks vertically, but does not constrain it laterally. Although the channel shaped tracks will keep the trolley on the tracks preventing it from falling, the trolley could still get twisted while moving and be subject to lock up. With the square track design, the idea to use spring-loaded wheels on each support arm to ride against the inside of the tracks was considered (see figure 3.5a). This method of lateral constraint was found to be very difficult to implement and was the primary motivation for the track design change. With the channel tracks, laterally constraining the trolley was rather easy. To this end, a small Delrin hemisphere is attached to the overhanging axle ends (see figure 3.5b). Therefore, if the trolley were to twist, the hemispheres will rub smoothly on the inside of the tracks. This method proved to be a very easy way to prevent the trolley from locking up.

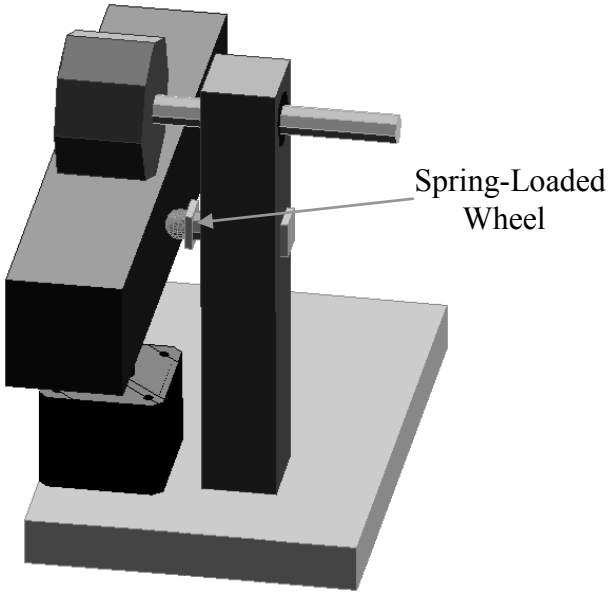

Figure 3.5a: Spring-Loaded Lateral Constraint Wheel

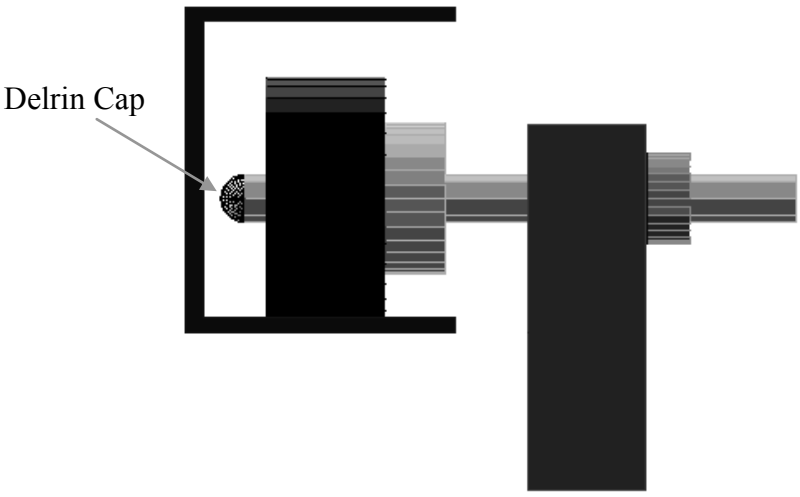

Figure 3.5b: Delrin Lateral Constraint Cap

Another design challenge that had to be met was to devise a method for holding the trolley firmly on the tracks when the trolley is stationary. The preliminary idea was to use power-off brake solenoids as a static constraint system to hold the trolley on the tracks. This type of solenoid uses a powered electro-magnet to retract an extension spring, and when depowered the spring extends the solenoid arm. The problem with this

type of solenoid is that the trolley could experience forces that are larger than the extension springs could handle. This brought on the search for a stronger type of static constraint system, which led to the use of screw type linear actuators. This type of actuator uses a permanent magnet to drive a screw, which in turn drives the actuator arm linearly. Four linear actuators, used to hold the trolley firmly in place over traffic, are connected to the trolley body underneath each wheel using four #4-40 screws for each actuator. These linear actuators provide a large holding force in a rather small package.

In order to move the trolley over lanes of traffic, a manual winch and cable drive system was originally contemplated. With this system, a cable would be looped through the truss and connected to two winches at the cable ends. One winch would pull the trolley out over traffic and the other would pull it back in. This system was found to have many flaws. For example, moving multiple trolleys on the same set of tracks would pose a serious challenge. It would be quite difficult to mount or dismount even a single trolley without the use of a bucket truck; and keeping the cable from sagging and preventing it from twisting the trolley would be problematic. Because of these difficulties, the winch and cable drive system was abandoned. The drive system that has been adopted uses a single motor and a dual right angle gearbox to drive the two front wheels. (see Figure 3.3) This arrangement allows a single motor to drive both wheels simultaneously and thus eliminates various coordination problems that would be associated with independently driven wheels.

3.3 Control System Concept

The trolley will be controlled remotely using radio frequency (RF) controllers. These RF controllers will be used to transmit commands to the motor, linear actuators, and mounted device. An optical encoder that comes with the motor will be used to determine the distance that the trolley has moved from a given position. To provide further precision in placing the trolley, the encoder is attached to the motor before a 65.5:1 gearbox. This means that the encoder's resolution will be multiplied by 65.5.

In addition to controlling the motor, the controller will also be used to control the linear actuators. The linear actuators will receive their basic commands, such as speed, direction, and enable/disable, through a special drive card. The controller will be linked to the drive card to manage the commands given to the actuators from the drive card. The controller will determine the distance that the linear actuator travels from its speed and steps per revolution (resolution). The distance between the linear actuator force distribution plate and the bottom of the tracks is known. However, the distance that the linear actuator needs to extend will be slightly larger than that distance, due to small displacements or defromations in the actuator, trolley body, and wheels. Tests will be performed to determine the exact distance that the linear actuators need to extend in order to apply the optimum holding pressure. The detailed implementation of an appropriate control strategy for the trolley is the subject of another design project.

3.4 Power Management

The issue of power supply to the trolley system and its attendant problems were discussed in chapter 1. After a thorough review of the difficulties, the following method of supplying power to the trolley was developed. This method involves using the tracks themselves to supply power to the trolley. To do this, one side of the tracks would be connected to the positive terminal of the power supply and the other track to the negative terminal. The tracks would be electrically isolated from the rest of the truss and trolley via rubber shims, grommets, and non-conductive washers. The physical power connection between the tracks and the trolley would be made using metal brushes attached to the trolley and that would continuously rub on either side of the track. This method of supplying power to the trolley allows the trolley to be a freely moving system that is uncoupled from other trolleys on the track. The trolleys could be precisely positioned and repositioned quickly and easily. This creates a truly wireless overhead detector mounting system.

While the trolley is in motion, there is a slight possibility of the brushes losing contact with the tracks. If this were to happen the trolley would lose all power and control causing the trolley to be stranded. To counteract this possibility, a 12 VDC battery, capable of maintaining sufficient power to the trolley, will be connected in parallel to the track supplied power. This backup battery ensures that the trolley would maintain power if the brushes were to lose contact with the tracks. The backup battery would most likely only need to be used for very short periods of time. However, the battery will have enough power to drive the trolley continuously for the time necessary to bring the trolley to the end of the tracks where it can be accessed by an operator.

The actual method of getting power to the tracks via the truss may include trenching and laying of electric cables. However, many trusses already have power supplied to them for the sign lights. In such cases, power may be drawn off of the existing power supply to supply power to the tracks.

3.5 Mounting and Dismounting the Trolley

It will be necessary, from time to time, to remove the trolley from the tracks for the purpose of replacing the monitoring instrument it carries, or for general maintenance. One way to do this is to command the platform to move to one end of the truss, and then bring a bucket truck to the site and hoist a person up to the truss. As stated earlier, this approach is undesirable, as it can lead to unnecessary delays from the need to coordinate activities between several offices of the department of transportation.

To resolve this problem, a special installation procedure is proposed. The method calls for the use of a winch attached to the truss at one of its ends, as well as two sets of maneuvering cables to hoist and place the trolley onto the tracks (see Figures 3.6, 3.7, and 3.8). First, the winch is lowered and a four-point electromagnet harness (Figure 3.6) is connected to the winch cable. Then the harness' electromagnets are powered and connected to four steel plates mounted on top of the trolley near the corners. Next, the

maneuvering cable electromagnets are powered and attached to steel plates on the underside of the trolley (see Figures 3.7 and 3.8). The trolley is checked for stability and then hoisted by the winch to the level of the tracks. The winch has a preset stop so the trolley will stop with its wheels at the level of the tracks. Once thus positioned vertically, the trolley is aligned horizontally using the maneuvering cables, and then pushed forward onto the tracks. To facilitate placing the trolley on the tracks, the ends of the tracks are flared, allowing a reasonable amount of deviation in horizontal alignment. With the help of the trolley drive system and back up battery, the trolley is pulled completely onto the tracks, and the maneuvering cable magnets are de-powered so that the cables fall to the ground. The winch cable electromagnets are also de-powered, and the cables raised from the trolley. Once the trolley is moved out of the way, the winch can be lowered again so that the harness cables can be retrieved, and the winch is returned to its normal position on the truss. The trolley will then be able to be positioned along its tracks using the trolley drive system.

To remove the trolley from the tracks, the winch is lowered and a single large magnet is attached to the end of the winch cable and raised just above the level of the highest point of the trolley. The trolley is then driven to the end of the tracks until it is underneath the winch. The large magnet is lowered until it makes contact with a steel plate attached to the trolley near the trolley's center of gravity. Then, some slack is let out of the winch cable and the trolley is driven off of the tracks. At this point the trolley will be free from the tracks and dangling in the air, and the trolley operator may lower the trolley to the ground.

The method described above gives the trolley operator direct access to the support platform and its instrument without having to involve other personnel and equipment, and will thus save both time and money.

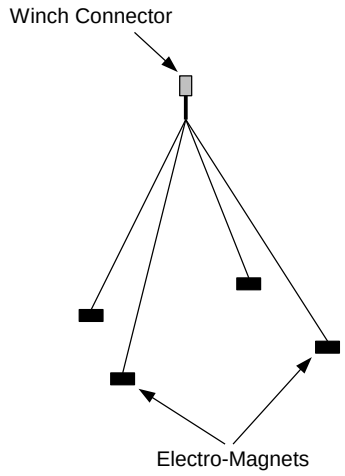

Figure 6: Four-Point Electro-Magnet Harness

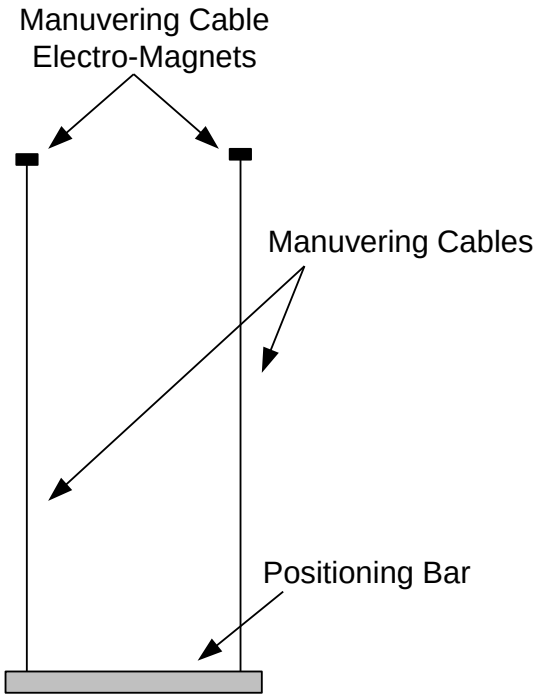

Figure 3.9: Maneuvering Cable Assembly

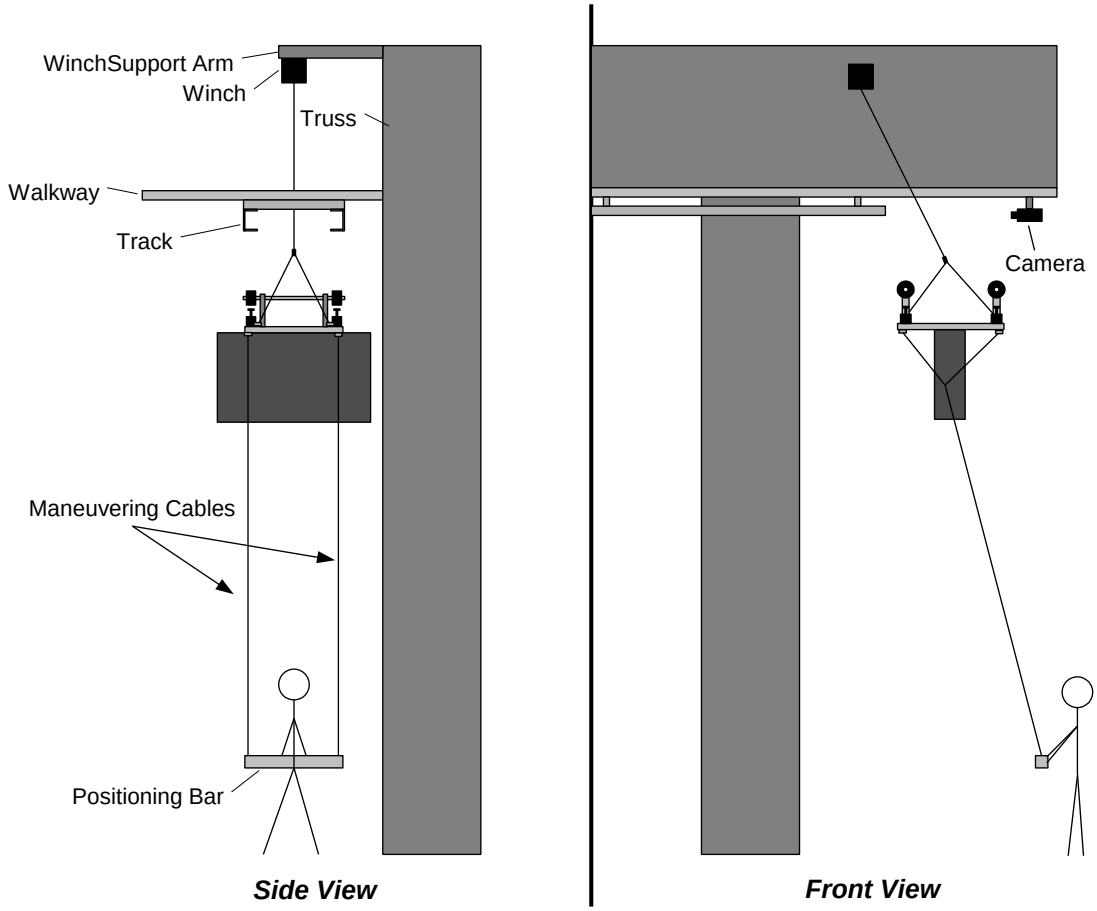

Figure 3.10: Trolley Installation Process

To remove the trolley from the tracks, a single large magnet will be used. First, the winch will be lowered and a single large magnet will be attached to the end of the winch cable and raised just above the trolley. The trolley will then be driven to the end of the tracks until it is underneath the winch. The large magnet will be lowered onto a steel plate on the trolley positioned near the center of gravity of the trolley. After this, some slack will be let out of the winch cable and the trolley will be driven off of the tracks. At this point the trolley will be free from the tracks and dangling in the air at which time the trolley operator may lower the trolley to the ground.

CHAPTER 4

ANALYSIS OF PLATFORM SYSTEM COMPONENTS

This chapter gives a brief presentation of the analysis behind the choice of the major components of the trolley system. The components that were studied include the axles, the bearings, the shaft collars, the tracks, support arms, shaft couplings, the trolley body, the U-plate, the motor, and the linear actuators. A study of the system's vibration response is also presented.

4.1 Axle Analysis

There are many important components on the trolley that need to be properly chosen in order to prevent failure. One of these components is the set of axles. The axles were chosen to be made of 303 stainless steel, instead of aluminum. The main reason for this design choice is that aluminum is a weaker material. By using steel axles, it is possible to use a relatively small diameter shaft and maintain high strength. As seen in the following analysis, the steel axles are approximately 2.8 times stronger than the aluminum axles of the same size. The axles were modeled using two different methods in order to fully assess their strength characteristics. Each model assumed a 50 lb. combined trolley and mounted device total weight.

4.1.1 Point Load Axle Model – Front Axle

One of the front axles is shown in figures 4.1a and 4.1b, and its free body diagram is drawn in figure 4.1c. The front axle system consists of two separate axles that are connected through the gearbox. To simplify the analysis, only one front axle was

examined with one-quarter of the total trolley weight applied. This is acceptable because both axles undergo the same state of stress, and the total weight on the front axle system is half of the total trolley weight. Using the model of Figure 4.1b, the axle problem is a statically indeterminate one, with fixed-pinned boundary conditions. Yet, general formulas for the forces, moments, and deflections in this case are readily available in handbooks, and some of these are given below.

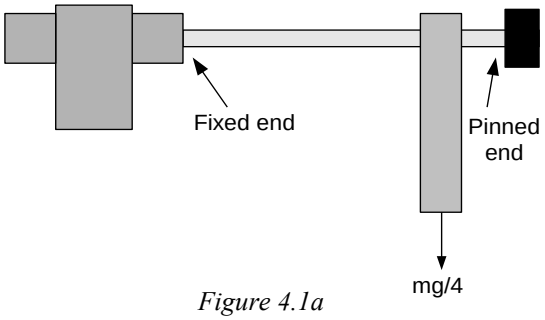

Figure 4.1a

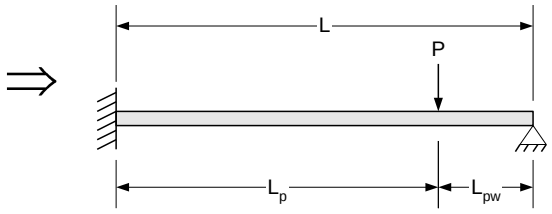

Figure 4.1b

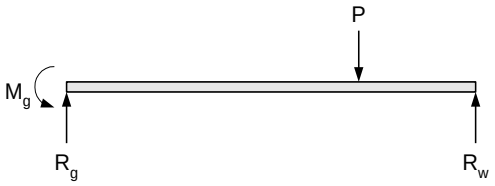

Figure 4.1c

$$M_g = \frac{PL_{pw}}{2L^2}(L_{pw}^2 - L^2)$$

$$M_{gp} = \frac{PL_{pw}}{2L^3}\left[L_{pw}^2 L - L^3 + x(3L^2 - L_{pw}^2)\right]$$

$$M_{pw} = \frac{PL_p^2}{2L^3}(3L^2 - 3Lx - L_p L + L_p x)$$

$$R_w = \frac{PL_p^2}{2L^3}(3L - L_p)$$

$$R_g = \frac{PL_{pw}}{2L^3}(3L^2 - L_{pw}^2)$$

Here, M_g is the bending moment at the fixed (gearbox) end; M_{gp} is the bending moment at a point on the axle a distance x from the fixed (gearbox) end, and located between the gearbox and the load; M_{pw} is the bending moment at a similar point between the load and the wheel; R_w and R_g are the reaction forces at the wheel and at the gearbox. From these equations, the maximum moment was found to be M = 11.94 in.-lb. at a distance of 4.5 in. from the gearbox (i.e. - at the point of load application). The reaction forces were

found to be R_w = 7.9 lb. and R_g = 4.6 lb. The axle deflection, stresses due to torsion and bending of the axle, principal stresses, maximum shear stress, and von Mises stress were also calculated. From these, the state of stress on the axles due to the combined effect of the motor torque and the load P could be determined. For the deflections, the following equations were used:

$$y_{gp} = \frac{PL_{pw}x^2}{12EIL^3}\left[3L(L_{pw}^2 - L^2) + x(3L^2 - L_{pw}^2)\right]$$

$$y_{pw} = y_{gp} - \frac{P(x-a)^3}{6EI}$$

where, E is the modulus of elasticity and I is the moment of inertia. These equations give the deflection as a function of distance along the axle. The first equation, y_{gp}, gives the vertical deflection of a point, x, on the axle located between the gearbox and the point of load application; and the second, y_{pw}, gives the deflection of a point on the axle between the point of load application and the wheel. From these equations the maximum deflection of the axle was found to be y_{max} = 0.0008 in. at a distance of 3.84 in. from the gearbox, slightly to the left of the point of load application. A plot of the vertical displacement along the axle was made (see figure 4.4) to help both visualize the axle deflection and find the maximum point of displacement. In addition to this, shear and moment diagrams are shown in figures 4.2 and 4.3.

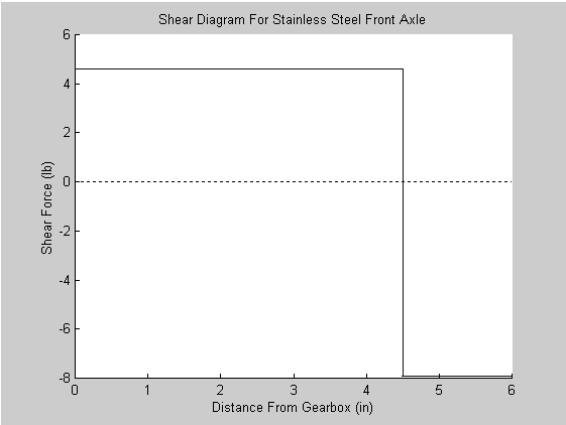

Figure 4.2: Front Axle Shear Diagram

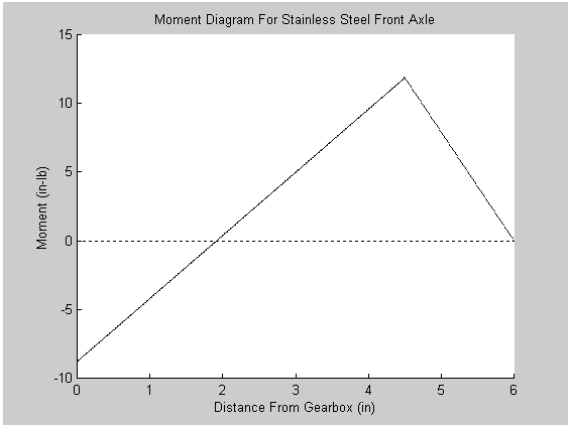

Figure 4.3: Front Axle Moment Diagram

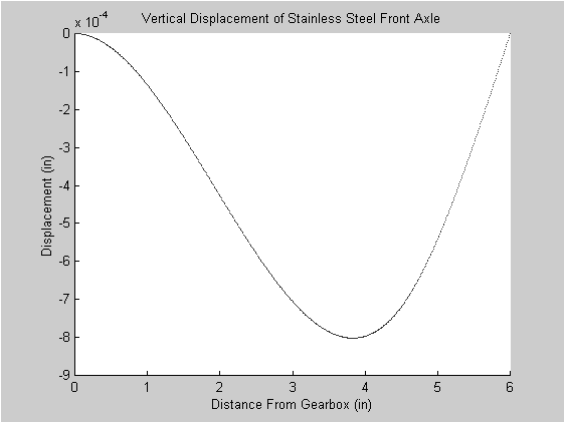

Figure 4.4: Front Axle Deflection

Following the force and deflection calculations, the stresses due to bending and torsion of the axle were calculated using the following equations (during normal operation, there should be no significant axial force, therefore the contributions from such forces are neglected):

$$\sigma_{z\theta} = \frac{Tr}{J} \quad , \text{ where } J = \frac{\pi d^4}{32} \text{ , } T = \text{applied torque, and } r = \text{axle radius}$$

$$\sigma_{zz_b} = \sigma_{zz} = \frac{Mr}{I} \quad , \text{ where } I = \frac{\pi d^4}{64} \text{ and } M = \text{maximum moment, and } r = \text{axle radius}$$

where, $\sigma_{z\theta}$ is the stress due to torsion and σ_{zz_b} is the stress due to bending.

These equations show that the stress due to torsion of the front axle is $\sigma_{z\theta}$ = 2897 psi and the stress due to bending is σ_{zz_b} = 2307 psi. After this, the principal stresses were calculated and from them the maximum shear stress and von Mises stress were calculated. The following equations were used:

$$\sigma_1 = \frac{\sigma_{zz}}{2} + \sqrt{\left(\frac{\sigma_{zz}}{2}\right)^2 + \sigma_{z\theta}{}^2} \qquad \tau_{max} = \frac{\sigma_1 - \sigma_2}{2}$$

$$\sigma_2 = \frac{\sigma_{zz}}{2} - \sqrt{\left(\frac{\sigma_{zz}}{2}\right)^2 + \sigma_{z\theta}{}^2} \qquad \sigma' = \sqrt{\sigma_1^2 - \sigma_1\sigma_2 + \sigma_2^2}$$

where, σ_1 and σ_2 are the pricipal stresses, τ_{max} is the maximum shear stress, and σ' is von Mises stress.

The maximum shear stress on the axles is τ_{max} = 3118 psi and the von Mises stress was found to be σ' = 5523 psi. Next, the angular deflection of the axles was calculated to

determine their torsional stiffness, and the angular displacement per unit length was also calculated. The following equations were used:

$$\theta = \frac{TL}{GJ} \qquad\qquad \frac{\theta}{L} = \frac{32T}{\pi d^4 G}$$

where, T is the torque, L is the axle length, d is the axle diameter, G is the shear modulus of elasticity, and J is the polar moment of inertia. From these equations the total angular deflection of the axle was found to be $\theta = 0.5°$ corresponding to an angular deflection per unit length of $\frac{\theta}{L} = 0.083 \ \frac{deg.}{in.}$.

The factor of safety was calculated next. There are a number of ways to determine the factor of safety and the method used in this case was accomplished via the distortion energy theory. By comparing the von Mises stress to the yield strength of the axle, the factor of safety can be obtained. In doing this, the factor of safety for the axle was found to be $\eta = 6.34$. This large value proves that using stainless steel for the front axles will be more than satisfactory.

After finding the performing an analysis on the stainless steel axle, all of the above calculations were performed again using Aluminum 6063 as the axle material. The shear and moment diagrams are identical to those for the stainless steel axle, since the diagrams are based on the loading conditions, not the material. For the aluminum axle, the maximum deflection was found to be almost 3 times larger, having a value of $y_{max} = 0.0021$ in. The angular deflection of the axle was also found to be nearly 3 times larger with a value of $\theta = 1.4°$. As for the factor of safety, it was found to be just under 2 times smaller than that for the stainless steel axle having a value of $\eta = 3.62$. The figure below shows a comparison of the deflection along the axle for the aluminum and stainless steel axles.

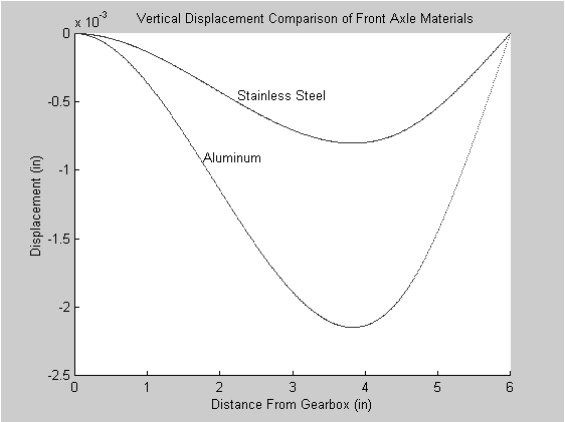

Figure 4.5: Front Axle Deflection Material Comparison

This plot shows that the stainless steel axle has far less deflection than the aluminum axle. However, the aluminum axle only deflects a small amount illustrating that both materials are within tolerable limits.

4.1.2 Point Load Axle Model – Rear Axle

Following the front axle analysis, the rear axle was analyzed. A free body diagram of the rear axle was drawn to help determine the forces and moments on the axle. The rear axle was less complex to analyze because of its simple support loaded condition. The rear axle can be modeled as a simply supported shaft with two point loads. This again is a common loading condition and therefore generic equations for the forces, moments, and deflections are available in handbooks. The equations used are shown below:

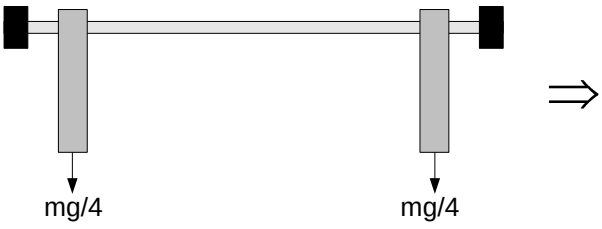

Figure 4.6a

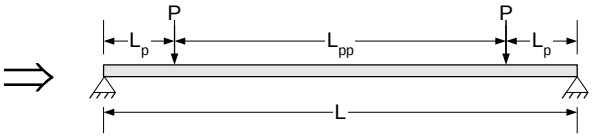

Figure 4.6b

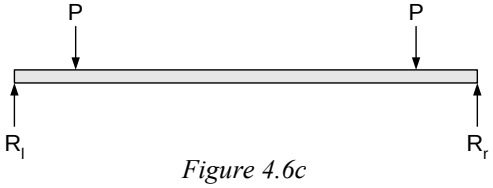

Figure 4.6c

$$M_{lp} = Px$$

$$M_{pp} = PL_p$$

$$M_{pr} = P(L - x)$$

$$R_l = R_r = P$$

Here, M_{lp} is the bending moment at a point, x, along the axle between the left wheel and the first (left) load; M_{pp} is the bending moment at a point along the axle between the two loads; and M_{rp} is the bending moment at a point along the axle between the second (right) load and the right wheel. These simple equations led to the determination of the maximum moment as being M = 18.87 in.-lb. This maximum moment is experienced everywhere between the two applied loads, in other words, everywhere between the trolley support arms. The reactions on the left and right wheels were found to be $R_l = R_r = 12.5$ lb. Below are the shear and moment diagrams to help visualize the force and moment along the axle.

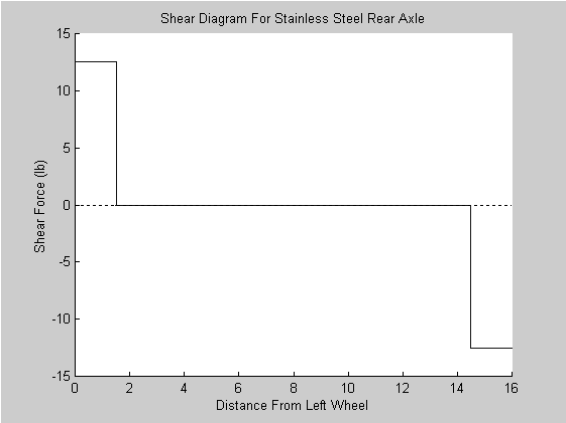

Figure 4.7: Rear Axle Shear Diagram

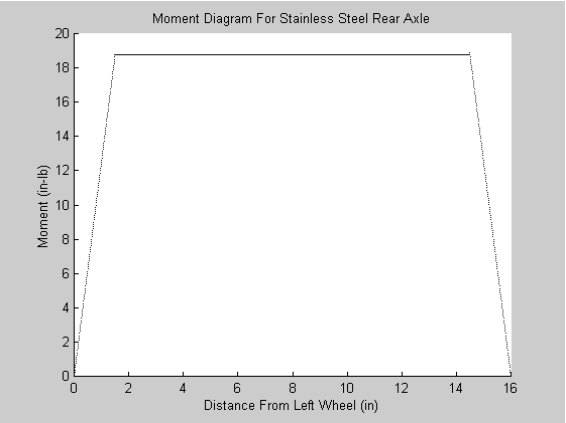

Figure 4.8: Rear Axle Moment Diagram

After the forces and moments on the axle were determined, the next step was to determine the maximum deflection of the axle. This was done using the following equations:

$$y_{lp} = \frac{Px}{6EI}(x^2 + 3L_p^2 - 3LL_p)$$

$$y_{pp} = \frac{PL_p}{6EI}(3x^2 + L_p^2 - 3Lx)$$

$$y_{pr} = \frac{P(L-x)}{6EI}[(L-x)^2 + 3L_p^2 - 3LL_p]$$

$$y_{max} = \frac{PL_p}{24EI}(4L_p^2 - 3L^2)$$

From these vertical displacement equations, the maximum deflection was found to be y_{max} = 0.022 in. at the center of the axle. The equations for y_{lp}, y_{pp}, and y_{rp} determine the deflection of the axle between the left wheel and first load, between the two loads, and between the second load and right wheel, respectively. These equations were used to create a plot (see figure 4.9) of the total deflection along the axle.

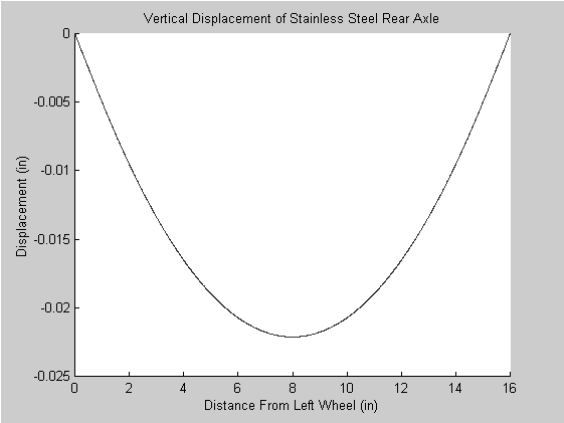

Figure 4.9: Rear Axle Deflection Plot

After obtaining the axle displacement, a complete stress analysis was performed to determine the rear axle's state of stress. The equations used to perform the stress analysis on the rear axle are identical to those used on the front axle. However, the rear axle is free rolling meaning that there is not a torsional force on the axle. As with the front axle, the axial force is negligible. Therefore, the stress due to bending is the only applied force to the rear axle. The equation for the stress due to bending gives the stress to be σ_{zz_b} = 3645 psi. This is also the same value for the first principal stresses and von Mises stress. The maximum shear stress was found to be half of the bending stress. From these values, the factor of safety was determined to be η = 9.6.

After evaluating the stainless steel rear axle, the material was changed to aluminum 6063 and the same analysis was performed. There was a considerable difference between the two materials behavior. Below is a plot of the difference between the vertical displacements along the axle.

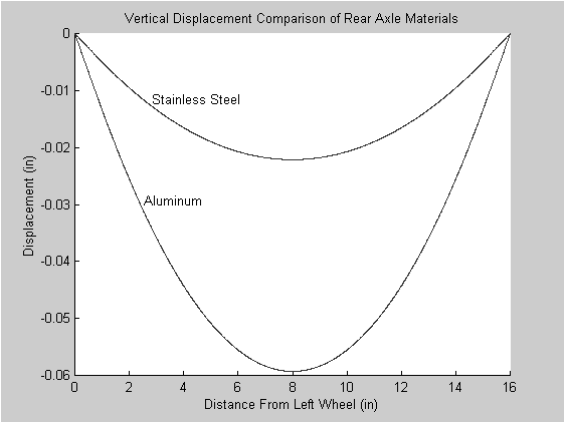

Figure 4.10: Rear Axle Deflection Material Comparison

In this plot it can be seen that the aluminum axle deflects much more than the steel axle. In fact, the aluminum axle underwent a deflection of over 2.6 times that of the steel having a value of $y_{max} = 0.059$ in. Even with this considerable difference in deflection, the factor of safety for the aluminum axle is still rather large being $\eta = 5.5$.

4.1.3 Cantilevered Axle Model – Both Axles

The above "point load" models for the front and rear axles are worst-case scenarios. This is because it is assumed a point load is applied to the axles to simulate the weight of the support arms. In reality, the support arms are 1.25" wide have bearings that impose a tight fit on the axles. This width and tight fit on the axles allows for the assumption that a single axle can be modeled as two cantilevered axles. With the cantilevered assumption, there is no need to perform an analysis on the front and rear axles individually because they are both subject to the same loading conditions. In addition, the section of the axle between the support arms should ideally have no applied transverse shear load. The front axle may experience a small transverse shear load due to the gearbox movement from small deflections of the trolley body. Using this seemingly valid assumption, a second analysis was performed on the axles.

In doing the cantilevered axle analysis, a free body diagram was constructed and used as seen below. Since equations for a cantilevered beam are readily available, the equations in table A-9 of the book *Mechanical Engineering Design, 5th ed.* (Ref. 8) were used for simplicity. To do the analysis, the axle is assumed to be cantilevered at the

support arm with a point load at the wheel. For this case, an upward force is applied to the bottom of the wheel, instead of the actual loading of a downward force being applied at the support arm. This is necessary due to the cantilevered assumption and does not affect the results. In addition, the force at the wheel is assumed to be a point load at the center of the wheel. The wheel is actually one inch wide, but a point load is assumed for simplicity.

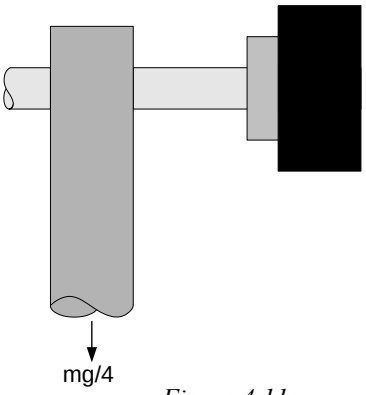

Figure 4.11a

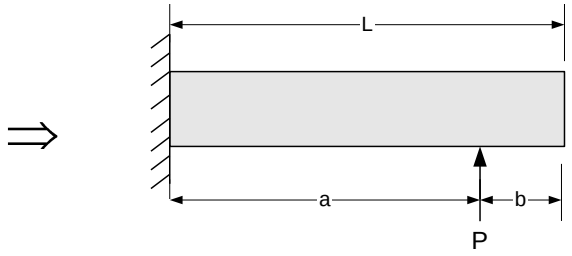

Figure 4.11b

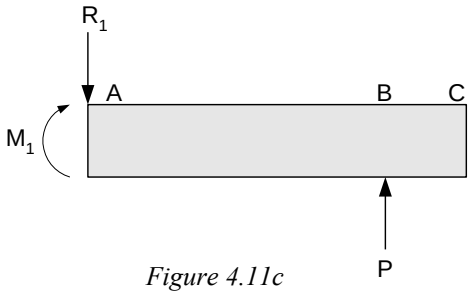

Figure 4.11c

$$M_1 = -Fa$$
$$M_{AB} = P(x-a)$$
$$M_{BC} = 0$$
$$R_1 = P$$

Here, M_1 is the bending moment at the cantilevered (support arm) end; M_{AB} is the bending moment at a point, x, along the axle between points A and B; M_{BC} is the bending moment at a point along the axle between points B and C; and R_1 is the reaction force at the cantilevered end of the axle. The above equations show that the reaction force at the support arm was equal to the applied force giving R_1 = 12.5 lb. The maximum moment was found to be at the support arm with a value of M = M_1 = 20.9 in.-lb. Below are the shear and moment diagrams for the cantilevered axle.

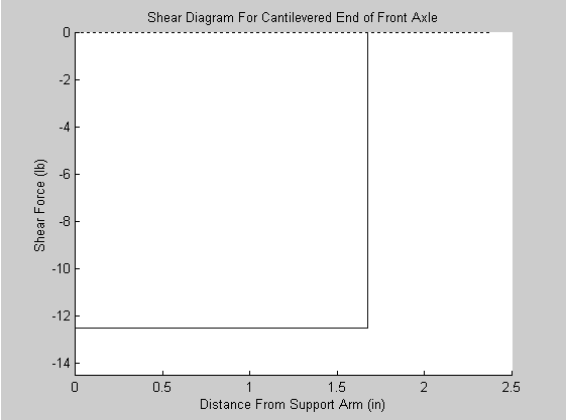

Figure 4.12: Cantilevered Axle Shear Diagram

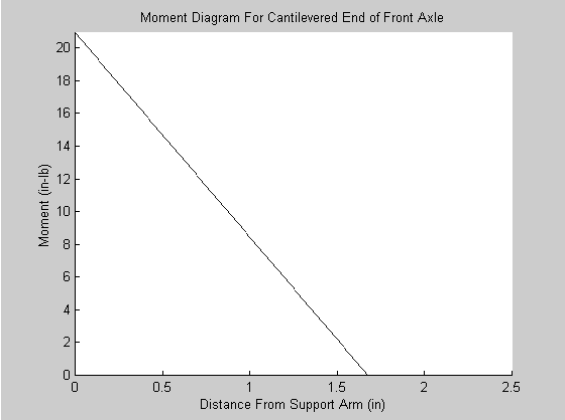

Figure 4.13: Cantilevered Axle Moment Diagram

With the forces and moments determined, the state of stress on the axle could then be calculated. This was done using the same equations as for the point load model analysis. The bending stress was found to be σ_{zz_b} = 4044 psi, which was also the same value as the principal and von Mises stress. The maximum shear stress was found to be half of the bending stress with a value of τ_{max} = 2022 psi. From these values, the factor of safety was calculated to be η = 8.65.

The next step in the analysis was to determine the vertical deflection of the axle. This was done using the following equations:

$$y_{AB} = \frac{Px^2}{6EI}(x - 3a)$$

$$y_{BC} = \frac{Pa^2}{6EI}(a - 3x)$$

$$y_{max} = \frac{Pa^2}{6EI}(a - 3L)$$

From these equations the maximum deflection was found to be y_{max} = 0.0012 in. The partial deflections, y_{AB} and y_{BC}, are the displacements at a point, x, between the support arm and load, and between the load and the end of the axle, respectively. These equations were used to create the vertical displacement plot seen below.

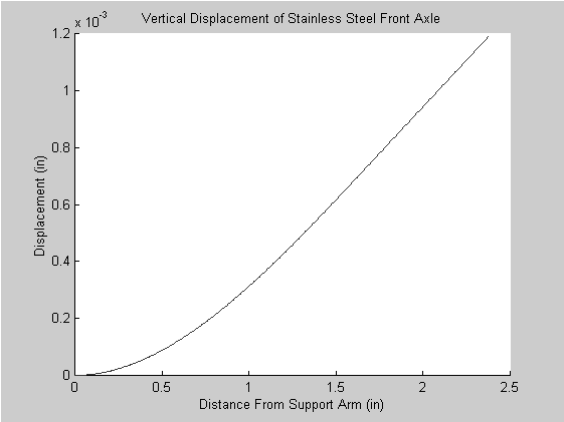

Figure 4.14: Cantilevered Axle Deflection Plot

With the stainless steel axle analyzed, the next step was to perform the same calculations for an aluminum axle. After performing the analysis, the maximum axle displacement for the aluminum axle was found to be $y_{max} = 0.0032$ in. This is seen to be nearly three times the deflection as that of the stainless steel axle. However, the factor of safety of the aluminum shaft was still rather large being $\eta = 4.9$. The plot below shows the vertical displacement comparison between the stainless steel and aluminum axle materials.

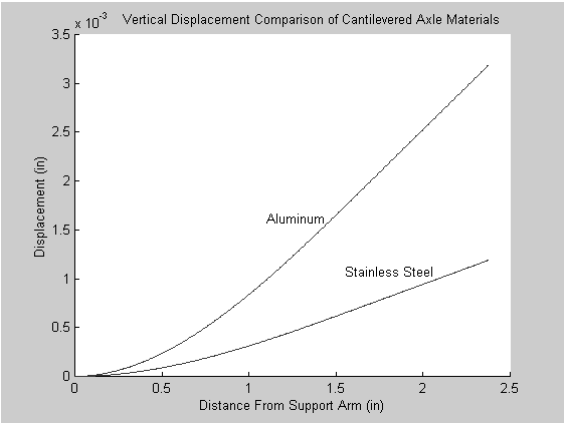

Figure 4.15: Cantilevered Axle Deflection Material Comparison

In comparing the point load axle model and the cantilevered axle model methods, the cantilevered model was found to be the most accurate. The point load models gave a slightly improper representation of the axles by assuming a pinned support arm, when the axles are actually connected through a 1.25" piece of aluminum. The thickness of the

support arms causes the axles to experience more of a cantilevered connection than a pinned connection. The differences between the deflections, stresses, and factors of safety of each model are not significant, and the cantilevered model gives a good medium between the rear and front axle point load models. Therefore, the less complex cantilevered model can be used for analysis without loss of accuracy.

After performing a through analysis on the front and rear axles of the trolley, the stainless steel axle material was the chosen material. Using stainless steel gives what seems to be an excessively large factor of safety. However, in considering the application of the trolley system, safety is of the utmost importance. The trolley will be suspended over live traffic, and if it fell a major catastrophe is very likely. Therefore, using stainless steel axles helps ensure that the trolley system will maintain structural integrity and not drop onto traffic.

4.2 Bearing Analysis

The bearings were rather easy to choose. The trolley will need to use simple ball bearings to support the system. A stainless steel, double-shielded ball bearing was decided upon to allow for strength and durability. The bearings chosen have a dynamic load rating of 569 lb. and a static load rating of 273 lb. The trolley will primarily be operated in a static position, and only a minute portion of its life will involve bearing rotation. For this reason, the dynamic load rating is not as important as the static load rating. Furthermore, the total weight of the trolley system and laser detector is approximately only 50 lb. Since there are eight bearings being used (two at each wheel), the combined total load supporting capability of the bearings on the trolley is 2184 lb. This proves that the bearings will be more than adequate for this application.

The only decision that needed to be made for the bearings is the type of lubrication and shielding. A double-shielded bearing was used because the trolley would be stationary for long periods of time and exposed to the environment. By having both sides of the bearing shielded, the bearing balls would be protected from debris thereby improving the

life and reliability of the bearings. For the choice of lubricant, there are two main types: grease or oil. In order to choose the proper lubricant for this application the book *Mechanical Engineering Design, 5th ed.* (Ref. 8) was consulted. From this book, the following table on page 470 was referred to:

USE GREASE WHEN:	USE OIL WHEN:
1. The temperature is not over 200°F.	1. Speeds are high.
2. The speed is low.	2. Temperatures are high.
3. Unusual protection is required from the entrance of foreign matter.	3. Oiltight seals are readily employed.
4. Simple bearing enclosures are desired.	4. Bearing type is not suitable for grease lubrication.
5. Operation for long periods without attention is desired.	5. The bearing is lubricated from a central supply which is also used for other machine parts.

Table 4.1: Lubrication Selection

From this table it is obvious to see that grease is the best option for bearing lubrication. Every item in the reasons to use grease column is an aspect that the trolley obeys or desires. Therefore, grease was the chosen bearing lubrication.

4.3 Shaft Collar Analysis

The shaft collars are another component that only needs minor decision making to choose the best collar for the application. They are used to axially constrain the trolley axles. The primary decision in choosing the shaft collar is the type of clamping mechanism that is used. There are two main types to choose from: clamp type or set screw type. The clamp type is a method that does not mar the shaft. The collar is secured to the shaft by tightening a screw that decreases the bore diameter of the collar. In essence, the collar squeezes the shaft tightly. The setscrew type uses a small setscrew that is screwed

through the collar and into the shaft. More than one setscrew can be used for increased holding strength. This method of tightening most often mars the shaft slightly. Another option to using the setscrew type of fastener is to use a roll pin along with the setscrew. A roll pin is a small "C" shaped pin that can expand and contract slightly. To use it, a small hole is drilled through the collar and shaft co-axially. The roll pin is then pressed into the holes, creating a relatively permanent attachment between the collar and shaft. A roll pin is used when high axial forces are to be applied to the collar.

For the trolley application, the clamp style shaft collar was used. This type was chosen because the trolley axles will only experience small axial forces. On the front axle, the gearbox will axially constrain the axles and the shaft collars are used mainly for added support. On the rear axle, the collars are necessary to axially constrain the axle. The collars take all of the axial force generated on the rear axle, however this force is very small under normal operation. The only time when a large axial force could be applied to the axle is if one drive wheel slips or sticks creating a torque on the trolley. This would cause the Teflon lateral constraint cap on one side of the rear axle (depending on the direction which the trolley is moving) to hit the inside of the track, and consequently produce an axial force on the rear axle. This axial force has been calculated via a dynamic analysis of the trolley body.

To simulate one drive wheel slipping or getting stuck while moving forward, a model of the trolley body with one corner constrained from translating, but free to rotate, was used as seen below. This simulates the worst-case scenario, being that the trolley is moving at full speed and one drive wheel instantaneously stops. To begin with, the maximum speed of the trolley must be calculated.

$\square$ $motor\ speed = 71\ RPM$

$\square$ $wheel\ circumference = \pi d = 3.14(2\ in.) = \underline{6.28\ in.}$

$v = (71\ \frac{rev}{min})(6.28\ \frac{in}{rev})(\frac{1}{60}\ \frac{min}{sec}) \quad \Rightarrow \quad \underline{\underline{v = 7.43\ \frac{in}{sec}}}$

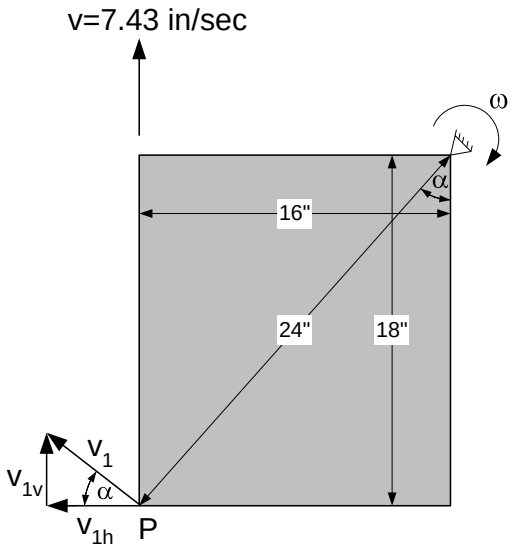

Figure 4.16: Trolley Body Rotation With One Wheel Slipping/Sticking

After determining the maximum speed of the trolley, the next step is to calculate the angle α and the angular velocity ω seen in figure 4.16 as follows (Ref. 9):

$$\alpha = \tan^{-1}\left(\frac{16}{18}\right) \quad \Rightarrow \quad \underline{\alpha = 41.6°}$$

$$\omega = \frac{v}{r} = \frac{7.43\ \frac{in}{sec}}{16\ in} \quad \Rightarrow \quad \underline{\omega = 0.464\ \frac{rad}{sec}}$$

Next, the velocity v_1 at the opposite rear corner of the trolley body is determined. The velocity v_1 is directed at an angle of 41.6° from the rear edge of the trolley because it must be perpendicular to the line segment from the constrained corner to the point P. Since the axial force on the rear axle is desired, only the horizontal component, v_{1h}, of the velocity v_1 will be needed.

$$v_1 = \omega r = 0.464\ \frac{rad}{sec}(24\ in.) \quad \Rightarrow \quad \underline{v_1 = 11.14\ \frac{in}{sec}}$$

$$v_{1h} = v_1 \cos\alpha = (11.14\ \frac{in}{sec})\cos 41.6° \quad \Rightarrow \quad \underline{\underline{v_{1h} = 8.33\ \frac{in}{sec}}}$$

Knowing the velocity at which the rear axle will impact the inside of the track brings on the use of Newton's second law, which can be written as:

$$F = m\frac{\Delta v}{\Delta t}$$

Using this form of Newton's second law and an estimated impact time of $\Delta t = 0.1$ sec, the applied axial impact force to the rear axle can be approximated.

$\square$ 50 *lb. trolley weight* $\Rightarrow$ $m = 1.55$ *slugs*

$\square$ $\Delta v = v_{1h} = 8.33 \ \frac{in}{sec} = 0.694 \ \frac{ft}{sec}$

$$F = m\frac{\Delta v}{\Delta t} = (1.55 \ slugs)\left(\frac{0.694 \ \frac{ft}{sec}}{0.1 \ sec}\right) \quad \Rightarrow \quad \underline{\underline{F \cong 10.76 \ lb.}}$$

Now this calculated axial force on the rear axle can be compared to the slip torque of the shaft collar. Figure 4.17 shows the clamp type shaft collar data. This table can be interpolated to determine the approximate slip torque for a 3/8" bore diameter. Interpolation, however, is not necessary since the figure shows that a 1/4" bore shaft collar using a clamp screw fastening torque of only 30 oz.-in. will withstand a slip torque of 5 in.-lb. This 5 in.-lb. slip torque equates to an axial holding force of approximately 40 lb as follows:

$$\frac{slip \ torque}{bore \ radius} = \frac{5 \ in.-lb.}{0.125 \ in.} = \underline{\underline{40 \ lb. \ holding \ force \ at \ the \ shaft \ surface}}$$

The slip torque is seen to increase with bore diameter, therefore a 3/8" bore shaft collar will easily be able to withstand the 10.76 lb. applied axial impact force on the rear axle. Moreover, the rear axle will be equipped with four of these shaft collars (two at each support arm), which will ensure that the rear axle will be axially constrained.

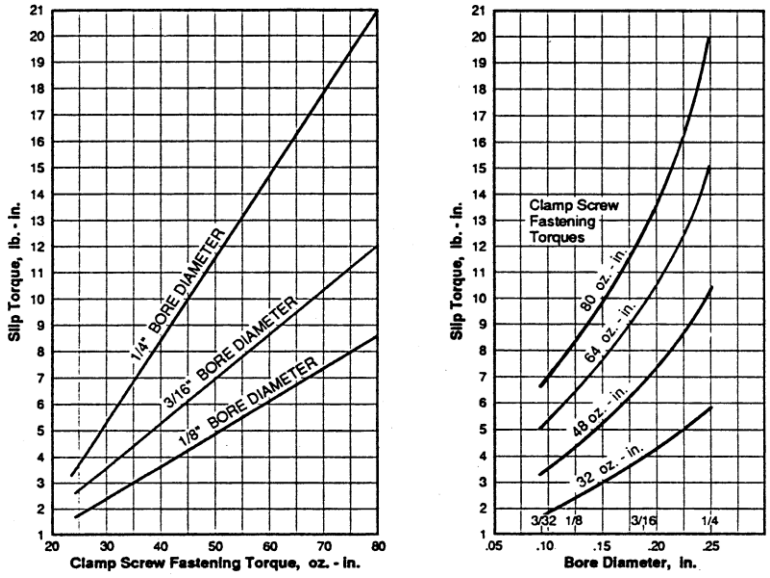

Figure 4.17: Shaft Collar Slip Torque
(figure from *Handbook of Inch Drive Components, SDP/SI Catalog* p.6-5, Ref. 10)

4.4 Shaft Coupling Analysis

The shaft couplings can be chosen without computation. This is because the shaft coupling is only used to transmit torque, so only a torque requirement needs to be satisfied. Most shaft coupling manufacturers supply a torque rating which eliminates the need to calculate one. There are many different types of shaft couplings on the market. In the trolley application, a flexible coupling is needed to allow for inexact shaft alignment. Within the flexible coupling category, there are subcategories of different types to choose from including helical, bellows, and rubber style couplings. The type chosen for the trolley system is a helical flexible shaft coupling. This type was chosen because of its environmental robustness as well as its compact size. The particular coupling chosen allows for maximum misalignments of 5° angular, 0.01" parallel offset, and 0.01" axial motion. These allowable misalignments are large enough to accommodate any misalignments created during machining. The coupling has a maximum torque rating of 42 in.-lb., which is more than the torque needed to drive the trolley, since only a 30 in.-lb. drive motor is used.

4.5 Trolley Body and U-Plate Analysis

The trolley body is the component that carries the load of almost every component on the trolley, which can be up to 50 lb. It experiences an upward force at each support arm and a downward force from the mounted device (see figure 4.18). The trolley body must also support the 50 lb. applied downward load from the linear actuators when they are activated to constrain the trolley.

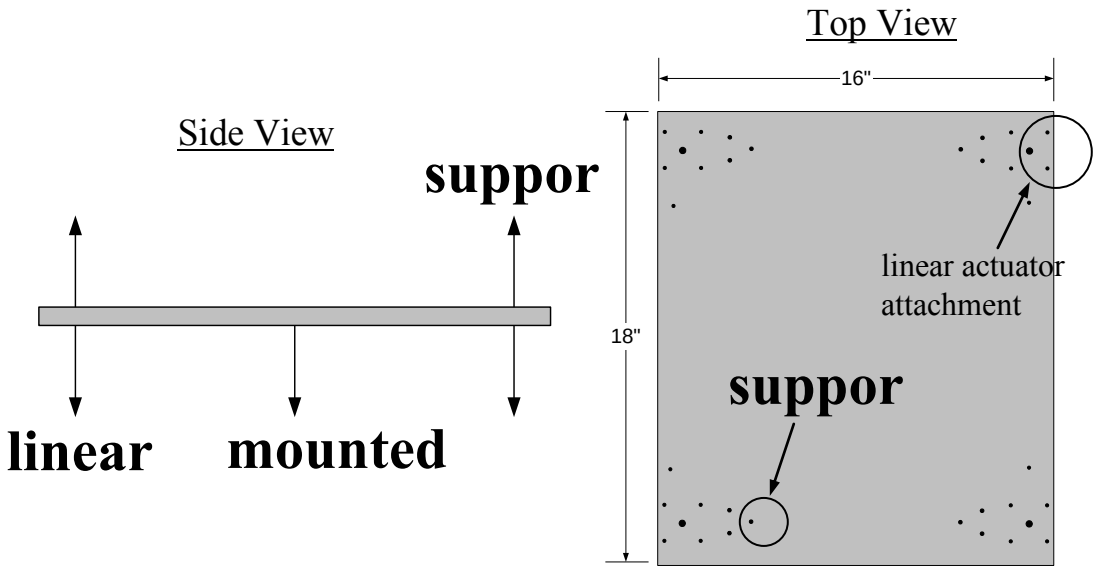

Figure 4.18: Trolley Body Loading Description

In addition to these forces, the trolley body supports the weight of all the components attached to it. Because of the multiple forces, a finite element analysis (FEA) was performed to determine the deflections and stresses applied to the trolley body using MSC PATRAN. The figures below show the results of the FE analysis.

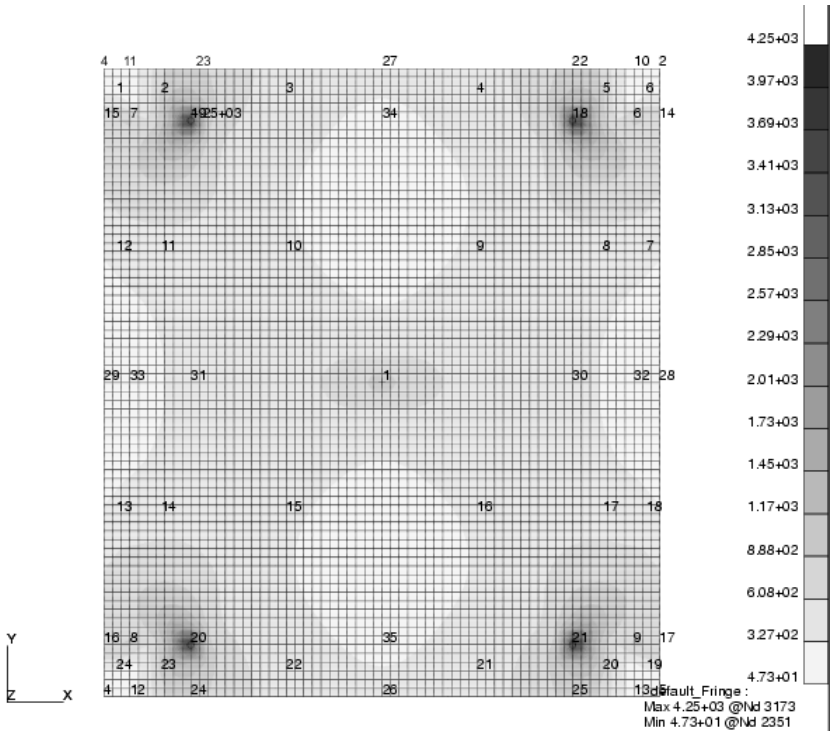

Figure 4.19: Stress on Trolley Body Due to Loading and Constraints

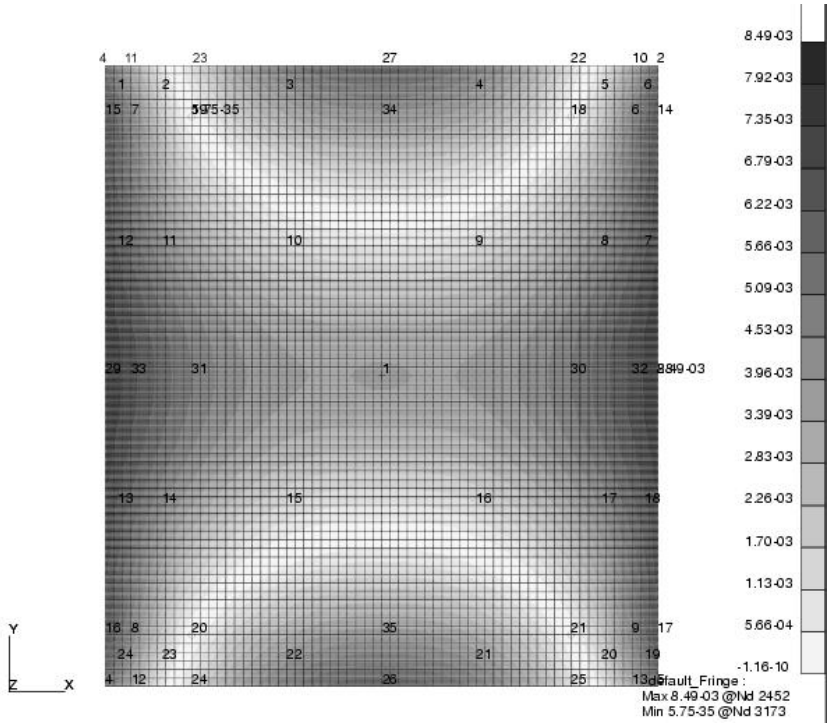

Figure 4.20a: Top View of Trolley Body Displacement Due to Loading and Constraints

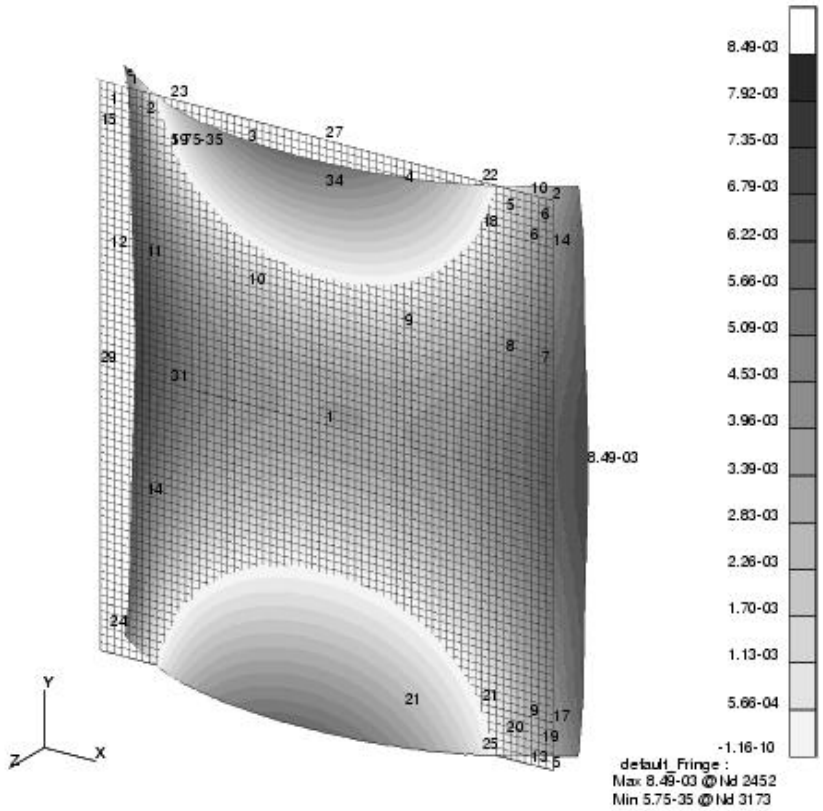

Figure 4.20b: Deformed View of Trolley Body Displacement Due to Loading and Constraints

The figures show the results of a 50 lb. load due to the trolley components and the mounted device as well as a 50 lb. load from each linear actuator being applied to the trolley body. Figure 4.19 depicts that the trolley body experiences a maximum stress of σ = 4250 psi at the four trolley support arm attachment points (near the corners). The yield strength of the trolley body is approximately 20 x 10^3 psi, which gives a factor of safety of $\eta = \frac{S_y}{\sigma} = \frac{20{,}000\ psi}{4250\ psi} = 4.7$. This maximum point of stress was not surprising because the support arms carry the entire weight of the trolley and mounted device. Figures 4.20a and 4.20b illustrate that the trolley body undergoes a maximum displacement of y_{max} = 0.0085 in. at the center of the outer edge of the trolley body. The minimum displacement occurs at the four support arms. These displacements were expected, since the center of the trolley has the least support. The analysis performed proves that the trolley body is strong enough to support the loads that it will experience.

The universal mounting plate (U-plate) is a component similar to the trolley body. The U-plate, however, only supports the weight of the mounted device, which is approximately 30 lb. for the laser detector. For this reason the stress on the U-plate will be less than that on the trolley body, and can therefore be made with slightly smaller thickness aluminum. The U-plate experiences an upward force from the trolley body connection points near the four corners, and a downward force from the mounted device connection points. For the laser detector, the device connection points will be six inches apart near the outside center as seen below:

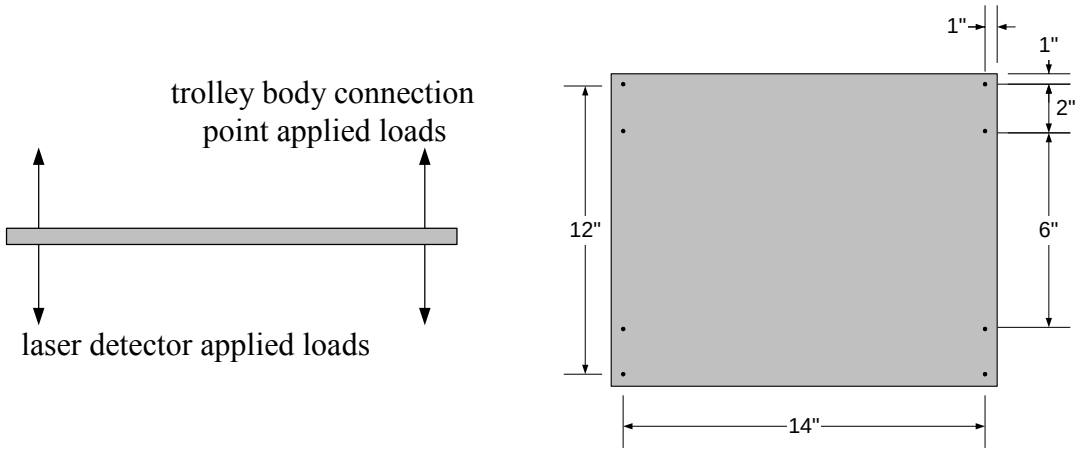

Figure 4.21: U-Plate Loading Description

To determine the state of stress of the U-plate due to the applied load from the laser detector, an FE analysis was performed. The FE analysis results are seen in the figures below:

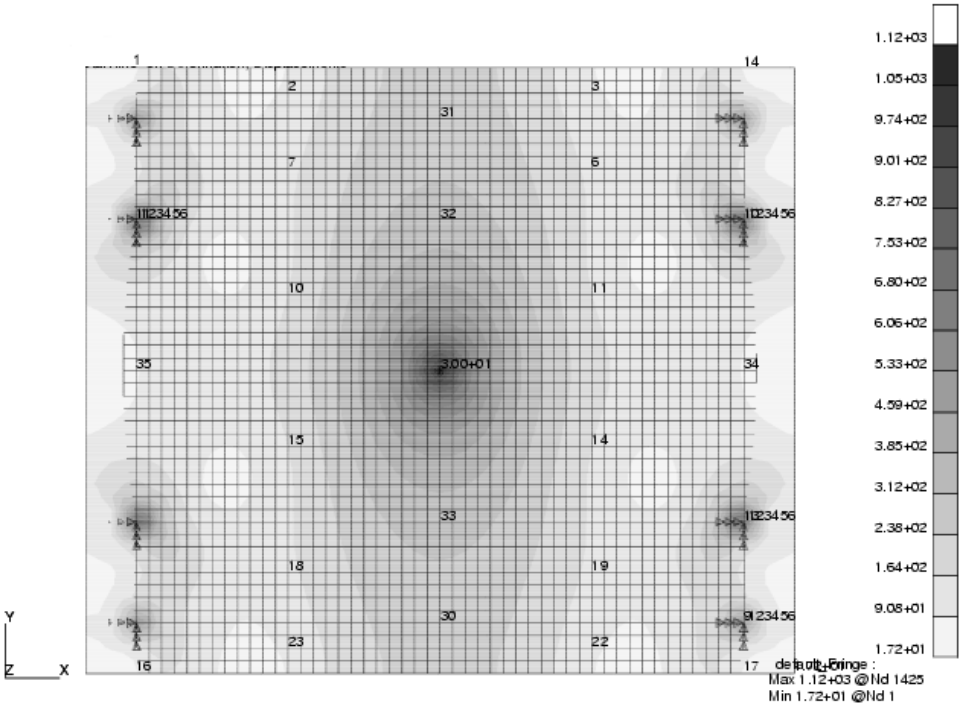

Figure 4.22: Stress on U-Plate Due to 30 lb. Laser Detector

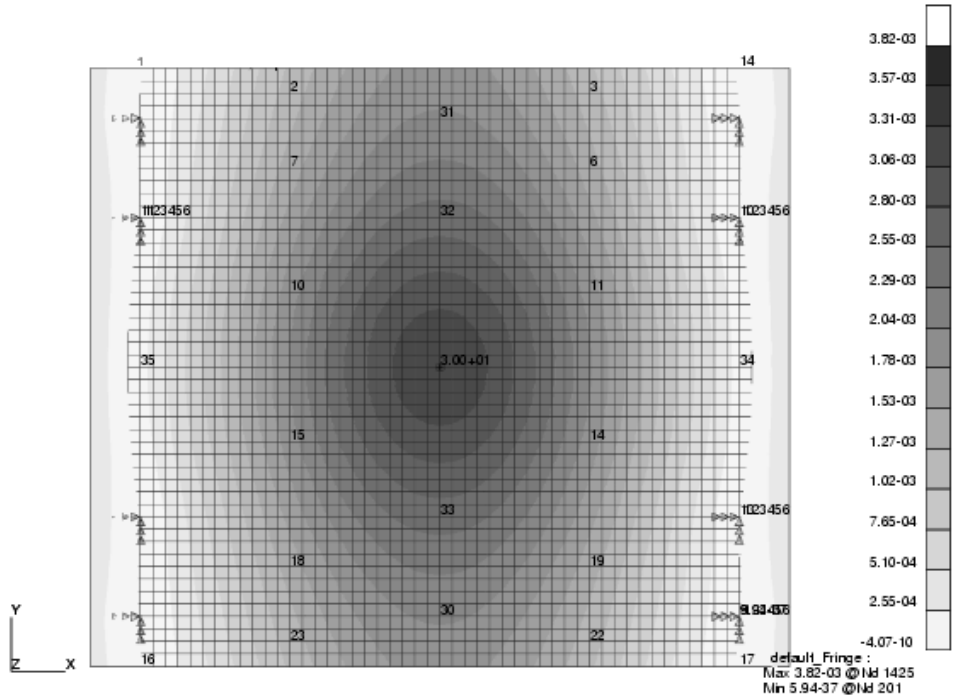

Figure 4.23a: Top View of U-plate Displacement Due to 30 lb. Laser Detector

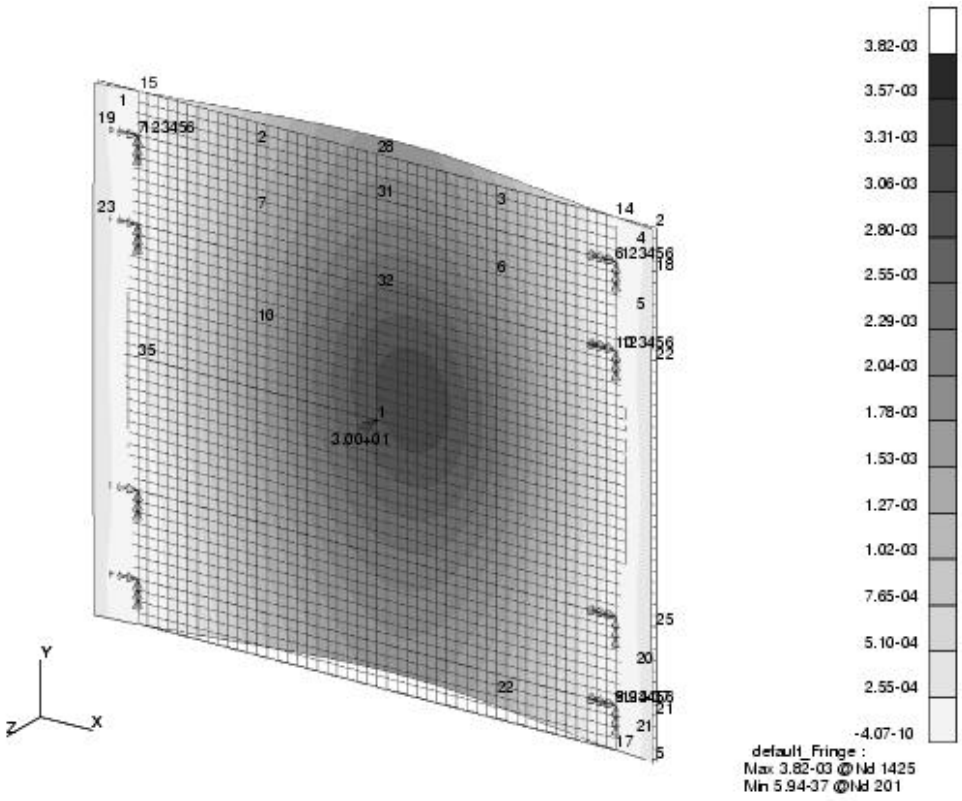

Figure 4.23b: Deformed View of U-plate Displacement Due to 30 lb. Laser Detector

These figures show the stresses and displacements that the U-plate experiences due to the weight of the laser detector. Figure 4.22 illustrates that the maximum stress on the U-plate is σ = 1120 psi at the center of the U-plate. The maximum stress was anticipated to be at the trolley body connection points, but this was not so. The maximum stress likely occurred at the center of the U-plate because it is least supported at that point. With this load, the factor of safety was calculated to be $\eta = \frac{S_y}{\sigma} = \frac{20{,}000\ psi}{1120\ psi} = 17.8$. Figures 4.23a and 4.23b demonstrate that the trolley experiences a maximum displacement of y_{max} = 0.00382 in. at the center of the U-plate. The minimum deflection was found to be at the trolley body connection points. These results were again expected because the U-plate is rigidly supported at the four corners, which allows for small deflections at the corners and larger deflections near the center. The analysis performed on the U-plate proves that it is more than capable of supporting any device that will be mounted to the trolley.

4.6 Track Analysis

An analysis was performed on the trolley system's tracks because they are the only elements holding the entire trolley system above ground. The tracks are connected to the sign truss via I-beams at a minimum of every 5.5 feet. This gives the tracks a considerable amount of support. In order to do the analysis for the tracks, two different approaches were used. One method was to model a section of track as a hole, and the other was to model only the weight-bearing flange of the aluminum channel. Both methods were needed for a thorough analysis of the tracks. Furthermore, for simplicity, the analysis was only performed on one of the two tracks using half of the trolley's 50 lb. load. To simplify the analysis further, the trolley weight was only modeled as a point load on the track, instead of the two points (one for each wheel) actually on the track. This was done because there would not be any significant differences in the results by using two point loads.

The model of the entire track section was used to determine the strength of the individual sections on which the trolley may rest. This model used the assumption that the trolley load was applied to the top of the aluminum channel. This will allow a determination of the stress and deflection that the entire section of track undergoes with the trolley mounted. For this analysis, only the worst-case position for the trolley was used, being at the center of the track. This was done because for any other trolley position, the tracks would not undergo as large a stress or deflection. The figures below show the loading condition and free body diagram for the entire track section model. First, a stress analysis was performed on the tracks using the equations below (all track calculations were made using MATLAB, see Appendix C).

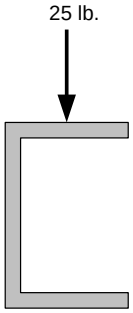

Figure 4.24a: Cross-Section

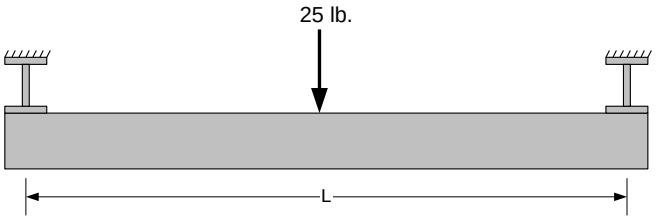

Figure 4.24b

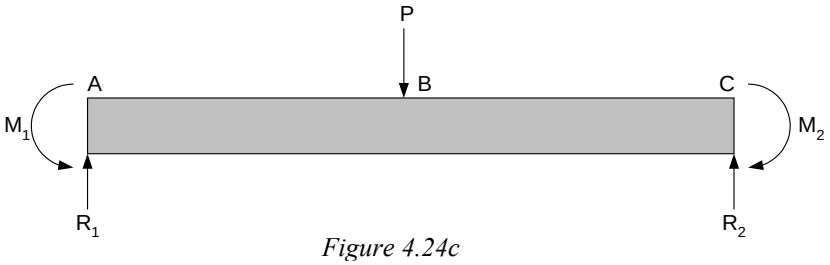

Figure 4.24c

$$M_1 = M_2 = -\frac{PL}{8}$$

$$M_{AB} = \frac{P}{8}(4x - L)$$

$$M_{BC} = \frac{P}{8}(3L - 4x)$$

$$R_1 = R_2 = \frac{P}{2}$$

Here, M_1 and M_2 are the bending moments at the supported ends of the track; M_{AB} and M_{BC} are the bending moments at a point, x, on the track between points A and B, and between points B and C, respectively; R_1 and R_2 are the reaction forces at the supported ends of the track. From the stress analysis, the maximum moment was found to be at the ends of the beam with a value of $M = M_1 = M_2 = 206$ in.-lb. The reaction forces at the ends were found to be $R_1 = R_2 = 12.5$ lb. The figures below show the shear and moment diagrams for this model.

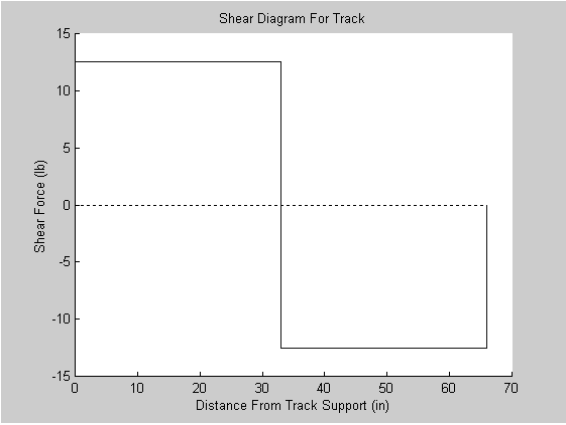

Figure 4.25: Track Shear Diagram

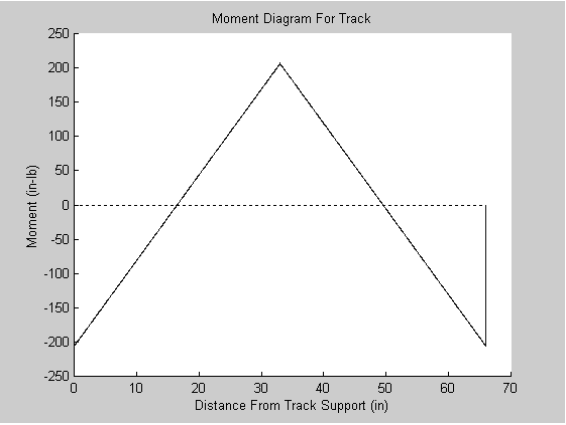

Figure 4.26: Track Moment Diagram

Following the stress analysis, calculations were performed to find the deflection characteristics of the tracks. The vertical displacement analysis for the tracks using the entire track section method involved more than just a simple beam analysis. Since the tracks are made of channel aluminum, the cross-section geometry had to be taken into account. First the area of the cross-section was determined. This was done by separating the C-channel shaped cross-section into three rectangles.

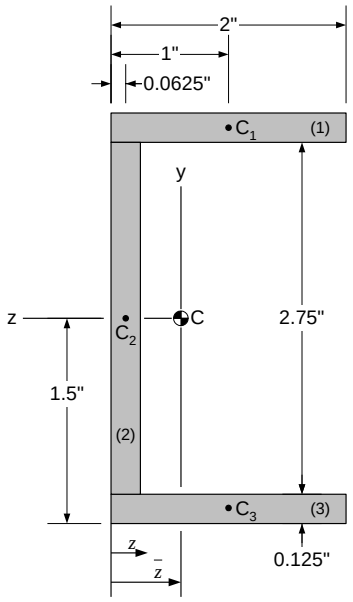

Figure 4.27: Track Cross-Section

Separating the cross-section into three rectangles facilitated the analysis. The areas of the cross-section were found in the following manner:

$$A = A_1 + A_2 + A_3 = (2")(0.125") + (2.75")(0.125") + (2")(0.125")$$

$$\underline{A = 0.8438\ in.^2}$$

With the total cross-section area determined, the next step is to find the location of the centroid. To do this, an arbitrary origin at the left (web) side of the cross-section is used and the coordinate in the *z*-direction is called *z*. Then, the first moment of area contributions are summed to give the total first area moment as follows (Ref. 11):

$$\int_A z\ dA = \int_{A_1} z\ dA + \int_{A_2} z\ dA + \int_{A_3} z\ dA$$

or

$$\bar{z}A = \bar{z}_1 A_1 + \bar{z}_2 A_2 + \bar{z}_3 A_3 = (1")(0.25") + (0.0625")(0.3438") + (1")(0.25")$$

$$\underline{\bar{z}A = 0.5215\ in.^3}$$

Then, to find the location of the centroid in the *x*-direction:

$$\bar{z} = \frac{\bar{z}A}{A} = \frac{0.5215\ in.^3}{0.8438\ in.^2} \quad \Rightarrow \quad \underline{\underline{\bar{z} = 0.6181\ in.}}$$

The location of the centroid in the *y*-direction is known due to the symmetry of the cross-section and has a value of $\bar{y} = 1.5"$ from the bottom of the cross-section. Now that the location of the centroid is known, the moment of inertia in the *z*- and *y*-directions can be determined. In order to determine the moments of inertia, the parallel-axis theorem must be used. The moment of inertia of a rectangle about an axis through its own centroid is:

$$I_C = \frac{1}{12} bh^3$$

Using this equation, the moments of inertia for each rectangle of the cross-section can be found as follows:

$$I_1 = \frac{1}{12}(2")(0.125")^3 \quad \Rightarrow \quad \underline{I_1 = 3.26 \text{ x } 10^{-4}\ in.^4}$$

$$I_2 = \frac{1}{12}(0.125")(2.75")^3 \quad \Rightarrow \quad \underline{I_2 = 0.217\ in.^4}$$

$$I_3 = \frac{1}{12}(2")(0.125")^3 \quad \Rightarrow \quad \underline{I_3 = 3.26 \text{ x } 10^{-4}\ in.^4}$$

By applying the parallel-axis theorem, the moment of inertia about an axis through the centroid of the composite cross-section can be determined. For the loading condition of the tracks, only the moment of inertia in the *z*-direction is needed. Therefore, the moment of inertia of the cross-section in the *z*-direction is:

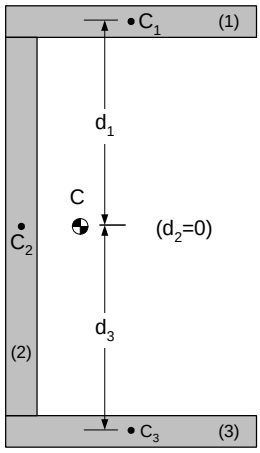

Figure 4.28: Track Cross-Section

$$I_z = (I_1 + A_1 d_1^2) + (I_2 + A_2 d_2^2) + (I_3 + A_3 d_3^2)$$
$$= \left[\frac{1}{12}(2")(0.125")^3 + (2")(0.125")(1.4375)^2\right] + \left[\frac{1}{12}(0.125")(2.75")^3\right]$$
$$+ \left[\frac{1}{12}(2")(0.125")^3 + (2")(0.125")(1.4375)^2\right]$$
$$\underline{\underline{I_z = I = 1.25\ in.^4}}$$

Now that the moment of inertia has been determined, the vertical displacement of the track can be calculated. This was done using the following equations:

$$y_{AB} = \frac{Px^2}{48EI}(4x - 3L)$$
$$y_{BC} = \frac{P(L-x)^2}{48EI}(4(L-x) - 3L)$$
$$y_{max} = -\frac{PL^3}{192EI}$$

where, y_{AB} and y_{BC} are the vertical displacements at a point, x, along the track between points A and B, and between points B and C, respectively. From these equations the maximum track deflection was found to be y_{max} = 0.0029 in. and a plot of the track deflection between the track supports was created as seen in the figure below.

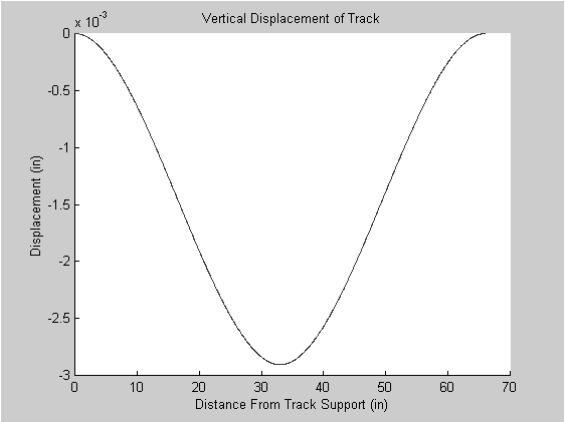

Figure 4.29: Track Deflection Plot

After determining the deflection characteristics of the track, the maximum bending stress and factor of safety were calculated. The maximum bending stress is found in the following manner:

$$\sigma_{max_x} = \frac{-My}{I} = \frac{-(206\ in.-lb.)(-1.5\ in.)}{1.25\ in.^4} \quad \Rightarrow \quad \underline{\underline{\sigma_{max_x} = 248.2\ psi}}$$

To determine the factor of safety, the yield stress of the metal is compared to the maximum bending stress as follows:

$$\eta = \frac{S_y}{\sigma_{max}} = \frac{20{,}000\ psi}{248.2\ psi} \quad \Rightarrow \quad \underline{\underline{\eta = 80.5}}$$

This shows that the tracks are extremely strong and can easily withhold the weight of the trolley and mounted device.

Next, a method to better analyze the flange reaction was performed using the partial differential equations toolbox in MATLAB (see Appendix C). This method modeled a load being applied to the bottom flange of the tracks, on which the trolley wheels sit, instead of to the entire track. In doing this method, the track cross-section strength and deflection can be analyzed and determined. This analysis gives a more detailed look at how the track reacts to the mounted trolley. The figures below show the result of the analysis:

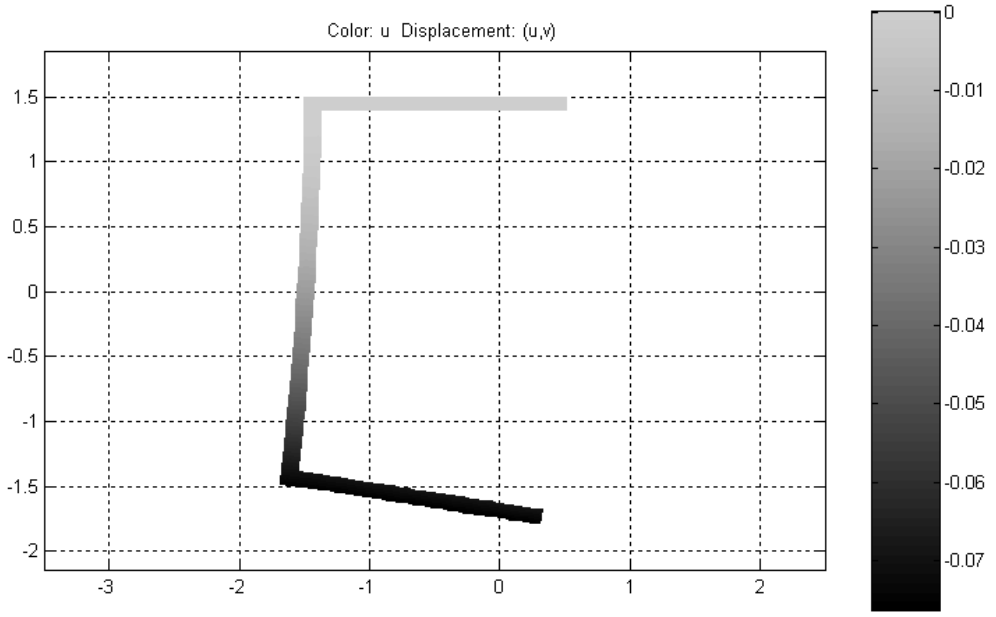

Figure 4.30a: Deformed Track with x-Displacement of Track Color Code

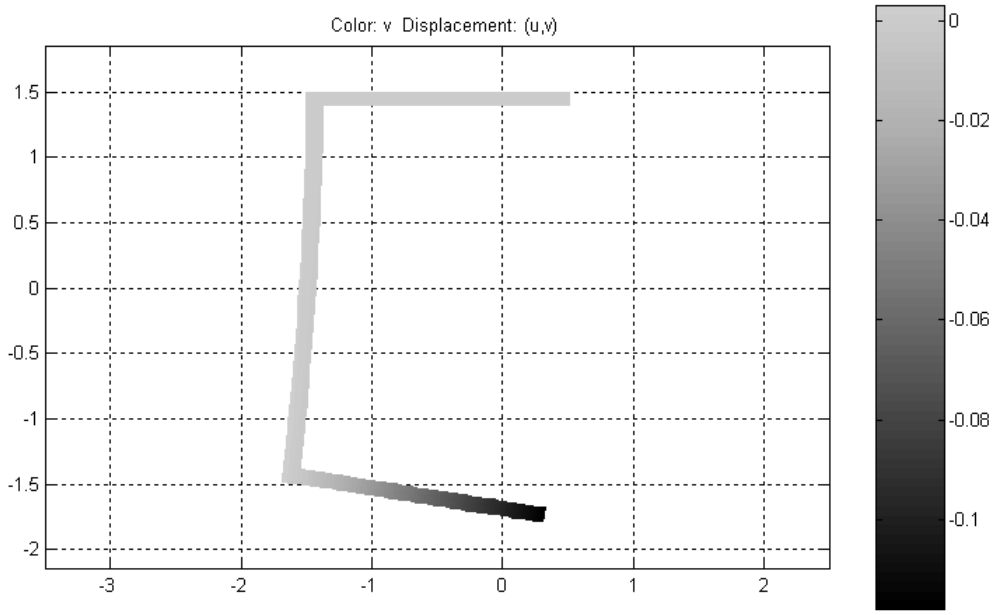

Figure 4.30b: Deformed Track with y-Displacement of Track Color Code

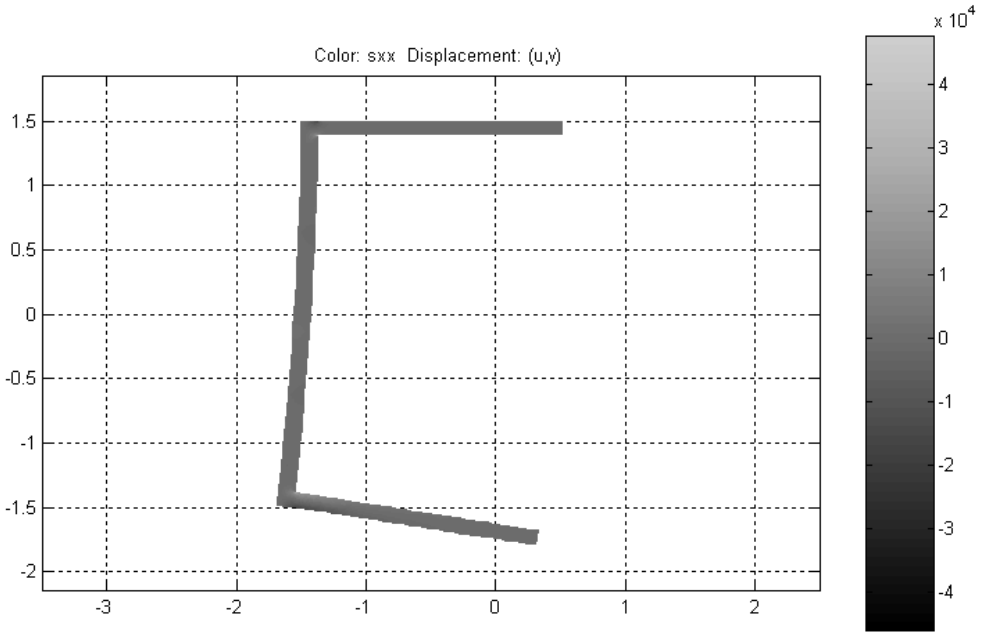

Figure 4.30c: Deformed Track with x-Stress of Track Color Code

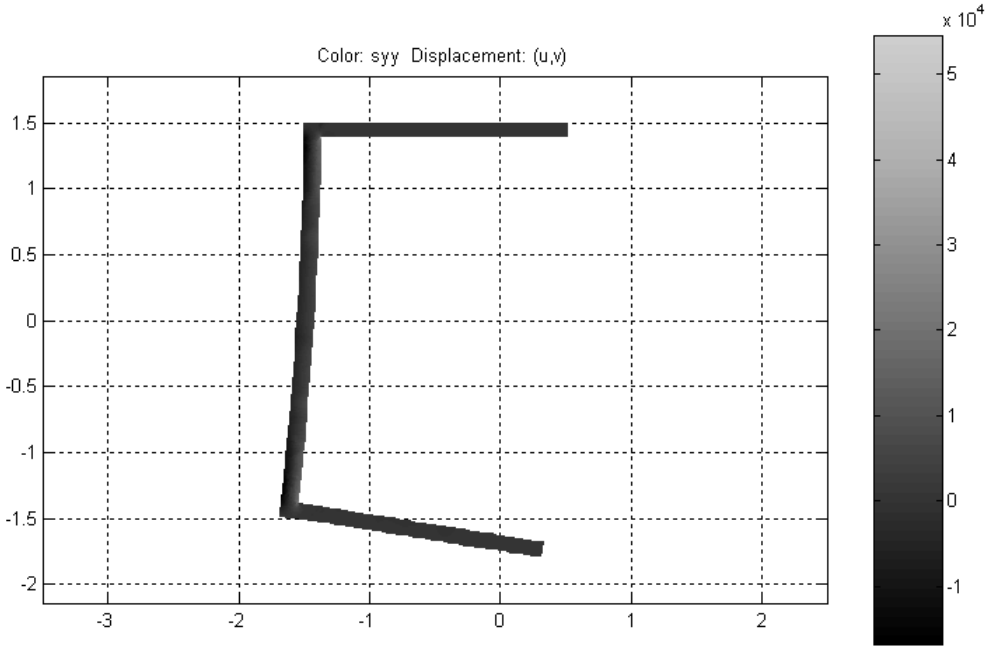

Figure 4.30d: Deformed Track with y-Stress of Track Color Code

These figures all show a physical representation of how the track will deform with the trolley system mounted to it. This is obviously an exaggerated deformation but is used to

help visualize the displacements since they are so small. The color-coding on figures 4.30a and 4.30b shows the *x*- and *y*-displacements, respectively, of the track. The color-coding is helpful to see how large the displacements are on all parts of the track. It is seen that the largest *y*-displacement is at the end of the bottom flange of the track, as expected, and has an approximate value of 0.12 inches. It is also noticed that the largest *x*-displacement is experienced on the entire bottom flange with an approximate value of 0.075 inches. These displacements are relatively small and prove that the tracks can support the trolley without excessive deformation.

Figures 4.30c and 4.30d illustrate the *x*- and *y*-stresses on the track. It is noticed that the largest stresses are found at the top and bottom inside corners of the track. Although is it seen that the bottom inside corner of the *x*-stress experiences the largest stress distribution, the top inside corner actually experiences the largest stress. For the *y*-stress, the stress is more evenly distributed between the top and bottom corners, but the top inner corner again experiences the largest stress. The maximum stresses were found to be approximately $\sigma_y = 5.5 \times 10^4$ psi and $\sigma_x = 4.8 \times 10^4$ psi. These values are very large and demonstrate that the tracks will suffer very small fractures at the inside corners. Although the values are very large at the corners, it is only an extremely small area that experiences this large stress. The average stress through the track cross-section is $\sigma_y = \sigma_x = 5000$ psi demonstrating that the tracks will not fracture. The MATLAB program most likely calculated very small micro-stresses at the corners and applied them to the analysis. This may be an error in MATLAB. The tracks will be tested to prove their strength and durability.

After the tracks were thoroughly analyzed for static loading, the dynamic loading due to an applied wind force was explored. The trolley is mounted between the tracks and its center of gravity is nearly at the center of the tracks. This gives a 7.25" moment arm for twisting of the tracks as seen in figure 4.31. From the environmental analysis in chapter 6 it was found that with the wind hitting the frontal face of the laser detector, a force of 5.4 lb. will be applied to each linear actuator. This creates a 10.8 lb. force per track, which applies a 135 in.-lb. torque to the tracks. However, since the axis of rotation for

the tracks is between them and not through their individual centers of gravity, the tracks can be assumed to only experience a bending force. The tracks may experience a small torque, but its effect will be small compared to that of the bending force and thus can be neglected.

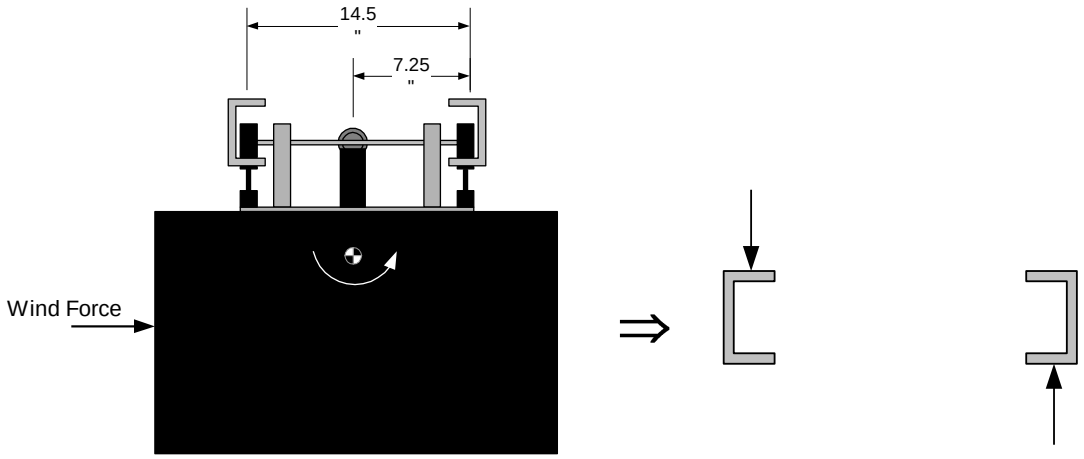

Figure 4.31: Applied Force on Tracks

4.7 Trolley Support Arm and Wheel Analysis

The support arms for the trolley were chosen to be made of aluminum instead of a plastic for environmental and durability reasons. Other materials were not considered. Because they had to be effectively connected to the trolley body and needed to have bearings inset in them, the support arms were chosen to be a solid block of aluminum. This makes them very strong, and since they will mainly only be exposed to a tensile load, they will easily withstand the necessary loads of the trolley system.

The limitation of the support arms will be their connection to the trolley body. Each support arm is connected to the trolley body using three stainless steel 8-32 x 3/4" long screws. These screws were found to have a holding force of 385 lb. each, from table 8-13 in *Mechanical Engineering Design, 5th ed.* (Ref. 8). This gives each support arm a total of 1155 lb. of tensile holding force from the screws. The total holding force from all four support arms is 4620 lb. This is far more load than the trolley will ever experience. Any

shear loads on the support arms will be negligible due to the aid of the linear actuators in constraining the trolley while positioned over traffic.

The wheels were chosen solely for their friction, environmental stability, and holding strength. First, the wheels need to have a high coefficient of friction with the aluminum tracks. Along with this, the wheels need to be able to withstand all of the environmental conditions that they may encounter. For these reasons, the wheels were chosen to be made of neoprene. After choosing the material, the next step was to choose the neoprene properties. In order to be environmentally stable, the neoprene was chosen to have a durometer measurement of 90. This durometer measurement is slightly larger than that for a car tire, so it will be at least as environmentally stable as any vehicle tire on the road. Next, the finish of the wheels were chosen to be roughened and without tread. Tread was not needed because the tracks are smooth and the roughened surface will allow a larger contact area, giving better traction.

Finally, the wheels need to be strong enough to hold the dynamic and static loads that the trolley will impose on them. For this reason, the wheels were given a 1.25" diameter aluminum hub and 0.375" thick solid neoprene wheel surrounding it. This created a 2" diameter solid composite wheel. The aluminum hub and solid neoprene wheel gives the wheels a large holding strength. Each wheel is capable of holding 200 lb. giving the entire trolley an 800 lb. wheel load capacity. This is far more load than the trolley system will ever experience.

4.8 Motor and Linear Actuator Analysis

In determining the motor torque needed to drive the trolley system, an analysis was performed on the system with the laser detector mounted. To begin with, the motor needs to be able to overcome the rolling friction of the weighty system. This was determined by finding the rolling friction, and then the rolling resistance. The rolling

resistance is the applied resistance torque that the rolling friction will impose on the trolley wheels. (Ref. 12)

$$\square\ motor\ torque = 30\ in.-lb.$$

$$\square\ \mu_r \cong 0.015\ (coefficient\ of\ rolling\ friction)$$

$$f_r = \mu_r N = (0.015)(50\ lb.) \ \Rightarrow\ \underline{f_r = 0.75\ lbf}$$

$$Rolling\ Resistance:$$

$$R_r = rf_r = (1\ in.)(0.75\ lbf) \ \Rightarrow\ \underline{\underline{R_r = 0.75\ in.-lb.}}$$

This rolling resistance is noticed to be very small compared to the motor torque and can therefore be neglected.

Next, the external resistance forces on the trolley needed to be taken into account. The primary, and most appreciable, external force on the trolley will be due to the wind. It was found that the largest drag force on the system would be in the direction of motion of the trolley (i.e. parallel with the tracks) directly opposing (or adding to) the trolleys motion. The case for an opposing wind force of 40 mph will be considered to help determine the motor torque needed. For a 40 mph wind, the drag force on the laser detector was found to be 15 lb. (see Chapter 6). This means that the motor will need a torque of 15 in.-lb. as seen below:

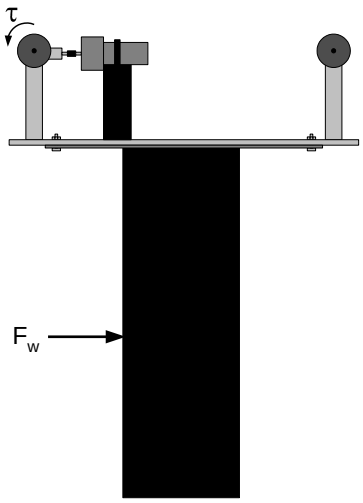

Figure 4.32: Wind Force and Torque Directions

$$\tau = F_w r = (15\ lb.)(1\ in.) \ \Rightarrow\ \underline{\tau = 15\ in.-lb.}$$

The motor chosen for the trolley has 30 in.-lb. of torque. This motor was chosen because of its small size and weight, yet rather high torque. The motor is observed to have enough torque to overcome a 40 mph direct lateral wind. In fact, since the wheel radius is one inch, the above equation can be used to show that the motor will be able to withstand opposing forces up to 30 lb. The next step is to determine if the trolley wheels will have enough friction to withstand a 30 lb. force. Below the static and kinetic friction forces are calculated:

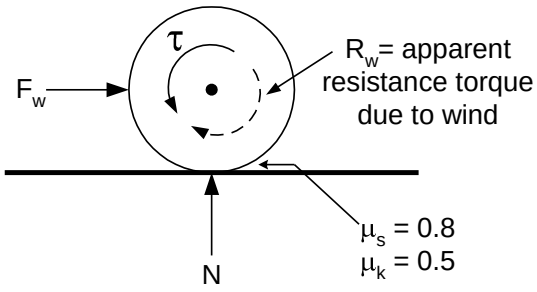

Figure 4.33: Wheel Friction Forces

$$f_s = N\mu_s = (50\ lb.)(0.8) \quad \Rightarrow \quad \underline{f_s = 40\ lb.}$$

$$f_k = N\mu_k = (50\ lb.)(0.5) \quad \Rightarrow \quad \underline{f_k = 25\ lb.}$$

The above equations show that the trolley wheels will have enough friction to overcome an external force of 40 lb. when starting from rest, but only 25 lb. while moving. This illustrates that the maximum external force that the trolley can withstand is 25 lb, which corresponds to a direct lateral wind speed of about 52 mph.

To ensure that the trolley will be able to operate properly, it should not be driven when wind speeds exceed 40 mph. This is due to the limitation of the wheels. The wheels can only withstand a maximum of 52 mph direct lateral wind (or 25 lb. external force) before slipping. It may be possible to use wheels with a slightly higher coefficient of dynamic friction, but for the application requirements, there would not be a significant difference. Therefore, an operating condition is imposed on the trolley system of not driving the

trolley when wind speeds exceed 40 mph. This is a very reasonable operating constraint and will likely not be a hindrance very often.

As for the linear actuators, they were chosen as a result of the necessary holding force and size constraints. It was found that a lateral wind load on the laser detector would cause the most appreciable forces on the trolley system. The trolley system has been designed to withstand 90 mph winds while in position over traffic. In order to maintain this constraint, the linear actuators would need to withstand the applied forces from the wind. These forces were found to be as large as 23 lb. on a single linear actuator (see Chapter 6).

At first, the idea was to use solenoids as the static constraints for the trolley. The solenoids would retract strong springs when powered, and when de-powered the springs would extend to the tracks being the only holding force. For a 23 lb. force, solenoids were not a practical option. Therefore, it was decided to use a screw driven type linear actuator. This type of linear actuator uses a permanent magnet motor to drive a worm gear. After much research, a linear actuator was found that had 50 lb. of holding force. It is small in size and

CHAPTER 5

VIBRATION ANALYSIS

5.1 Trolley Vibrations

The trolley system can experience vibrations from many different sources, however the primary source is from wind loads imposed by the environment and passing vehicles. Strong, steady winds hitting the trolley system may create harmonic vibrations, but for the most part the wind loads applied to the trolley will occur as impact loads, or shock pulses. This means that the wind will impact the trolley for only a brief period of time. Passing vehicles are the most common cause of wind gusts hitting the trolley; strong and steady winds only occur occasionally. When the trolley is moving, vibrations will not harm the system, since the mounted device will not be collecting data. The mounted device will collect data only when the trolley is in position over traffic and locked in place. Vibrations in this mounted position can adversely affect collected data. (The analysis in this chapter uses methods and equations from *Engineering Vibration*, Ref. 13)

Since only vibrations in the stationary mounted position can cause a disturbance, the trolley wheels can act as vibration isolators for the system. When a wind gust hits the trolley system, a shock pulse will be experienced. This shock will cause the trolley and mounted laser detector to vibrate momentarily. Since the trolley is held firmly to the tracks via the static constraint system, and the tracks are assumed to be rigid, the primary vibration of the system will be due to the deformation of the wheels (the trolley system with mounted device is assumed to be a single rigid body). By using a wheel material that has the appropriate properties, the wheels can act as vibration isolators to minimize the vibration that the trolley system experiences.

To find the best material to use for the trolley wheels, the harmonic vibration due to steady wind and the systems response to wind generated shock pulses will be analyzed. For the shock pulse vibration, an analysis using a bond graph was performed. A bond graph was used because it can easily model certain complexities introduced by the limited displacement allowed by the static constraint system. Figure 5.1 shows the wheel area of the trolley system and its simplified model.

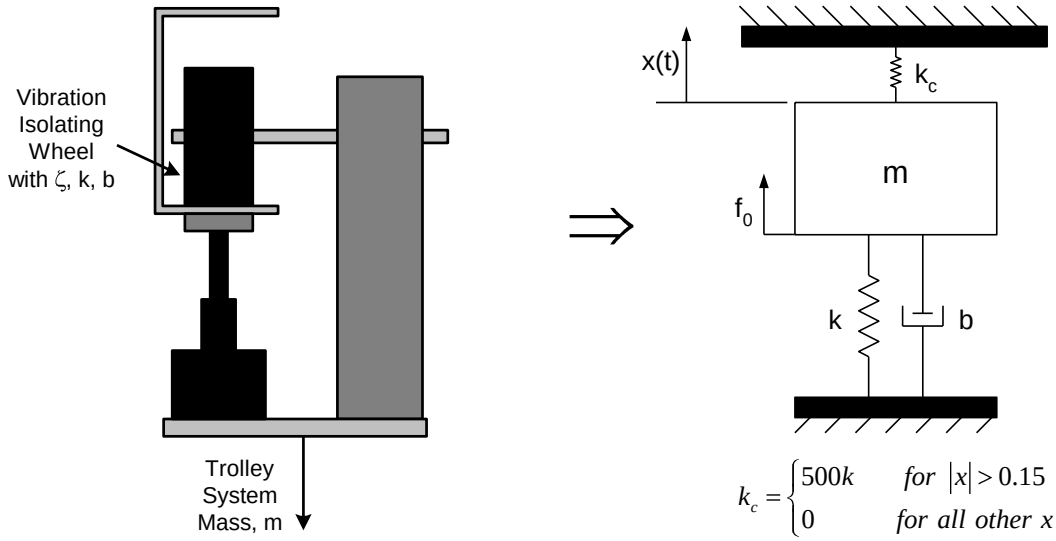

Figure 5.1: Trolley Vibration Model for Shock Pulse

This models the trolley wheel as a spring and dashpot, with stiffness k and damping constant b, mounted to a fixed track. The tracks are assumed to be fixed because they are rigidly attached to the sturdy truss. To model the displacement limits imposed by the static constraint system, a nonlinear spring was used seen in figure 5.1 and modeled on bond number 3 in figure 5.2. This nonlinear spring was designed such that if the displacement of the wheel were larger than ±0.15 in., the spring would have a stiffness value of $k_c = 500k$, otherwise $k_c = 0$. For a shock pulse, a vibration analysis is performed to determine the stiffness that will minimize the trolley's vibration response. To this end,

the time response of the trolley when it is subject to a shock pulse was generated through the use of the system's bond graph shown in figure 5.2.

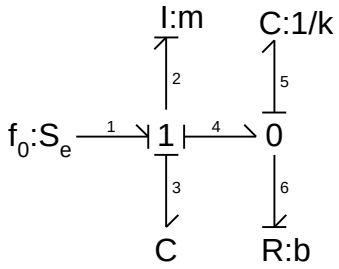

Figure 5.2: Bond Graph of Trolley Shock Vibration Model

This bond graph yields the following state equations:

$$\dot{p} = f_0 - k_c x - kq$$

$$\dot{q} = \frac{p}{m} - \frac{kq}{b}$$

$$\dot{x} = \frac{p}{m}$$

where, q is the displacement across the spring, p is the mass (wheel) momentum, x is the mass (wheel) displacement, and f_0 is the input force. (Ref. 14)

Since the trolley is locked in place by the static constraint system, the amplitude of the trolley displacement will be constrained by the amount of deformation of the wheels. The maximum deformation that the wheels can undergo is approximately 0.3 inches. This means that the maximum amplitude of vibration is only 0.15 inches. This constraint will aid in minimizing the vibration that the trolley experiences. This vibration-reducing phenomenon can be seen in figures 5.3a and 5.3b. Both figures simulate the same system, with one having unconstrained vibration and the other having constrained vibration. The unconstrained vibration is the vibration response of the trolley without the linear actuators employed, and the constrained vibration is the vibration response with the linear actuators employed.

Using the state equations with a damping ratio of $\zeta = 0.05$, the stiffness is the only variable (this value of damping ratio was chosen because rubber was the most foreseeable wheel material to be used, and $\zeta = 0.05$ is the value for natural rubber). System time responses were plotted for various values of wheel stiffness. In order to integrate the equations, initial values had to be input (all calculations were made using MATLAB, see Appendix C). The initial displacement was taken to be $x_0 = 0$ since the trolley was at rest. The system is designed to withstand 90 mph winds, which corresponds to a 75 lb force (see chapter 6), so the input force was assigned the value $f_0 = 75$ lb.

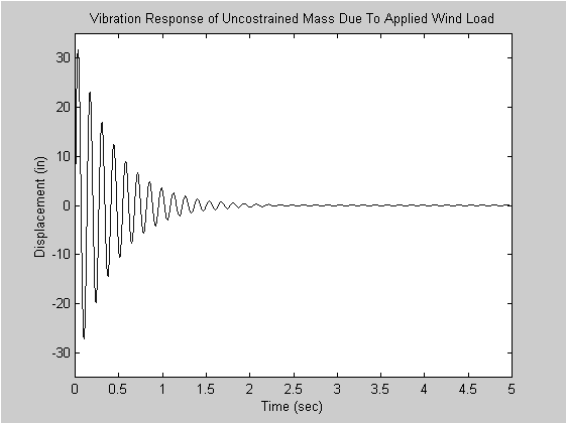

Figure 5.3a: Unconstrained Vibration Response

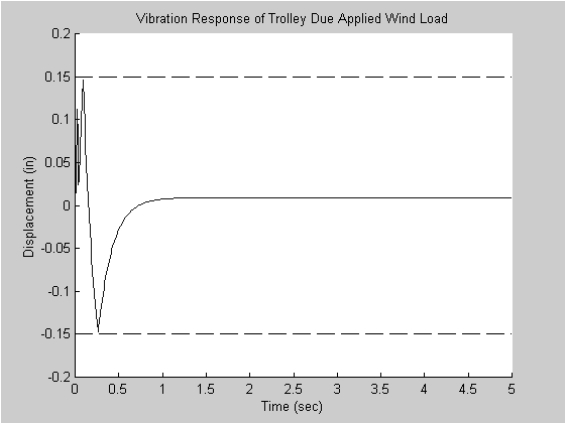

Figure 5.3b:Constrained Vibration Response

After plotting the vertical displacement of the trolley as a function of time, a trend was observed. For increasing values of stiffness, the vibration response improved as shown in figure 5.4. Therefore, to minimize the vibration of the trolley due to a shock pulse, the stiffness of the wheel material needs to be maximized. The minimum acceptable value of stiffness was decided to be that which caused vibration to cease after approximately one second. This decision created the need for the stiffness value to be greater than $k = 275 \frac{lb}{in}$ to minimize the trolley vibration due to a shock pulse.

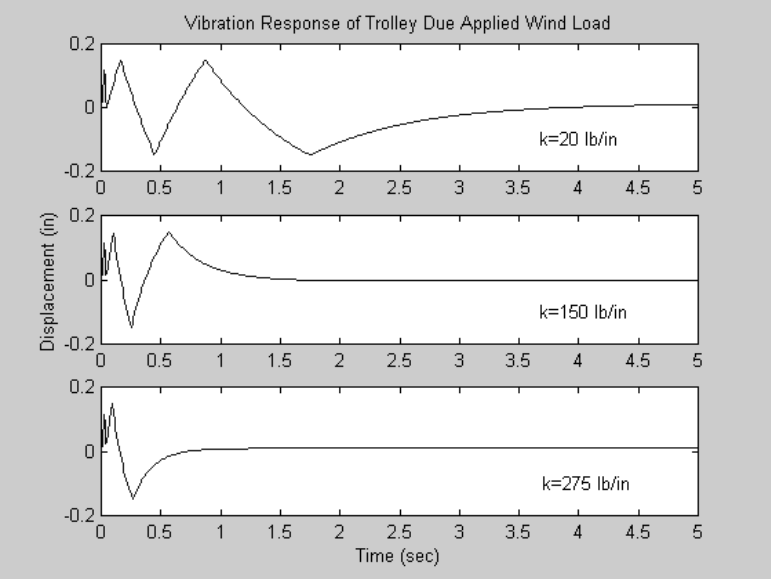

Figure 5.4: Vibration Response for Various Values of Stiffness

With the shock pulse vibration stiffness approximated, the next step is to determine how harmonic vibrations affect the trolley system. Using the model in figure 5.5 below, a vibration analysis can be performed to find the wheel stiffness that minimizes the trolley vibration response.

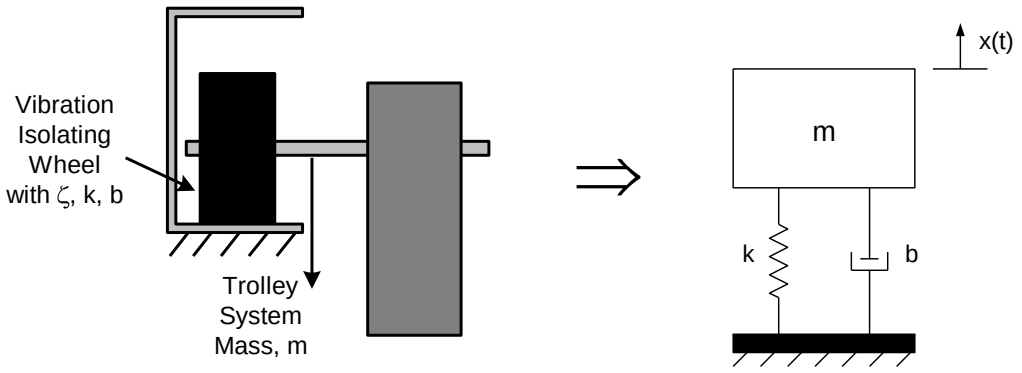

Figure 5.5: Trolley Vibration Model for Harmonic Vibrations

This model is similar to that of the shock pulse model except for the constraint system. The constraint system is not needed for modeling the harmonic vibration because it is assumed that it does not cause as large a displacement as a shock pulse does. For a harmonic vibration, a simple analysis can be performed to determine the wheel material stiffness that will minimize the trolley's vibration response. The equation of motion for

an underdamped system was used to create a time response of the trolley. Since the input is a harmonic motion, there must be a forcing function that excites the system. This forcing function is assumed to be:

$$F(t) = F_0 \cos(\omega_{dr} t)$$

The magnitude F_0 is determined by the force that the wind imposes on the wheels of the trolley. In chapter 6 it is noticed that the maximum force the wind can impose on each wheel of the trolley is 36 lb. Since this 36 lb. force is the maximum force imposed on a single wheel, the harmonic vibration force magnitude is given the value $F_0 = 36$ lb. The equation of motion for an underdamped harmonic that describes the system's vibration can be written as:

$$x(t) = Ae^{-\zeta\omega t} \sin(\omega_d t + \phi) + A_0 \cos(\omega_{dr} t - \theta)$$

with,

$$A = \sqrt{\frac{(v_0 + \zeta\omega x_0)^2 + (x_0\omega_d)^2}{\omega_d^2}} \qquad \phi = \tan^{-1}\left(\frac{x_0\omega_d}{v_0 + \zeta\omega x_0}\right)$$

where, $\omega_d = \omega\sqrt{1-\zeta^2}$

$$A_0 = \frac{f_0}{\sqrt{(\omega^2 - \omega_{dr}^2)^2 + (2\zeta\omega\omega_{dr})^2}} \qquad \theta = \tan^{-1}\left(\frac{2\zeta\omega\omega_{dr}}{\omega^2 - \omega_{dr}^2}\right)$$

and, $f_0 = \frac{F_0}{m}$

This equation takes into account the transient response from a shock pulse as well as the steady-state response from a harmonic input. Since the shock pulse has already been studied, the initial conditions will be set to zero to analyze only the harmonic response (the initial velocity is actually set to $v_0 = 0.0001 \frac{in}{sec}$ to avoid a divide by zero error in calculating ϕ, but still eliminate the transient effects).

Using a damping ratio of $\zeta = 0.05$, the time response of the trolley to the harmonic input depends on two variables, the stiffness k and the harmonic driving frequency ω_{dr}. Since the mass of the trolley is known, the variables can be put in terms of the natural frequency of the trolley, ω, and ω_{dr}. This allows a normalized magnitude plot to be generated, which can be used to illustrate the frequency interdependence. To create this

plot, the amplitude, A_0, was normalized and plotted against the frequency ratio as seen below:

$$\frac{A_0\omega^2}{f_0} = \frac{1}{\sqrt{(1-r^2)^2 + (2\zeta r)^2}}$$

$$\textit{where, } r \textit{ is the frequency ratio } r = \frac{\omega_{dr}}{\omega}$$

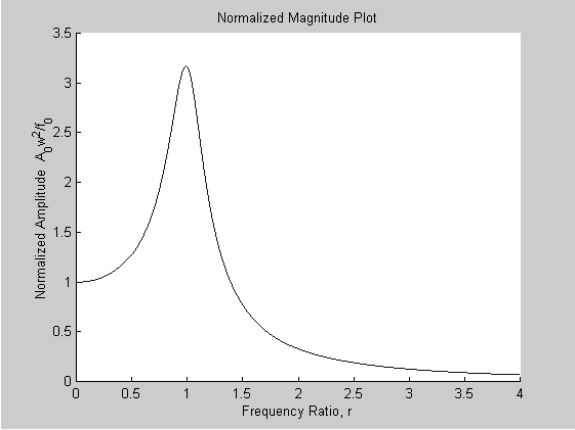

Figure 5.6: Normalized Magnitude Plot for a Harmonic Input

The normalized magnitude plot demonstrates that resonance will occur when the driving frequency and system natural frequency approach the same value. By using this plot, it was decided that by making the natural frequency at most half the value of the driving frequency, the vibration that the trolley experiences can be minimized. From this, the a limit can be put on the wheel stiffness value as follows:

$$\omega = \sqrt{\frac{k}{m}} < \frac{\omega_{dr}}{2} \quad \Rightarrow \quad k < \frac{m\omega_{dr}^2}{4}$$

$$\textit{with the mass as } m = 1.55 \textit{ slugs the stiffness becomes,}$$

$$k < \frac{\omega_{dr}^2 (1.55\ slugs)\ \frac{1\ in}{12\ ft}}{4} \quad \Rightarrow \quad \underline{\underline{k < 0.032\omega_{dr}^2}}$$

This shows that for an assumed driving frequency of ω_{dr} = 2 Hz = $12.56 \frac{rad}{s}$, the stiffness will need to be less than $5.1 \frac{lb}{in}$ in order to minimize the vibration due to harmonic vibration. For a driving frequency of ω_{dr} = 20 Hz = $125.7 \frac{rad}{s}$, the stiffness will need to

be $k < 510 \frac{lb}{in}$. This reveals that for very low frequency harmonic vibrations, the stiffness must be rather small. However, as the driving frequency begins to increase the stiffness increases dramatically. Due to the interdependence between the stiffness and driving frequency, a value of stiffness cannot be approximated. This is because the driving frequency is not known.

To help approximate a stiffness value for the trolley wheels that will reduce vibration from a harmonic input, the laser detector can be examined more closely. As mentioned earlier, the laser detector can be impaired by vibration. Of these disturbing vibrations, high frequency vibrations will be more disturbing than low frequency vibrations. The high frequency range can be defined as vibrations above 10 Hz. From this definition, an approximate stiffness of the trolley wheels can be assigned. For a 10 Hz driving frequency, the wheel stiffness needs to be $k < 127.5 \frac{lb}{in}$. This is only an approximate boundary for the wheel stiffness, and is subject to change for different mounted devices and different harmonic conditions. Figure 5.7 below depicts the steady-state time response of the trolley system to a harmonic input with a 10 Hz driving frequency and stiffness of $127.5 \frac{lb}{in}$. The figure shows that the trolley only vibrates with an amplitude of 0.088 inches, which proves that the initial assumption of neglecting the constraint system was legitimate.

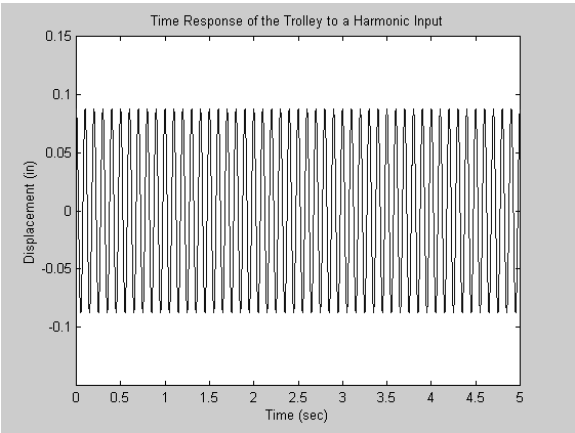

Figure 5.7: Steady-State Vibration Response of Trolley to Harmonic Input

The calculations performed show that the value of stiffness needed for trolley vibration isolation is $k > 275\frac{lb}{in}$ for shock pulses and $k < 127.5\frac{lb}{in}$ for harmonic vibrations. This gives a conflicting stiffness range of $275\frac{lb}{in} > k < 127.5\frac{lb}{in}$ for the trolley wheels. Due to the conflict in the stiffness value for the appropriate wheel material, the most appropriate range must be selected. Since the trolley will experience shock pulses more commonly than harmonic vibrations, the shock pulse stiffness range will be used. Therefore, wheel stiffness should have a value of $k > 275\frac{lb}{in}$.

5.2 Truss Vibrations

Vibrations experienced by the trolley will be primarily due to winds hitting the trolley system itself. However, vibrations transmitted to the trolley from the truss are also a possibility. The truss is built to withstand 90 mph winds making it extremely strong, but it is not built to prevent vibrations. Therefore, vibrations that the truss experiences may be passed on to the attached trolley system. The simple model of the truss and trolley shown in figure 5.8 is used to determine the effects of the truss motion.

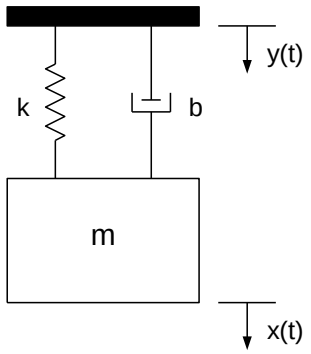

Figure 5.8: Truss and Trolley Vibration Model

The y(t) is a base excitation and x(t) is the output motion. The base excitation is the input to the system and represents the vibration of the truss. The truss input is assumed to be a sinusoidal input with a natural frequency of $\omega_b = 2$ Hz. The spring and dashpot in this

model represent the stiffness and damping of the trolley wheels. The output motion, x(t), represents the vibration of the trolley with natural frequency ω. The device that is mounted to the trolley is assumed to be rigidly attached. Therefore, the output motion may also represent the vibration of the device. The model depicts that input from the truss, y(t), must transmit vibration through the wheels with stiffness k and damping b in order to cause the trolley to vibrate. Because of this, the wheels are the primary factor in determining the vibration that the trolley experiences. With the appropriate material properties, the wheels can again act as vibration isolators to minimize the amount of vibration transmitted from the truss to the trolley system.

In order to determine the best material to use for the trolley wheels, the damping ratio will be assumed and the harmonic vibration and shock pulse stiffness values will be approximated. A problem exists in that for the case of base excitation, harmonic vibration isolation and shock isolation are accomplished via opposing methods. A harmonic vibration isolator requires a larger stiffness, whereas a shock isolator requires a smaller stiffness. This opposition means that a device which provides great isolation from harmonic vibration will not protect from shocks. It is noticed that the truss will undergo more vibration due to harmonic inputs than to shock pulses. For this reason, the trolley wheels will be made of a material that provides better harmonic vibration isolation than shock isolation.

To find the harmonic vibration stiffness, a displacement transmissibility plot can be used as seen below:

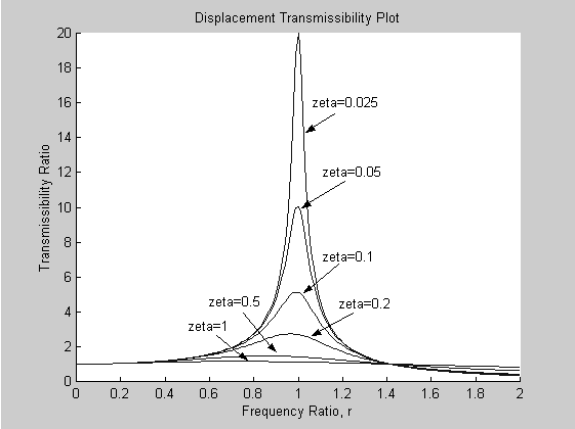

Figure 5.9: Displacement Transmissibility Curve

This plot shows how the transmissibility ratio (the relative motion between the trolley and base) changes with increasing frequency ratio ($r = \omega_b/\omega$). Now, if it is assumed that the relative motion between the wheel and base is desired to be 0.5, then the transmissibility ratio is T.R. = 0.5. With this assumption it is seen that there are numerous possible values for ζ and ω. Figure 5.10 below shows that for a T.R. of 0.5 multiple values of both ζ and r can be used. The $\zeta = 0.05$ curve is seen to intersect the T.R. = 0.5 line at r = 1.74. By assuming a truss frequency of $\omega_b = 2$ Hz $= 12.56 \frac{rad}{s}$ it is possible to determine the necessary stiffness of the wheels as follows:

$$r = \frac{\omega_b}{\omega} = 1.74 \quad \Rightarrow \quad \omega = \frac{12.56}{1.74} \quad \Rightarrow \quad \underline{\omega = 7.22 \frac{rad}{s}}$$

$$k = m\omega^2 = (1.55\ slugs)\ \frac{1\ ft.}{12\ in.}\ (7.22 \frac{rad}{s})^2 \quad \Rightarrow \quad \underline{\underline{k = 6.73 \frac{lb.}{in.}}}$$

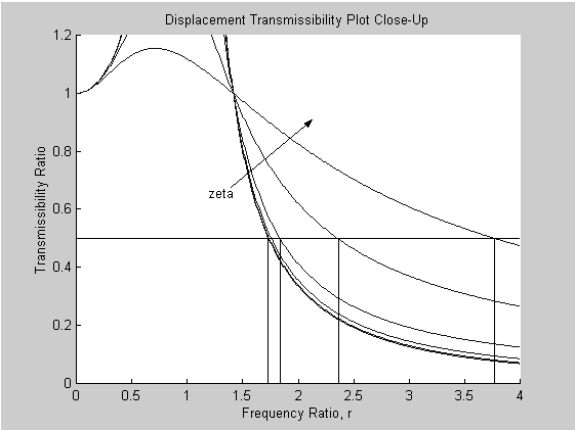

Figure 5.10: Close-Up of the Displacement Transmissibility Curve

This shows that any stiffness value greater than $k = 6.73 \frac{lb.}{in.}$ will be an acceptable value for harmonic vibration isolation.

After determining the stiffness for harmonic vibration isolation, the next step is to determine the necessary stiffness for shock isolation. To do this, the shock pulse must first be defined. The shock pulse will represent a wind gust from the environment or a large passing vehicle. To best represent a wind gust, the shock pulse will be modeled as a half sinusoid of the form:

$$p(t) = \begin{cases} P \sin \omega_p t & 0 \le t \le t_1 = \dfrac{\pi}{\omega_p} \\ 0 & t > t_1 = \dfrac{\pi}{\omega_p} \end{cases}$$

The frequency ω_p and time $t_1 = \pi/\omega_p$ determine how long the shock pulse will last. Figure 5.11 shows that the product ωt_1 is used to plot the shock transmissibility instead of the frequency ratio used for designing harmonic vibration isolators. This figure illustrates that as the pulse width increases, the acceleration that the trolley experiences will increase. Thus, to minimize the acceleration that the trolley experiences, the product ωt_1 must be small. In order to provide shock isolation the product ωt_1 must be less than 0.5 as seen in figure 5.11. For a damping ratio of $\zeta = 0.05$ and a shock pulse time of $t_1 = 1$ second, the necessary stiffness can be calculated as follows:

$$\omega t_1 = \omega(1) < 0.5 \quad \Rightarrow \quad \omega < 0.5$$

$$\omega = \sqrt{\frac{k}{m}} < 0.5 \quad \Rightarrow \quad k < (1.55\ slugs)\left(\tfrac{1\,ft}{12in}\right)\left(0.5 \tfrac{rad}{s}\right)^2 \quad \Rightarrow \quad \underline{k < 0.032 \tfrac{lb}{in}}$$

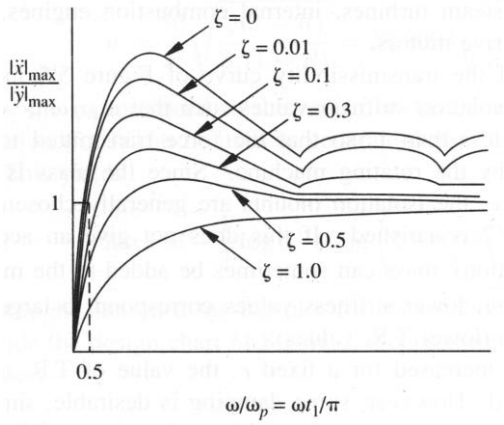

Figure 5.11: Acceleration Amplitude Ratio vs. Product of $\omega\, t_1$

(figure from *Engineering Vibration,* p.247, Ref. 13)

The above calculations show that for trolley vibration isolation due to truss vibration the stiffness of the wheels must be $k > 6.73 \frac{lb.}{in.}$ for harmonic vibration or $k < 0.032 \frac{lb.}{in.}$ for shock pulses. These opposing values create the need to choose which vibration is more common and disturbing. Of the vibration sources that the truss experiences, shock pulses will rarely, if ever, occur on the truss due to its large size, large mass, and geometry. Harmonic vibrations, on the other hand, are more likely to occur if strong steady winds blow past the truss. This vibration is due to the wind striking the freeway signs in a harmonic manner, as well as the wind blowing over the smooth cylindrical truss support posts. Wind blowing past smooth cylinders can cause rather large vibrations if the frequency of the wind and structure approach the same value. Because of this, isolation from harmonic vibration is the primary need in minimizing the amount of vibration that the truss imposes on the trolley system. Therefore, a wheel material stiffness of $k > 6.73 \frac{lb.}{in.}$ will be necessary.

5.3 Trolley Wheel Selection

In choosing a material for the trolley wheels, many factors had to be taken into account. One necessary aspect of the wheels is that they had to have good traction in order to drive

the trolley to its destination. Without good traction, the wheels will slip easily creating problems in the trolley movement and the control system. Another feature of the wheels that needs to be considered is their mechanical properties. The wheel must be able to compensate for vibration that the trolley system is subject to, and at the same time be strong enough to hold the trolley system firmly to the tracks. The wheels also need to be environmentally stable. The wheels will be exposed to heat, cold, sun, and rain. They must be able to withstand this exposure to the elements and still maintain their mechanical and good traction properties.

Taking all of the factors into consideration, the material chosen for the trolley wheels is neoprene. Neoprene satisfied most of the trolley system needs. The damping ratio of neoprene was found from Enidine's *Elastomeric Isolation Mounts Product Catalog and Selection Guide* (Ref. 15) to be $\zeta = 0.05$. The stiffness of neoprene was calculated from experimentation. A 50 lb. load was applied to a single wheel and the displacement was measured. For the 50 lb. load the wheel displaced about 0.2 inches.

$$k = \frac{65\ lb.}{0.2\ in.} = 325\,\tfrac{lb.}{in.} \quad \Rightarrow \quad \underline{k = 325\,\tfrac{lb.}{in.}}$$

From this, the natural frequency of the wheels can be calculated as follows:

$$\omega = \sqrt{\frac{k}{m}} = \sqrt{\frac{325\,\frac{lb}{in}}{(1.55\ slugs)(\frac{1\,ft}{12in})}} \quad \Rightarrow \quad \underline{\omega = 50.2\,\tfrac{rad}{s} = 8\ Hz}$$

Knowing the damping ratio and stiffness, the damping constant can be determined using the following equation:

$$b = 2\zeta\sqrt{km} = 2(0.05)\sqrt{(1.55\ slugs)(325\,\tfrac{lb.}{in.})(12\,\tfrac{in.}{ft.})}$$

$$b = 7.77\,\tfrac{slugs}{s} \quad \Rightarrow \quad \underline{b = 250.4\,\tfrac{lb}{s}}$$

These values are found to be within the calculated necessary range for the primary vibration sources. The wheel material selected is thus likely to give satisfactory vibration isolation to harmonic vibrations applied to the trolley from the truss, and to shock pulses from wind loads applied to the trolley system itself. However, for shock pulses on the truss transmitted to the trolley, the selected wheel material will not isolate vibration. This does not pose a problem, since the truss shock pulses will rarely occur due to the large size, large mass, and geometry of the truss. As for the harmonic vibrations due to wind

loads on the trolley, the wheels will isolate vibrations with driving frequencies of ω_{dr} $>100.3\frac{rad}{s}$ = 16 Hz. This shows that the wheels will isolate from these harmonic vibrations for a rather large range, making the wheel selection appropriate. Because of its isolation to the most commonly experienced vibrations, Neoprene is an acceptable selection for vibration isolation.

CHAPTER 6

ENVIRONMENTAL ANALYSIS

6.1 Rain and Sun Effects

Due to the exposure of rain, sun, and wind, the trolley system must be environmentally stable. The operating environment has been taken into consideration in the material selection of the trolley. To counteract the ill effects of rain, the tracks and many of the trolley components are made of aluminum. Aluminum's excellent resistance to corrosion will prevent any rust from occurring. In fact, aluminum forms an inert oxide film a few ten-millionths of an inch thick, covering the exposed surfaces; this blocks further oxidation and rapidly reseals any dents, scratches, or abrasions. The corrosion resistance attribute of the tracks and much of the trolley will prevent many other problems from occurring, such as increased friction and decreased strength that can occur from rusting. Parts of the trolley are made from stainless steel including the axles, motor casing, gearbox, shaft collars, bearings, and linear actuators. By using stainless steel for these parts, they will be protected from rusting as well. Cold temperatures usually accompany the rain. For aluminum, this is not a problem because it has cryogenic toughness. At very low temperatures down to near absolute zero (-273 °C), aluminum has even greater strength, ductility, and toughness than at room temperature. Therefore, the cold usually associated with rain will not adversely affect the aluminum trolley parts and tracks. The trolley wheels have an aluminum hub, but the wheel is made of neoprene. Because of its rubber-like properties, neoprene will be affected by the cold and rain; the only question is how much. Neoprene remains useful between temperatures of -40° F and 275° F. This temperature range is larger than the trolley will be subject to, making neoprene resistant to the cold and rain that it will experience. (Ref. 16)

On the other hand, the effects of the sun must also be considered. The trolley will be exposed to the harmful UV radiation from the sun and high temperatures. This will not affect the metal components on the trolley system because the temperatures will not rise high enough to affect them. The one part of the trolley that will be affected is the wheels. To compensate for the UV radiation and heat, the wheels are made of a UV stable material. Therefore, the wheels will be able to endure direct sunlight for many years. In addition, the C-channel design of the tracks will block the majority of direct sunlight on the wheels. Although the wheels will be blocked from direct sunlight, the tracks will not. Aluminum reflects heat well, but the sun can still cause the aluminum tracks to experience relatively high temperatures. The tracks themselves will not be adversely affected, but the trolley wheels may experience high temperatures via conducted heat from the tracks. By using neoprene, the wheels will be able to withstand the temperatures to which they are subject.

6.2 Aerodynamic Effects

Of the commonly experienced environmental effects, the wind has the largest effect on the trolley. When the wind hits the exposed surface area of the trolley and attached measuring device, drag forces and applied moments will be imposed on the trolley system. The larger the exposed surface area, the larger the drag force will be. The trolley can experience wind flows from all directions. For the trolley and mounted laser detector, winds that flow perpendicular to the roadway (lateral winds or crosswinds) will cause the most appreciable forces and moments on the trolley. This is because the laser detector will have the largest cross-sectional area in this direction (see figure 6.1a). The trolley system is expected to withstand 90 mph winds (the same standards set for a sign truss). Therefore, the drag force on the trolley system for a 90 mph (40 m/s) wind is calculated below:

$$D = \tfrac{1}{2}\rho v^2 C_D A$$

$$= \tfrac{1}{2}\ 1.2\ \tfrac{kg}{m^3}\ \ 40\ \tfrac{m}{s}\ (1.2)\ 0.2903\ m^2$$

$$= 334.4\ N \ \Rightarrow\ \underline{\underline{D = 75.2\ lb.}}$$

where, ρ *= density of air*
v *= wind velocity*
C_D *= laser detector drag coefficient*
A *= laser detector frontal area*

The drag coefficient of $C_D = 1.2$ was chosen using table 7.3 in *Fluid Mechanics, 3rd ed.* (Ref. 17). This drag coefficient is valid for fluid flows with a Reynolds Number greater than or equal to 1×10^4. The C_D for the lateral wind flow was determined using the assumption that the laser detector was a rectangular plate. However, the C_D for the vertical and frontal wind flows was approximated using a combination of a cube and rectangular plate. The drag coefficient for these directions was found to be slightly smaller than in the lateral wind flow direction, but 1.2 was used for all wind flow directions. This was done for simplicity and to keep a conservative calculation.

6.2.1 Lateral Wind Loads

Using a two-dimensional model, a relationship can be derived between the applied wind force (drag) and the forces at the linear actuators, thus the wheels, of the trolley. A front view of the trolley and mounted laser detector as seen by oncoming traffic is shown in figure 6.1b, and depicts a lateral wind (or crosswind) hitting the system. It shows that the laser detector is connected to the trolley via a universal mounting plate (U-plate). The connection is such that the laser detector is bolted to the U-plate and the U-plate is bolted to the trolley body. Wind hitting the laser detector will cause a moment, which will create forces on the U-plate. These forces will then be transmitted through the U-plate to the trolley body, and then to the linear actuators and wheels connected to the trolley body. Below a complete force analysis of the trolley and mounted laser detector is performed for a direct, steady crosswind hitting the center of the lateral face of the laser detector using methods and equations from *Engineering Mechanics vol. 1, Statics, 3rd ed.* (Ref. 18)

(Note: The weight of the trolley system was neglected in calculating the force on the linear actuators because it only adds excess force to the wheels. The wheels are strong enough to withstand any force that the trolley will experience, as observed in chapter 4.

The trolley system weight reduces the force that the wind applies to the linear actuators, since the weight acts against the upward wind force. For this reason the trolley system weight was neglected to allow a conservative estimate/worst-case scenario for the force applied to the linear actuators.)

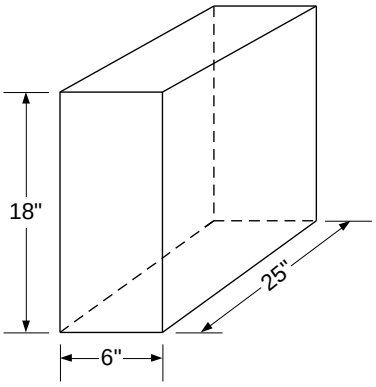

Figure 6.1a: Laser Detector Dimensions

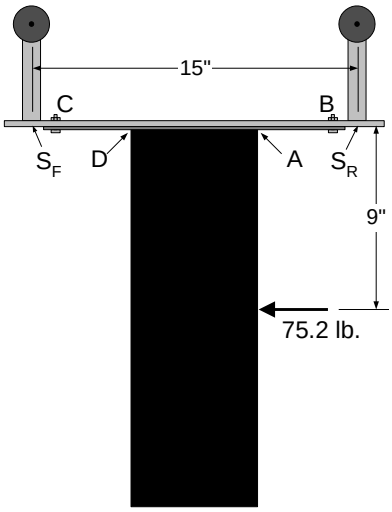

Figure 6.1b: Front View of Trolley

Free Body Diagram 1: Laser Detector

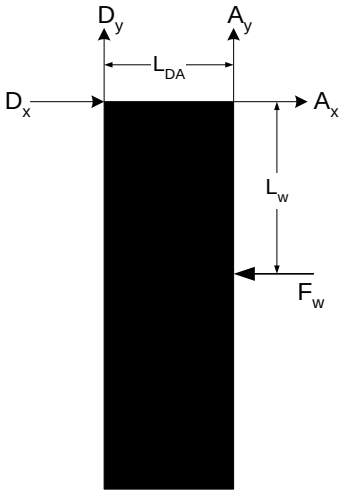

$$\Sigma F_x: \ \underline{\underline{A_x + D_x = F_w}}$$

$$\Sigma F_y: \ \underline{\underline{A_y = -D_y}}$$

$$\Sigma M_D: \ F_w L_w - A_y L_{DA} = 0$$

$$\underline{\underline{A_y = \frac{F_w L_w}{L_{DA}}}} \quad \textit{and} \quad \underline{\underline{D_y = -\frac{F_w L_w}{L_{DA}}}}$$

Free Body Diagram 2: U-plate

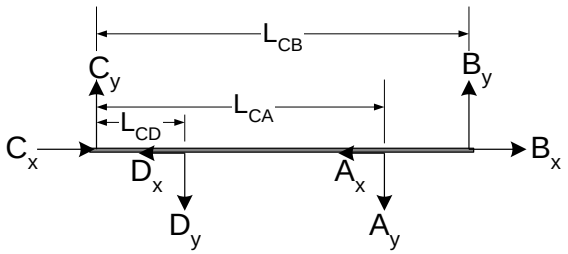

$$\Sigma F_x:\ C_x + B_x = A_x + D_x$$

from ΣF_x *in* FBD 1: $A_x + D_x = F_w \ \Rightarrow\ \underline{\underline{C_x + B_x = F_w}}$

$$\Sigma F_y:\ C_y + B_y = D_y + A_y$$

from ΣF_y *in* FBD 1: $A_y = -D_y \ \Rightarrow\ \underline{\underline{C_y = -B_y}}$

$$\Sigma M_C:\ D_y L_{CD} + A_y L_{CA} - B_y L_{CB} = 0$$

$$B_y = \frac{\left(\frac{F_w L_w}{L_{DA}}\right) L_{CA} - \left(\frac{F_w L_w}{L_{DA}}\right) L_{CD}}{L_{CB}}$$

$$\Rightarrow\ \underline{\underline{B_y = \frac{F_w L_w}{L_{DA} L_{CB}} (L_{CA} - L_{CD})}} \quad \textit{and} \quad \underline{\underline{C_y = -\frac{F_w L_w}{L_{DA} L_{CB}} (L_{CA} - L_{CD})}}$$

Free Body Diagram 3: Trolley Body

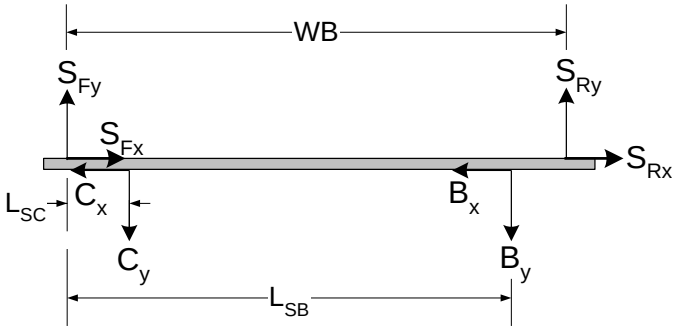

$$\Sigma F_x:\ S_{Fx}+S_{Rx}=C_x+B_x$$

from ΣF_x *in* FBD 2: $C_x+B_x=F_w \ \Rightarrow\ \underline{\underline{S_{Fx}+S_{Rx}=F_w}}$

$$\Sigma F_y:\ S_{Fy}+S_{Ry}=C_y+B_y$$

from ΣF_y *in* FBD 2: $C_y=-B_y \ \Rightarrow\ \underline{\underline{S_{Fy}=-S_{Ry}}}$

$$\Sigma M_{S_F}:\ C_yL_{SC}+B_yL_{SB}-S_{Ry}WB=0$$

$$S_{Ry}=\frac{\left[\frac{F_wL_w}{L_{DA}L_{CB}}(L_{CA}-L_{CD})\right]L_{SB}-\left[\frac{F_wL_w}{L_{DA}L_{CB}}(L_{CA}-L_{CD})\right]L_{SC}}{WB}$$

$$\Rightarrow\ \underline{\underline{S_{Ry}=\frac{\left[\frac{F_wL_w}{L_{DA}L_{CB}}(L_{CA}-L_{CD})\right](L_{SB}-L_{SC})}{WB}}}$$

and $\underline{\underline{S_{Fy}=-\frac{\left[\frac{F_wL_w}{L_{DA}L_{CB}}(L_{CA}-L_{CD})\right](L_{SB}-L_{SC})}{WB}}}$

The above equations for the front and rear linear actuator reaction forces (S_{Fy} and S_{Ry}) can be simplified using the trolley geometry. From the free body diagrams (FBD's) and figure 6.1b, it can be seen that L_{CA} - L_{CD} = L_{DA} and L_{SB} - L_{SC} = L_{CB}. Plugging these relations into the linear actuator reaction force equations gives:

$$S_{Ry}=\frac{\left[\frac{F_wL_w}{L_{DA}L_{CB}}(L_{CA}-L_{CD})\right](L_{SB}-L_{SC})}{WB}$$

$$=\frac{\left[\frac{F_wL_w}{\cancel{L_{DA}}\ \cancel{L_{CB}}}(\cancel{L_{DA}})\right](\cancel{L_{CB}})}{WB}$$

$$\Rightarrow\ \underline{\underline{S_{Ry}=\frac{F_wL_w}{WB}}}\quad \textit{likewise,}\quad \underline{\underline{S_{Fy}=-\frac{F_wL_w}{WB}}}$$

With this, a single equation can be written to represent the magnitude of the reaction force on the linear actuators on one axle as follows:

$$\boxed{S=\frac{F_wL_w}{WB}}$$

(Note: If the trolley system weight were taken into account, similar analysis would show the above equation to be, $S = \frac{F_w L_w}{WB} - \frac{W_T}{2}$ *where,* W_T *is the trolley system weight*.)

This derived equation makes it possible to determine the forces generated on an axle of the trolley. Each axle has two linear actuators, so this force, S, will need to be divided by two to find the force on a single linear actuator.

$$\boxed{S_1 = \frac{S}{2} = \frac{F_w L_w}{2WB}}$$

(*force on each linear actuator*)

By knowing the generated force on a single linear actuator, it is possible to select the proper linear actuator to withstand the generated force. In addition to this, with the trolley system weight taken into account, similar analysis shows the force on a single wheel to be,

$$S_{1W} = \frac{F_w L_w}{2WB} + \frac{W_T}{4}$$

and from this, the applied forces and moments on the axles can then be determined.

From the above force analysis, a simple equation has been derived to relate the applied wind force to the forces at the linear actuators, which has been named the "wind equation." By inspection, it is noticed that a much simpler model can be used instead of doing a complete force analysis on the laser detector, U-plate, and trolley body. This simplified model is named the "T-model" and is shown below:

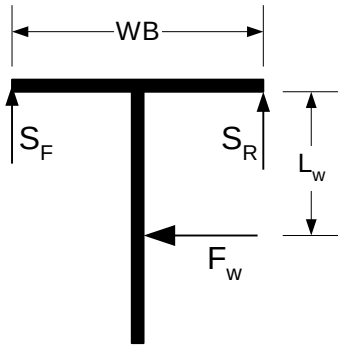

Figure 6.2: T-model of Trolley System

The T-model assumes that the applied wind force acts along the centerline (horizontal centerline running in and out of the paper) of the laser detector. It is common practice to model the combined forces over the entire side of a body as a single force at the center of that side. Furthermore, since it has been shown that the forces will be transmitted through the U-plate, there is no reason to include it in the analysis for determining the forces on the trolley. Also, due to the laser detector being firmly bolted to the U-plate and the U-plate firmly bolted to the trolley, it can be assumed that the laser detector is rigidly attached to the trolley. It is by excluding the U-plate, assuming a centerline action of force, and assuming a rigid connection that the T-model emerges. These are all reasonable assumptions and the will expedite further analysis on the trolley. Below the T-model is proven to give the same result as the complete force analysis in only one step.

$$\Sigma M_{S_F}: \; F_w L_w - S_R WB = 0$$

$$\underline{\underline{S_R = \frac{F_w L_w}{WB}}} \quad \textit{likewise,} \quad \underline{\underline{S_F = -\frac{F_w L_w}{WB}}}$$

Through similar analysis, it can be shown that the T-model can also be used for wind forces acting on the frontal face of the laser detector. For this reason, the wind equation is valid for all horizontal wind flow that hits the laser detector. The wind equation allows for variance in the trolley geometry as well as variance in the point of application of the

wind load. Therefore, if the trolley were to be made longer or wider, or if the point of wind application differed, the wind equation could be used to find the new forces on the linear actuators. In addition, if the wind were known to be concentrated at a certain point vertically on the laser detector (i.e. the wind force is determined to be larger at the bottom of the detector than the at the top), the wind equation could still be employed to determine the forces at the linear actuators.

After deriving the wind equation, the next step is to determine the drag force on the trolley system. Table 6.1 below shows the drag force applied to the laser detector for the wind hitting the lateral side center of the detector for various wind speeds.

C_D	ρ (kg/m^3)	μ (kg/m-s)	L (m)	Frontal Area (m^2)	Velocity (m/s)	Velocity (mph)	Reynolds No.	Drag Force (N)	Drag Force (lb)
1.2	1.2	1.80E-05	0.152	0.2903	5	11.2	5.07E+04	5.23	**1.18**
1.2	1.2	1.80E-05	0.152	0.2903	10	22.4	1.01E+05	20.9	**4.7**
1.2	1.2	1.80E-05	0.152	0.2903	15	33.6	1.52E+05	47.03	**10.57**
1.2	1.2	1.80E-05	0.152	0.2903	20	44.7	2.03E+05	83.61	**18.8**
1.2	1.2	1.80E-05	0.152	0.2903	25	55.9	2.53E+05	130.64	**29.37**
1.2	1.2	1.80E-05	0.152	0.2903	30	67.1	3.04E+05	188.11	**42.29**
1.2	1.2	1.80E-05	0.152	0.2903	35	78.3	3.55E+05	256.04	**57.56**
1.2	1.2	1.80E-05	0.152	0.2903	40	89.5	4.05E+05	334.43	**75.18**

Table 6.1: Applied Wind Force on Lateral Face of Laser Detector

Now the wind equation will be put to use to calculate the forces at the linear actuators due to a given wind force on the lateral face of the laser detector:

Given: A wind gust with a velocity of $40\ \frac{m}{s}$ $(90\ mph)$ creating a drag force of $F_w = 334\ N\ (75\ lb)$ applied to the laser detector, with the wind acting at the center of the laser detector $[L_w = 0.2286\ m\ (9\ in)]$. Employing the wind equation gives:

$$S_1 = \frac{F_w L_w}{2WB} = \frac{(334\ N)(0.2286\ m)}{2(0.375\ m)} \quad \Rightarrow \quad \boxed{S_1 = 101.8\ N\ (23\ lb.)}$$ on a single linear actuator.

With the laser detector mounted to the trolley, it is noticed that the wind can apply significant forces to the trolley via drag forces on the lateral face of the laser detector. However, this 23 lb. force that is applied to a single linear actuator is well within the 50 lb. holding force of the linear actuators.

6.2.2 Vertical Wind Loads

In addition to the crosswinds, vertical and longitudinal winds can also play a part in creating undesirable forces on the trolley. Vertical winds will be mainly due to large trucks passing under the trolley. In performing an analysis on the vertical wind speed imposed on the trolley, it is noticed that the truck can experience rather large wind speeds. The wind speed that the truck experiences is composed of two parts, the actual wind speed, V_w, and the vehicle speed, V_T. These two values add to form the relative wind speed that the truck experiences, V_{rel}.

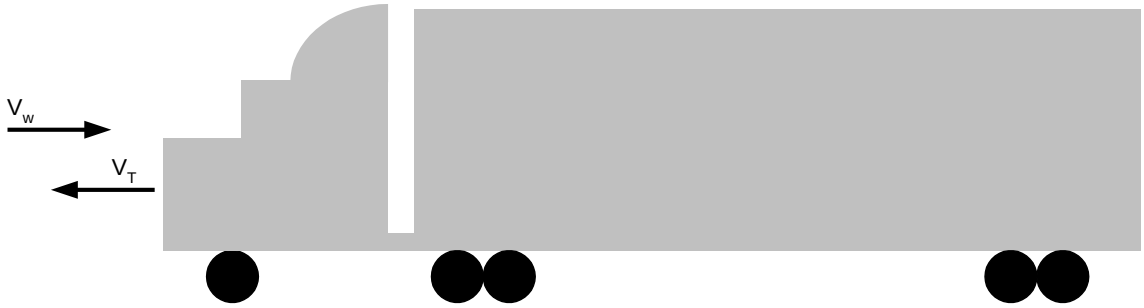

Figure 6.3: Truck Wind Speed Breakdown

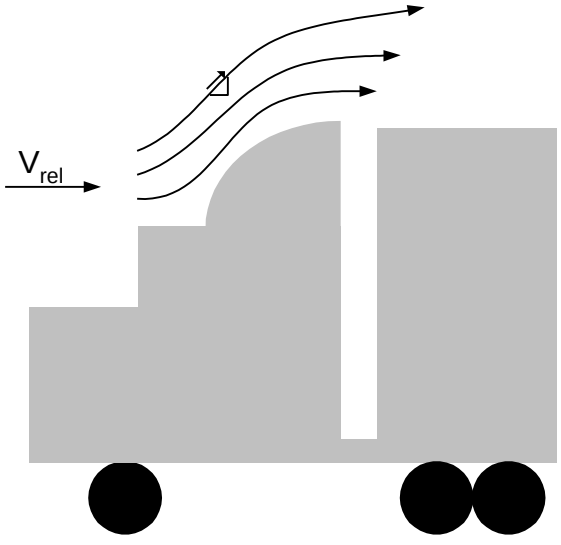

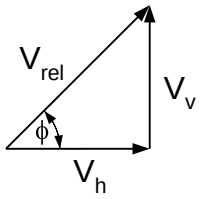

Figure 6.4a: Boundary Layer Over Truck

Figure 6.4b: Wind Flow Geometry

Many trucks are designed to reduce the amount of drag that the vehicle experiences. As wind flows over the truck (see figure 6.4a), a boundary layer is formed over the top of the truck. The boundary layer causes the wind to flow smoothly over the truck, thereby reducing the drag force that the truck experiences. This boundary layer also causes the wind to undergo a direction change. The direction change is what creates the vertical wind force on the trolley system. The change in angle of the wind flow, ϕ, is assumed to be 45°. In addition, the truck velocity is assumed to be 60 mph and the actual wind velocity 60 mph, creating a relative velocity of 120 mph. A 60 mph wind speed is very high and uncommon. However, this speed was chosen to put the trolley system under maximum load. Since the relative wind velocity is at an angle, only the vertical component is needed. With the relative wind velocity at a 45° angle from the horizontal, the vertical wind speed is found to be:

$$V_v = V_{rel}\sin\phi = \frac{V_{rel}}{\sqrt{2}}$$

Plugging the assumed relative velocity into the above equation gives a vertical component of V_v = 84.9 mph. This is the maximum vertical wind speed that the trolley will experience if the trolley were only inches away from the passing truck. The actual wind speed that the trolley will experience from the passing truck will be much less due to its further distance above the truck. The average truck height is 12.5 ft. and the trolley will be at a minimum height of 16 ft. but an average height of 18 ft. This gives a minimum of 3.5 ft. between the truck and the lowest part of the trolley. With this large of a gap, the wind will not be at full speed. Other factors, such as truck geometry and wind direction, will create slower wind speeds as well. Under normal circumstances, the trolley will be subject to only the wind force from the 60 mph passing truck. This creates a normal vertical wind gust of 42.4 mph, but not all of this speed is imposed on the

trolley system. Table 6.2 below shows the drag force imposed on the trolley system due to vertical winds for various wind speeds.

C_D	ρ (kg/m^3)	μ (kg/m-s)	L (m)	Frontal Area (m^2)	Velocity (m/s)	Velocity (mph)	Reynolds No.	Drag Force (N)	Drag Force (lb)
1.2	1.2	1.80^{E}-05	0.457	0.1896	5	11.2	1.52E+05	3.41	**0.77**
1.2	1.2	1.80^{E}-05	0.457	0.1896	10	22.4	3.05E+05	13.65	**3.07**
1.2	1.2	1.80^{E}-05	0.457	0.1896	15	33.6	4.57E+05	30.72	**6.91**
1.2	1.2	1.80^{E}-05	0.457	0.1896	20	44.7	6.09E+05	54.6	**12.27**
1.2	1.2	1.80^{E}-05	0.457	0.1896	25	55.9	7.62E+05	85.32	**19.18**
1.2	1.2	1.80^{E}-05	0.457	0.1896	30	67.1	9.14E+05	122.86	**27.62**
1.2	1.2	1.80^{E}-05	0.457	0.1896	35	78.3	1.07E+06	167.23	**37.59**
1.2	1.2	1.80^{E}-05	0.457	0.1896	40	89.5	1.22E+06	218.42	**49.1**

Table 6.2: Applied Wind Force on Bottom of Laser Detector and Trolley Body

Since the applied wind force is acting vertically, the force applied to each linear actuator is simply the drag force divided by four. For a 90 mph wind it is seen that the force on each actuator is 12.3 lb. This equates to about half the applied force as in the crosswind case. Therefore, the applied wind force from passing trucks or winds does not pose a threat to the trolley system.

6.2.3 Longitudinal Wind Loads

The longitudinal winds (or headwinds) have been noticed to produce rather small forces on the trolley system as well. The reason for this is because the front of the laser detector has the smallest frontal area. This causes minute drag forces to be imposed on the trolley. The drag forces for various wind speeds are calculated below:

C_D	ρ (kg/m^3)	μ (kg/m-s)	L (m)	Frontal Area (m^2)	Velocity (m/s)	Velocity (mph)	Reynolds No.	Drag Force (N)	Drag Force (lb)
1.2	1.2	1.80E-05	0.635	0.0695	5	11.2	2.12E+05	1.25	**0.28**

1.2	1.2	1.80E-05	0.635	0.0695	10	22.4	4.23E+05	5	**1.12**
1.2	1.2	1.80E-05	0.635	0.0695	15	33.6	6.35E+05	11.26	**2.53**
1.2	1.2	1.80E-05	0.635	0.0695	20	44.7	8.47E+05	20.02	**4.5**
1.2	1.2	1.80E-05	0.635	0.0695	25	55.9	1.06E+06	31.28	**7.03**
1.2	1.2	1.80E-05	0.635	0.0695	30	67.1	1.27E+06	45.04	**10.13**
1.2	1.2	1.80E-05	0.635	0.0695	35	78.3	1.48E+06	61.3	**13.78**
1.2	1.2	1.80E-05	0.635	0.0695	40	89.5	1.69E+06	80.06	**18**

Table 6.3: Applied Wind Force on Front of Laser Detector

To calculate the forces applied to each linear actuator, the wind equation can be used as seen below:

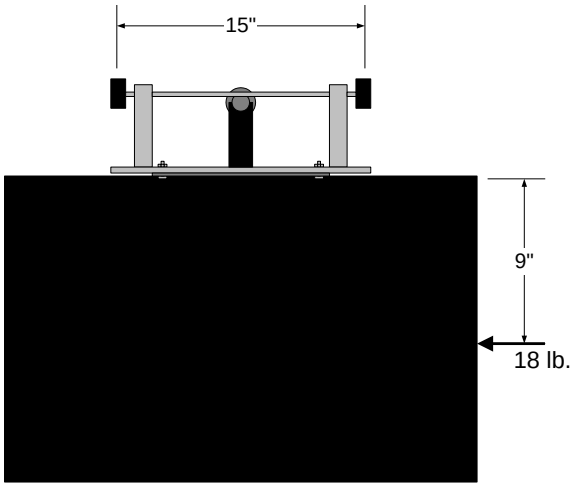

Figure 6.5: Assumed Point of Wind Load on Trolley System

$$S_1 = \frac{F_w L_w}{2WB} = \frac{(18\ lb.)(9\ in.)}{2(15\ in.)} \quad \Rightarrow \quad \underline{\underline{S_1 = 5.4\ lb.}}$$

The largest drag force, which occurs at 90 mph, was used to calculate the force applied to the linear actuators. Even with the largest drag force, each linear actuator will only experience a 5.4 lb. of force. This is very small and can be neglected.

After analyzing the wind force on all sides of the trolley and laser detector, it is determined that the wind forces are largest in the lateral wind direction, and therefore pose the greatest challenge to the trolley system. However, the trolley is designed to easily withstand the large drag forces to which it is exposed through the use of the linear actuators.

By taking the trolley system weight into account, the equation for S_{1W} (seen in section 6.2.1) makes it possible to determine the force applied to the wheels; the resulting forces and moments applied to the axles can then be determined. In order to perform an analysis of the loads on the axles, the cantilevered axle model from section 4.1 was used. The only difference in the analysis from section 4.1 is that the wind equation was used to determine the force on the axles instead of the trolley weight. Since the trolley is designed to withstand a 90 mph wind, this speed was used to determine the maximum force applied to the wheels. The drag force on the laser detector for a 90 mph wind was determined to be 75.2 lb., creating a maximum force on the wheels of S_{1W} = 36 lb. This value was then used to evaluate the forces, moments, and deflection of the axles. It was found that the maximum moment on the axles was M = 60.3 in.-lb. with a maximum shear force of V = 36 lb. The shear and moment diagrams are of the same shape as in section 4.1.3, but have the above values of maximum shear and moment. The maximum deflection of the axles as a result of the 36 lb. per wheel wind load was found to be y_{max} = 0.0034 in. The factor of safety was calculated to be $\eta = 3$.

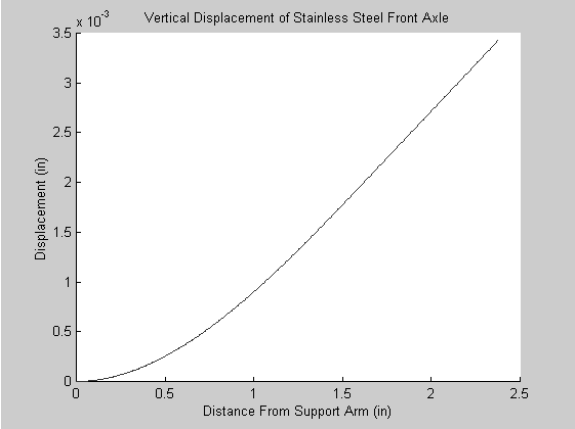

Figure 6.6: Vertical Displacement of the Trolley Due To Wind Load

The analysis performed was a worst-case scenario and the trolley system still held up to the conditions. Since the laser detector will be the largest device mounted to the trolley, the system will certainly be stable with other devices (camera, radar detectors, etc.)

mounted. The trolley has been made with environmentally robust materials. This helps the system resist the ill effects caused by the rain and sun.

CHAPTER 7

MANUFACTURING PROCESS

The first stage of the manufacturing process was to make rough cuts on the axles and trolley body. The axles and trolley body were cut to length and the cut ends were sanded flat. The trolley support arms (see figure 7.1) were the next part that were fabricated. The support arms are made of 1.25" square aluminum shafting. First, each of the four support arms was cut to an approximate length 5.7". The ends of each piece were machined square and then cut to a length of 5.5" using the end mill. The bearing slots were machined next. An edge finder was used in the end mill to determine the precise location of the support arm on the mill table. A 0.5" hole was then drilled through each of the support arms at the predetermined precise location. Next, a program was created on the end mill to machine a 0.875" diameter bearing slot, centered at the center of the 0.5" hole in the support arm. The program was needed because a 0.875" mill bit was not available. Using the program, a bearing slot was machined on the two sides of the 0.5" hole on each support arm to a depth of 0.28". This machining operation created the four trolley support arms as seen below.

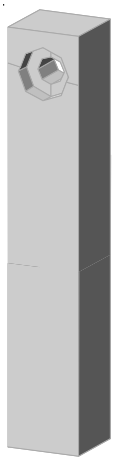

Figure 7.1: Single Trolley Support Arm

Following the completion of the support arms, the trolley body was machined square. This was done using the mill and a square. The trolley body was placed on the mill table and one side was aligned square with the table edge. Another side of the trolley body was machined square with the aligned edge. Once square, the trolley body was rotated 90° and the machined edge was aligned square with the mill table. The next side was then machined square with the aligned edge. This was continued until all edges of the trolley body were square with one another.

Now that the trolley body and support arms were cut to size, the next step was to connect them together. This connection needed to be extremely precise. If the holes in the trolley body did not align near exactly, the axles would not fit into support arms properly. To do the machining for the connection holes, the mill was again used. First, the holes were planned, measured, and marked by hand to their precise locations. The marks were used for a double check to ensure that the holes were drilled in the proper locations. The holes in the support arms were drilled first. Three holes were drilled in a triangular pattern in their precise locations as seen in figure 7.2. For ease of machining, a mill stop was used so each support arm could be placed into position quickly, drilled, and removed. In addition, since all of the holes are the same for each support arm, a program was made on the mill. The program specified the hole position in reference to an origin (0,0) point. The program automatically moved the support arm into a precise position for each hole to be drilled.

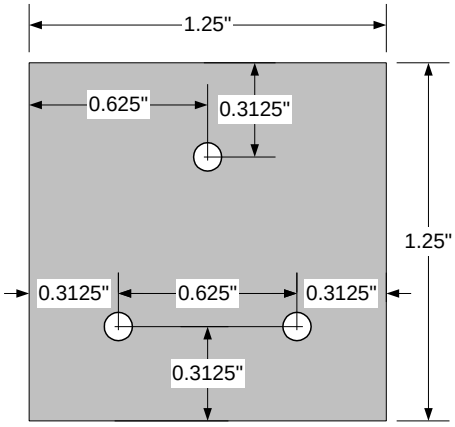

Figure 7.2: Support Arm Hole Location

After drilling the holes in the support arms, each hole was tapped to fit an #8-32 size screw. Next, the corresponding holes on the trolley body were drilled using the mill for accurate hole positioning. The trolley body was aligned square to the mill table and an edge finder was used to create an origin (0,0) point on the trolley body. The pre-planned and marked holes were then drilled with the aid of the digital readout on the mill for precise positioning. The holes were drilled to match up with the support arm connection holes and a second set of five holes were drilled to match up with the linear actuator connection points. The front connection holes were drilled first without moving the trolley body. This allowed the distance from the front of the trolley body to the front axle to remain constant, which ensured that the front support arms would be coaxial. Once the front holes were drilled, the trolley was rotated 180° and the same process was performed for the rear holes. In all, eight holes were made on each corner of the trolley body for a total of 32 precisely aligned holes. Figures 7.3a and 7.3b below show the hole positioning and alignment.

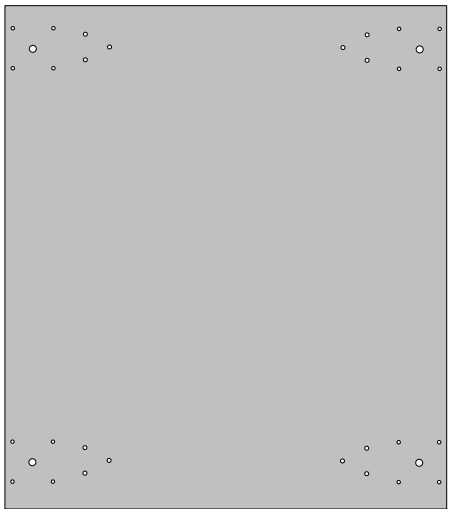

Figure 7.3a: Trolley Body Hole Location

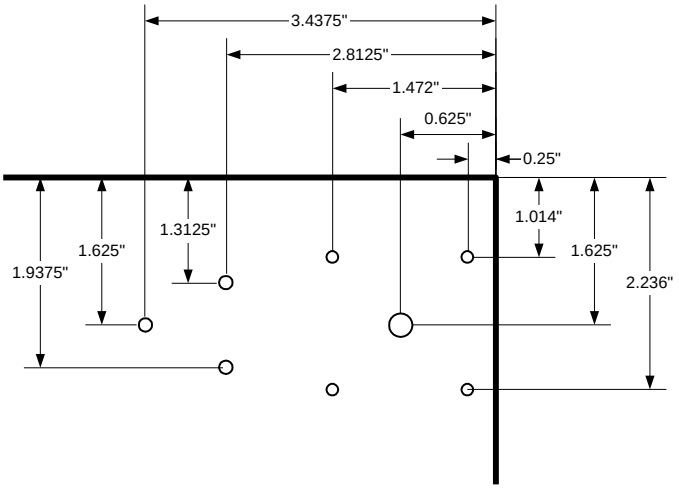

Figure 7.3b: Trolley Body Hole Location Detail

Now that the holes were drilled, the support arms and linear actuators were attached to the trolley body. All of the holes were countersunk to eliminate the possibility of bolt head interference, and to give the underside of the trolley a pleasing look. With the support arms and linear actuators in place, the next task was to put the axles, wheels, shaft collars, and shaft couplings into place and secure them. Following this, four 1”

square pieces of 1/4” aluminum were cut, smoothed, and tapped in the center with an #8-32 thread. These aluminum pieces were connected to the linear actuator shaft ends and used to distribute the holding force delivered by the actuators. Rubber pads were then attached to the aluminum pieces to give them a high friction surface.

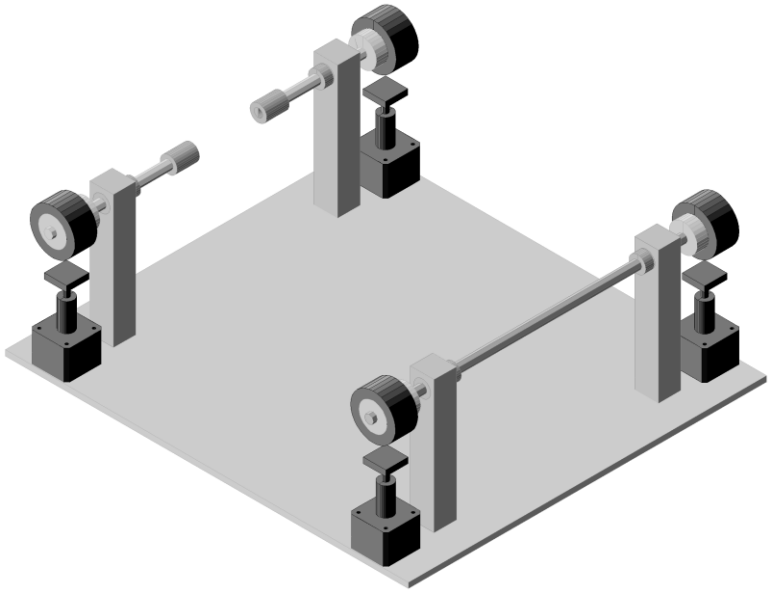

Figure 7.4: Halfway Completed Trolley

Following this, the power connection arms and lateral constraint axle end caps were constructed and attached to the trolley. First the power connection arms were fabricated using two 3/4” x 1/16” strips of brass. The two strips were cut to a length of 7” and the bottom 1” of the strips was bent to a 90° angle. Two connection holes were drilled into the 1” bent section of the strips. Then, a 1” x 1/4” slot was milled into the strips at the top (see figure 7.5a). The slots allow the brushes to be repositioned to maintain proper contact with the tracks after excessive wear. Next, corresponding holes were drilled on the trolley body to attach the power connection arms. To electrically isolate the power connection arms from the trolley, a piece of rubber was placed between the trolley body and each arm, and plastic countersink screws were used for attachment. A piece of 3/8”

diameter Delrin shaft was used to make the lateral constraint axle end caps (see figure 7.5b). The end of the shaft was rounded to a hemisphere and then cut to 1/4" length. These fabricated hemispheres were then glued to the ends of the axles.

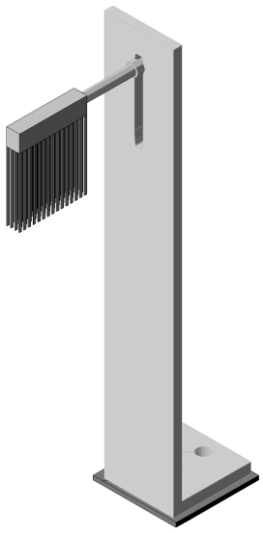

Figure 7.5a: Power Connection Arm and brush

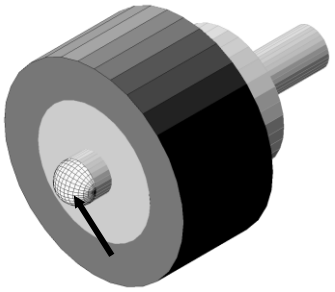

Figure 7.5b: Lateral Constraint Axle End Cap

At this point the trolley system was nearly ready for testing. The only parts needed were the gearbox mount, motor mount, and tracks. The gearbox and motor mounts were the next items that were fabricated. Each mount was made of a 2" square by 4.25" tall block of Delrin. The blocks were cut to size and shaped to fit the gearbox and motor. Each mount is connected to the trolley body using three #10-24 screws arranged in a triangular pattern. The gearbox mount has a flat top, but the motor mount had to have a concave top machined into it to accommodate the cylindrical motor casing. The gearbox has three connection holes that are used to connect it to the gearbox mount. The motor was more difficult to connect to its mount. A piece of rubber was placed between the motor and the motor mount to help prevent the motor from spinning on the mount. In order to hold the motor in place, a Velcro motor strap is used. This strap is simply a piece of Velcro that is attached to the sides of the motor mount using screws. The Velcro is a cinch type strap

that allows for a tight holding force against the motor. A piece of rubber is stuck on the inside of the Velcro where it contacts the motor to further help prevent the motor from spinning. With the mounts fabricated, the motor and gearbox were connected to the trolley.

Now that the motor and gearbox were mounted, the next task was to construct a pair of tracks for the trolley to ride on. Two pieces of channel aluminum are used as the tracks. The pieces of channel aluminum are 8 ft. long and connected together near the ends to keep the tracks a fixed 12.5" apart. The tracks were connected together using two pieces of 1" x 3/4" x 1/16" channel aluminum. Each track connector channel is attached to the tracks using four #10-24 screws (two for each track). To electrically isolate the tracks from each other, a piece of rubber is placed between the connector channels and the tracks. In addition, a rubber grommet and plastic washer is used with each screw. Once firmly connected and electrically isolated from each other, the tracks were set between two tables, and the trolley was mounted to them. Now the trolley was complete, and the initial testing phase was ready to begin (see figure 7.6).

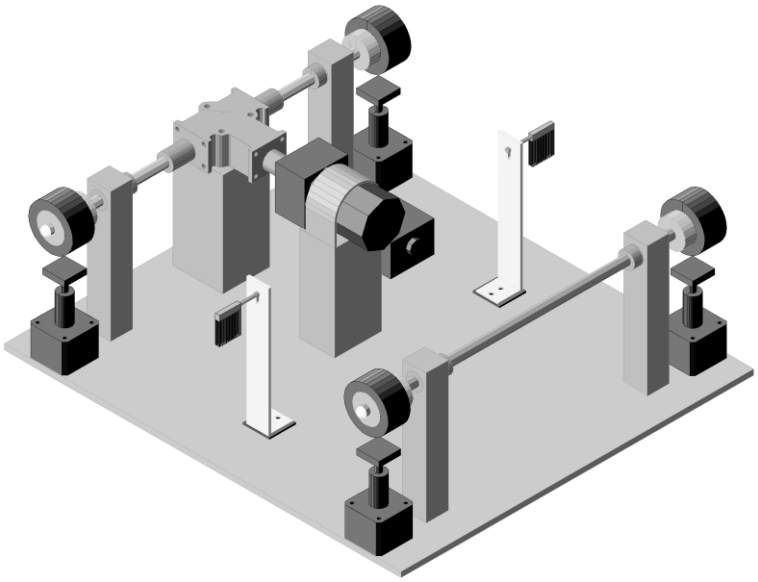

Figure 7.6: Trolley Ready For Testin

CHAPTER 8

PROTOTYPE TESTING

To begin testing of the trolley system, a motor with 100 oz.-in. of torque was connected to the trolley. The purpose for using this motor was to physically test the trolley system to estimate the amount of motor torque needed. With the motor attached to the trolley, it was then connected to a power source and turned on. Through testing it was determined that the motor had enough torque to drive the unloaded trolley. However, when approximately 30 lb. of weight was added to the trolley, the motor had a very difficult time starting up and continuing movement. This showed that a 100 oz.-in. motor would not be sufficient. In order to correct this problem, calculations were performed (see chapter 4) that determined a motor with 480 oz.-in. of torque should be sufficient (see figure 8.1). The new motor was tested by adding approximately 30 lb. of weight to the trolley and starting it from rest as well as driving it continuously. The motor proved to have enough torque to drive the loaded trolley easily.

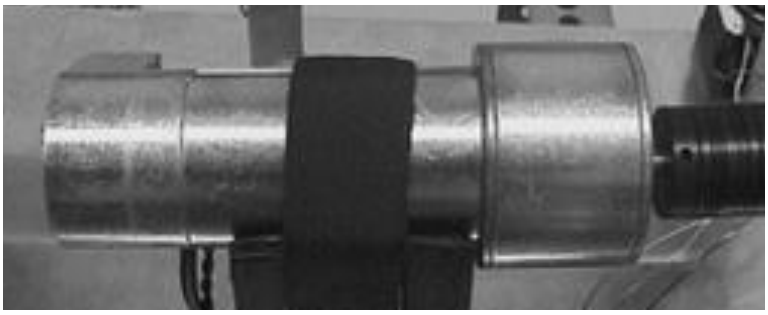

Figure 8.1: 480 oz.-in. Motor Used with Trolley System

The next testing that was performed was to evaluate the effectiveness of the lateral constraint end caps (see figure 8.2). The trolley was tested with and without the lateral constraint axle end caps to demonstrate their effectiveness. Without the caps, it was found that the trolley would twist and turn slightly on the tracks causing the axle ends to rub harshly against the inside of the tracks. This twisting and rubbing caused the trolley to experience difficulty moving. The end caps were then added to the axles and it was found that the trolley rode straight and smoothly on the tracks. This proves that the lateral constraint axle end caps are both effective and necessary.

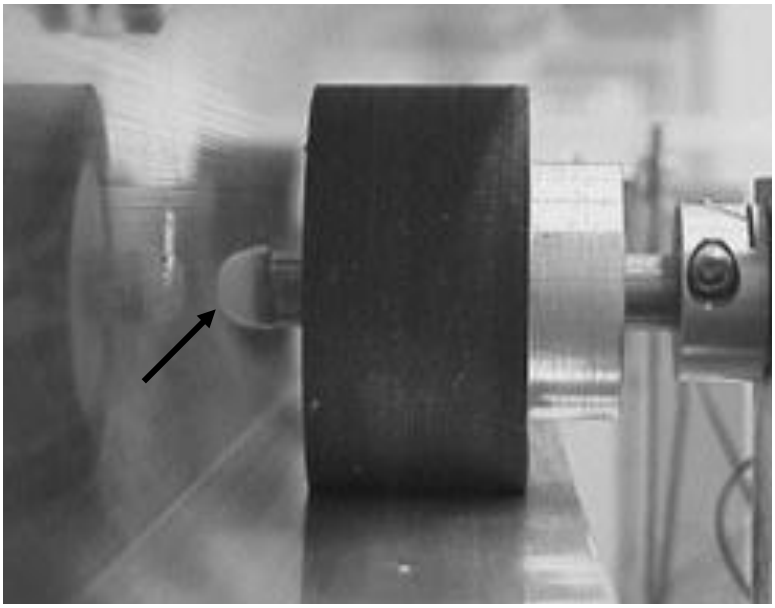

Figure 8.2: Lateral Constraint Axle End Cap

To show that the system can be truly wireless, testing on the power connection method was performed. To do this, the electrically isolated tracks were connected to a power supply. One track was connected to the positive lead and the other to the negative (see figure 8.3a). The trolley power connection brushes were adjusted to rub along the tracks properly and the power was turned on (see figure 8.3b). The trolley started moving immediately, which was the desired response, making the trolley system a success up to this point.

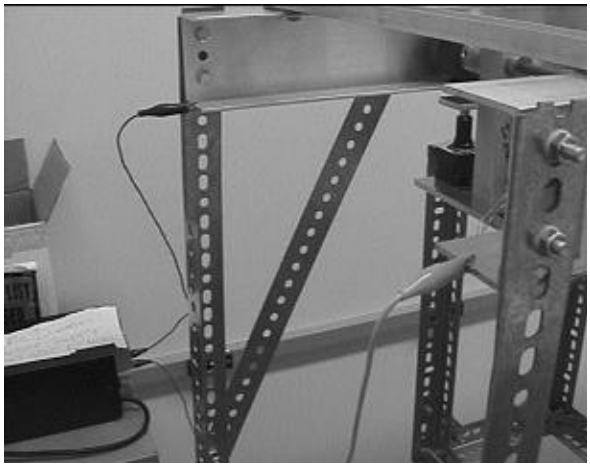

Figure 8.3a: Track Power Connection

Figure 8.3b: Power Connection Arm and Brush

The next testing procedure for the trolley system was to simulate the presence of the laser detector on the trolley system and examine how the trolley system would operate with the detector in place. To do this, the tracks were mounted on a five-foot tall support, designed and manufactured by two UC Davis undergraduate students. This mount provided the necessary height to simulate a sign truss and perform tests on the trolley system with mounted laser detector. Due to its delicate and unfinished status, the actual laser detector was not connected to the trolley. However, the actual laser detector mounting frame was used by connecting it to the U-plate, which was connected to the trolley (see figure 8.4a). Instead of the actual laser detector, an object with about the same weight was mounted on the laser detector frame (see figure 8.4b). The trolley system was powered and the entire system moved along the tracks rather well.

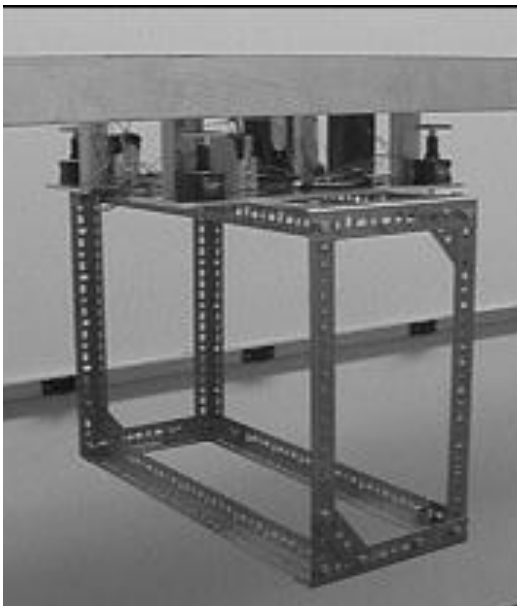

Fig. 8.4a: Trolley with Laser Detector Frame

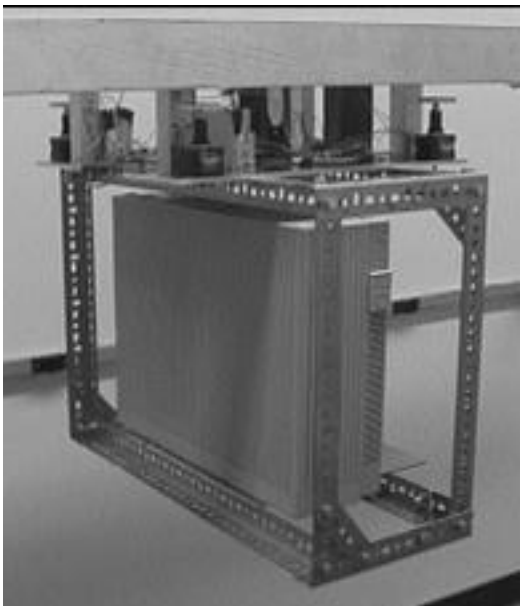

Fig. 8.4b: Trolley with Simulated Laser Detector

The drive system was then further tested by applying a force to the laser detector to simulate a direct lateral wind. It was found that the motor would drive the loaded system, subject to an applied force, with full power until the wheels slipped. Friction at the wheels was determined to be the limiting factor for an applied external force. This is the expected result according to the calculations performed in chapter 4.

At this point the trolley system had confidently passed all normal operating condition tests for the moving trolley. Therefore, it was time to test the robustness of the trolley system. To do this, a rather large impediment (approximately 0.25" tall and 1" wide) was placed on the wheels riding surface on one side of the tracks (see figure 8.5a). The fully loaded trolley was driven over the impediment both forwards and backwards (see figure 8.5b). It was found that the trolley had sufficient power to overcome the impediment without twisting, significant slowing, or excessive vibration. This shows that the motion of the trolley system would not be hampered by the presence of debris on the tracks.

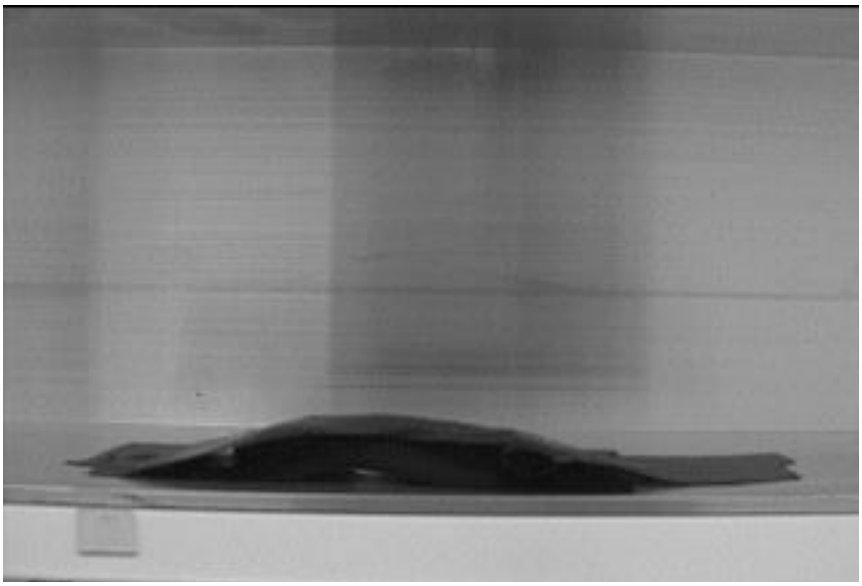

Figure 8.5a: Impediment Used to Test Trolley

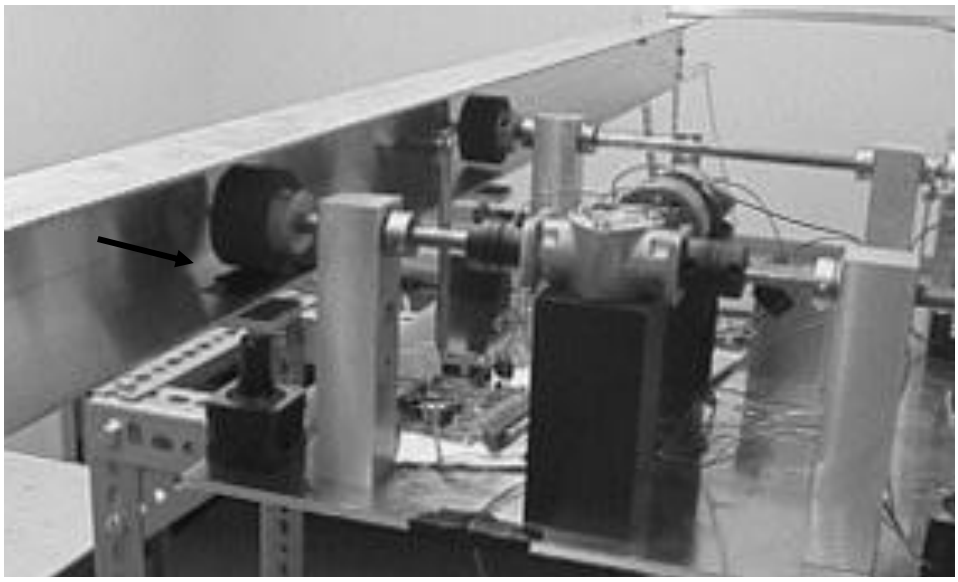

Figure 8.5b: Trolley Overcoming Impediment

The next test for robustness was to examine the trolley's ability to operate in the rain. First, only one track was wetted and the trolley was driven across the tracks. This did not affect the trolley's ability to move; it did not slip, twist, or slow down. Next, both tracks were wetted to simulate operation during a rainy day. The trolley was driven over the wetted tracks without noticeable slipping, twisting, or slowing down. Since wind often

accompanies rain, an exterior force of approximately 30 lb. was applied to the laser detector while the trolley drove over the wetted tracks. This caused the trolley wheels to slip and cease the trolley movement. With a wet track, it takes less force to cause the trolley wheels to slip than when the tracks are dry. This was expected due to the decreased coefficient of friction of the wet tracks. Nevertheless, the trolley proved to be operational during a simulated rainy and moderately windy day. Again, this was shows the trolley system to be rather robust.

After finding that the trolley drove well with the mounted laser detector, the next test was to find out how the system operated while in a static position. To do this, the static constraint system was employed, locking the system into position (see figure 8.6a). The first test was a vibration test. The hanging laser detector mount was struck numerous times on different sides to simulate a wind gust. The vibration of the trolley system was visually inspected and found to diminish rapidly, ceasing after approximately one second. Next the tracks were vibrated with different amplitudes causing the trolley to vibrate in response. Again, the vibration that the trolley system experienced was minimal and ceased quickly. The visual vibration inspection was used because no instrumentation was available, and since the acceptable vibration for the laser detector is not yet quantified, the trolley was designed to minimize vibration as best as possible.

Figure 8.6a: Static Constraint System Engaged *Figure 8.6b: Static Constraint System Disengaged*

The vibration noticed was almost completely due to the instability in the tracks, not the trolley system. Without manually holding the tracks from moving (which was done for the vibration test mentioned above) the vibrations were slightly larger. These larger vibrations that occurred were due to the unstable track mount. The track mount was built tall but not wide, which created instability to vibrations. In addition, the tracks were supported eight feet apart. This was done for ease of testing, however on the actual truss, the tracks will be supported a maximum of every 5.5 feet. The large distance between the track supports and unstable track mount led to twisting of the tracks, which created excess vibration to be experienced. Even with this instability, the trolley system showed to cease vibration after only approximately two seconds.

The next test that was performed was to simply observe the strength of the linear actuators grip on the tracks when the trolley system is stationary. The trolley was pushed, pulled, and struck with rather large forces on all sides, yet no slippage occurred and the system remained firmly attached to the tracks. This shows that the trolley would not get displaced from its precise position over traffic, due to external forces. This test also validated the calculations made in chapter 6, illustrating that the linear actuators are twice as strong as they need to be.

Since the linear actuators each have a 50 lb. holding force, a wheel deformation test was also performed. For this test, the linear actuators were engaged against the tracks to lock the trolley in place. This caused the wheels to deform slightly due to the large applied force (see figure 8.7). The trolley system was kept locked in place with deformed wheels for just over two weeks. The linear actuators were then disengaged and the trolley was driven. It was found that there was no noticeable permanent deformation of the wheels. If permanent wheel deformation were to occur, the trolley would experience a bumpy ride. This is not detrimental but is slightly undesirable.

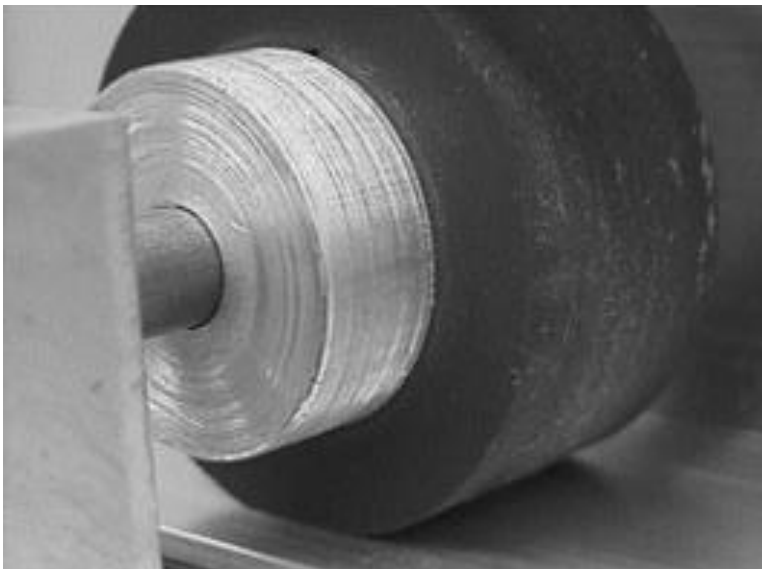

Figure 8.7: Deformed Wheel

With the trolley system performing extremely well, the backup battery was the next item to be tested. To do this, a four-inch section on one side of the tracks was covered with electrical tape to cause one brush to lose electrical contact with the tracks, thereby breaking the electric power circuit. The trolley was first driven over the discontinuous section, with the battery detached to see if an electrical isolation existed. The trolley was unable to pass the section, regardless of which direction it was traveling. The backup battery was then connected to the motor in parallel with the track delivered power source (see figure 8.8a). The trolley was driven over the discontinuous section again and was able to continue past the section (see figure 8.8b). This shows that the backup battery works and will ensure that the trolley gets to its destination.

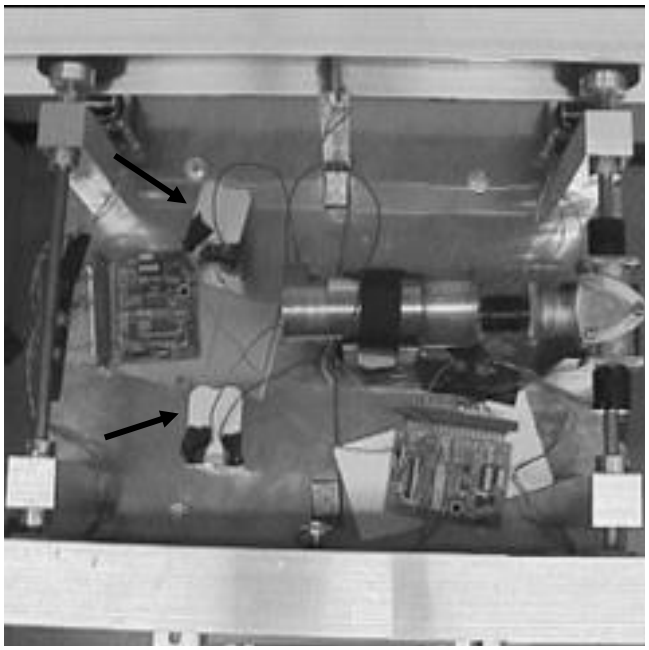

Figure 8.8a: Backup Batteries

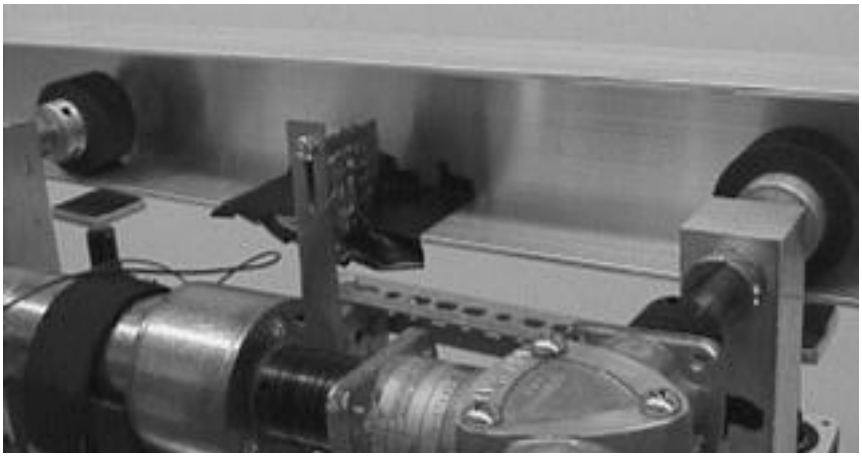

Figure 8.8b: Trolley Overcoming Discontinuous Section Using Backup Batteries

After testing the various possible failure modes of the trolley, the tracks were put to a couple of simple strength tests. To test the bending strength of the tracks, a 200 lb. load was applied to the pair of tracks that were supported eight feet apart. The tracks were noticed to deform slightly, but plastic deformation did not occur. Part of the observed

deformation most likely was due to instability and weakness in the track mount. With this in mind, and the fact that the track connections were eight feet apart instead of the 5.5 feet that will be used, the tracks will easily support the trolley system load. The next test was to test the strength of each track individually. This experiment tested for track strength from wind loading on the trolley. Winds will cause a torque about the center of the tracks, creating equal and opposite bending forces on the individual tracks. To test this, a 160 lb. load was applied to each track individually. The tracks were again noticed to deform slightly, partly due to the track mount, but suffer no plastic deformation. This proves that the tracks will be strong enough to support the trolley and mounted device.

Overall, the trolley system tested with tremendous success. All of the calculations made were upheld through the testing process. The testing demonstrated that the mounted device would be safe and secure above traffic. The mounted device will also be able to operate properly because of the robust nature of the trolley. The testing performed on the trolley system proves that it is acceptable to be used as an overhead device mounting system.

CHAPTER 9

CONCLUSION

The main objective of this project was to perform a comprehensive engineering study on a unique system for mounting overhead detectors and other electronic measuring devices over individual lanes of traffic. This study involved the development, design, theoretical analysis, and manufacturing of the platform mounting system. The goal of this study was to show that the proposed mounting system is an acceptable means for mounting overhead measuring devices over live traffic.

The development stage introduced the idea to use a roller coaster based platform (or trolley) to carry the measuring devices over traffic. The design of this trolley mounting system was done such that the overhead devices could be safely, easily, and effectively mounted over traffic. This was accomplished by creating a simple yet sturdy trolley. The simple design allows the trolley to be easily manufactured. The trolley has few moving parts, which grants fewer modes of failure. It is remotely controlled using RF communication to allow ease of use and accurate positioning over the lanes of traffic. A method for mounting the trolley system onto the tracks from the ground creates efficient use of time and resources.

The theoretical analysis was performed to verify and support the mounting system design choices. The analysis was widespread in that it examined nearly every aspect of the trolley design. The strength and durability of every significant trolley component was analyzed and either chosen from the analysis or shown to be acceptable for use on the trolley. The analysis also examined the environmental robustness of the system. The trolley system was evaluated for its ability to withstand the rain, sun, and wind to which it

will be exposed. In addition, the trolley was analyzed for its response to vibration. This analysis looked at the multiple modes of vibration that the trolley would be subject to and determined the magnitude of vibration that the mounted measuring device would experience. Through this exhaustive theoretical analysis, the trolley system was shown to be strong and durable, endure the elements to which it will be exposed, and minimize the vibrations transmitted to the mounted measuring device.

The manufacture of a prototype trolley allowed the design and analysis to be substantiated. The prototype was put through multiple tests to simulate actual operational events and obstacles. The system was tested for strength, environmental stability, and response to vibration. The testing procedure validated the design and analysis performed on the trolley system.

Throughout this project, lessons were learned along the way. During the design stage, the system had to be re-designed many different times. This was due to changing requirements of the system as well as inefficient initial designs. From this, it was learned that when designing a product, one should first have a good understanding of all the requirements and research possible designs before attempting them. Through the analysis, it was learned how to relate the known equations to the application at hand. The manufacturing process allowed me to learn much more about the use and capabilities of the machinery in the student machine shop. And from the prototype testing, it was learned how to find unique and unconventional methods to perform tests on the system that will simulate the desired situation.

Overall, this project turned out to be very successful. Through the multiple stages of study, the trolley system was shown to be an acceptable method of mounting overhead measuring devices over traffic. The analysis performed theorized that the system would be able to confidently withstand the loads to which it will be subject, as well as being environmentally stable, and able to suppress the majority of vibrations that it experiences. The prototype constructed proved to agree with the analysis performed, and through

much testing, the trolley system was found to be very robust. This system can be confidently placed over traffic safely, easily, and effectively.

REFERENCES

[1] Palen, Joe, *Personal Consultation on Multiple Trolley Aspects*, June 2000-July 2001.

[2] Cheng, H. H., Ben Shaw, Joe Palen, Jonathan E. Larson, Xudong Hu, Kirk Van Katwyk, *A Real-Time Laser-Based Detection System for Measurement of Delineations of Moving Vehicles*, IEEE/ASME Trans. On Mechatronics, Vol. 6, No. 2, June 2001, pp. 170-187.

[3] Banerjee, A. K., *Dynamics and Control of the Shuttle-Based WISP Antenna*, Journal of the Astronautical Sceinces, January-March, 1993, pp. 73-90.

[4] Singhose, W., A. K. Banerjee, and W. E. Seering, *Slewing Flexible Spacecraft with Deflection Limiting Input Shaping*, Journal of Guidance, Control, and Dynamics, 1997, vol. 20, no. 2, pp. 291-298.

[5] Banerjee, A. K. and W. Singhose, *Command Shaping in Tracking Control of a Two-Link Flexible Robot*, Journal of Guidance, Control, and Dynamics, Nov.-Dec. 1998, pp. 1012-1015.

[6] Banerjee, A. K., N. Pedreiro, and W. Singhose, *Vibration Reduction for Flexible Spacecraft Following Momentum Dumping with/without Slewing*, to appear in the journal of Guidance, Control, and Dynamics.

[7] Singer, N. C. and W. P. Seering, *Preshaping Command Inputs to Reduce System Vibration*, Journal of Dynamic Systems, Measurement, and Control, March 1990, pp. 76-82.

[8] Shigley, Joseph Edward and Charles R. Mischke, *Mechanical Engineering Design*, 5th ed., McGraw-Hill, Inc., New York, NY, 1989.

[9] Kraige, L. G. and J. L. Meriam, *Engineering Mechanics Dynamics*, 4th ed., John Wiley & Sons, Inc., New York, NY, 1997.

[10] Stock Drive Products/Sterling Instruments, *Handbook of Inch Drive Components*, Catalog 787, 1998.

[11] Craig, Roy R. Jr., *Mechanics of Material*, John Wiley & Sons, Inc., New York, NY, 1996.

[12] Gillespie, Thomas D., *Fundamentals of Vehicle Dynamics*, Society of Automotive Engineers, Inc., Warrendale, PA, 1992.

[13] Inman, Daniel J., *Engineering Vibration*, Prentice Hall, Englewood Cliffs, NJ, 1996.

[14] Karnopp, Dean C. and Ronald C. Rosenberg, *Introduction to Physical System Dynamics*, McGraw-Hill, Inc., New York, NY, 1983.

[15] Enidine Inc., An IMC Company, *Elastomeric Isolation Mounts Product Catalog and Selection Guide*: http://www.enidine.com/pdffiles/Elastomer.pdf. October 2001.

[16] Deeley, Paul D., Konrad J.A. Kundig, and Howard R. Spendelow Jr., *Ferroalloys and Alloying Additives Handbook*, Sheildalloy Corporation, Newfield, NJ and Metallurg Alloy Corporation, New York, NY, 1981.

[17] White, Frank M., *Fluid Mechanics*, 3rd ed., McGraw Hill, Inc., New York, NY, 1994.

[18] Kraige, L. G. and J. L. Meriam, *Engineering Mechanics vol. 1, Statics*, 3rd ed., John Wiley & Sons, Inc., New York, NY, 1992.

[19] Bin Lin, H. H. Cheng, Ben Shaw, Joe Palen, *Optical and Electronic Design for a Field Prototype of a Laser-Based Vehicle Delineation Detection System*, Optics and Lasers in Engineering, Vol. 36, No., July 2001, pp. 11-27.

[20] Cheng H. H., B. D. Shaw, Joe Palen, Jonathan E. Larson, Xudong Hu, Kirk Van Katwyk K., *Non-Intrusive Laser-Based System for Detecting Objects Moving Across a Planar Surface*. Patent recently approved by the U. S. Patent Office.